UNIVERSITY OF CATANIA

Department of Chemical Sciences
International PhD in Chemical Sciences
Cycle XXXIV
_____

Luca Spitaleri

Self-Assembly of Plasmonic and/or Luminescent Nanostructures

PhD Thesis

Tutor:
Prof. Antonino Gulino
Coordinator:
Prof. Salvatore Sortino
_____

ACADEMIC YEARS 2018-2021

A mio Padre Giuseppe

"Sei stato un gran maestro di vita senza mai farmi

mancare l'amore che ogni figlio dovrebbe ricevere.

Grazie per aver sempre creduto in me,

ti vorrò sempre tanto bene!"

Contents

Abstract

The aim of this PhD thesis is the fabrication, through bottom-up approaches, of hybrid plasmonic and/or luminescent molecular-nanoparticle nanostructures that are well suitable for the synthesis of functional nanostructures showing structural control (in terms of ability to direct the formation of large assemblies in solution and in the solid-state), peculiar and appealing properties, e.g. optical, electronic or catalytic properties, in the perspective of their applications in different fields of nanotechnology. In addition, the combination of different optical properties belonging to the different molecular components represents an advanced method to manufacture hybrid assemblies, useful for improved optical applications.

Gold nanoparticles (Au NPs) exhibit important chemical, electronic and optical properties, due to their size, shape, and electronic structures. Au NPs containing no more than 30-40 atoms are only luminescent because they can be regarded as large molecules with discrete energy levels. While nano-sized Au NPs only show the surface plasmon resonance because the energy level spacing becomes smaller as the number of gold atoms increases. Therefore, the formation of a band may result in the loss of luminescence. Hence, it appears that gold nanoparticles can alternatively be luminescent or plasmonic and this represents a severe constraint for their use as an optical material.

To overcome such a limitation, and achieve the above-mentioned purpose, the present study aims at the self-assembly of plasmonic Au NPs with multi-functional emissive building blocks.

For these reasons, we have chosen porphyrin molecules and europium complexes as emissive building blocks.

In this context, it was synthesized a novel bi-functional porphyrin molecule having two triazine moieties, in two opposite positions of the porphyrin ring, that works as bridges between different gold nanoparticles. Indeed, the molecular structure of these new bi-functional porphyrin molecules allows the formation of an extensive and covalently linked Au NP network, characterized by plasmonic and emissive properties. Effectively, this functional architecture shows a strong surface plasmon, due to the Au nanoparticles, and a strong luminescence signal coming from porphyrin molecules, thus, behaving like an artificial organized plasmonic and fluorescent network.

In addition, we experimentally investigated the luminescence quenching for europium complexes bound to Au nanostructures. We have studied this effect for two very similar europium complexes, one of which can covalently assemble on gold nanoparticle surfaces while the other cannot do it. We found that the Au nanostructures covalently surrounded by the Eu complex remained plasmonic and luminescent, while a total emission quenching was observed for the Eu complex not suited to covalent interact with the Au nanostructures. This behaviour was rationalized in terms of through bond vs. through-space interactions between the Eu complex and the Au nanoparticles.

Finally, plasmonic Au_ZnO core-shell nanoparticles were prepared by "one-pot" synthesis in which a [Zinc Citrate]$^-$ complex acts as ZnO precursor,

reducing agent for Au^{3+} and capping anion for the obtained Au nanoparticles. Gold nanostructures absorb visible light and show localized surface plasmon resonance bands in the visible region. Semiconducting ZnO nanostructures are excellent for ultraviolet detection thanks to their wide bandgap, large free exciton binding energy and high electron mobility. Therefore, the coupling of gold and ZnO nanostructures represents the best-suited way to enhance photodetection.

The photocatalytic activity of such core-shell nanostructures was investigated through the photodegradation of a standard methylene blue (MB) solution, according to ISO 10678:2010. Sun light was used as an irradiation source, and it was observed a fast and efficient MB decomposition.

To sum up, the most important achievement of this thesis is to have demonstrated that the covalent assembly of suitable molecules on gold nanoparticles surfaces allows the synthesis of architectures showing peculiar and unique properties appealing for future technologies. Noteworthy, some of these hybrid nanomaterials both show a strong surface plasmon and a strong luminescence signal.
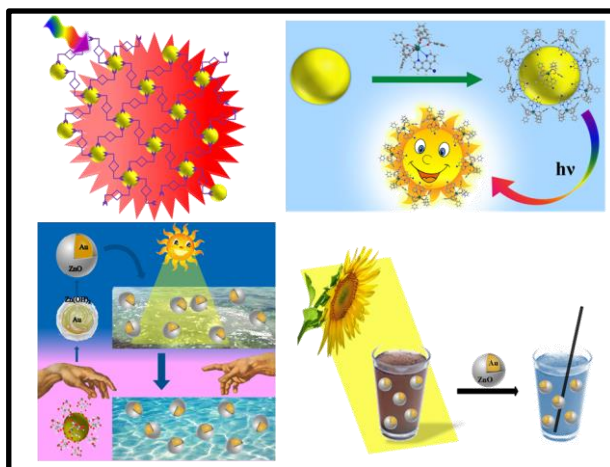
Chapter 1

Introduction

1.1 Nanotechnology and Nanomaterials

The birth of the concepts of nanotechnology was first discussed in 1959 by Nobel Prize winner Richard Feynman in his talk "There's Plenty of Room at the Bottom", in which he described the possibility of synthesis via direct manipulation of atoms and how its advancement could potentially generate an enormous number of technical applications.

Nanotechnology sciences focus on the research and technology development of systems at atomic, molecular and macromolecular scales, which leads to the controlled assembly and study of structures and devices with length scales typically in the range between 1 and 100 nm.[1] These novel types of materials have been called nanomaterials. The allure of nanotechnology comes from the possibility to control the properties of the material assembling such building blocks at the nanoscale.

In this context, a vast array of novel nanostructures has been manufactured and studied in the interdisciplinary fields of nanoscience, such as chemistry, physics, electronics, medicine, engineering, agriculture, biology, material science, etc....[2] The particular optical, electronic, magnetic, mechanical, or chemical properties of such nanostructures are due to their size, composition and shape which differ drastically from those of bulk materials.[3]

In fact, in the last decades, nanotechnology's research has grown exponentially, thanks to the possibility of observing unique phenomena, which cannot be investigated in similar chemical systems characterized by larger dimensions.[1] Indeed, nanostructured materials with tunable morphology (e.g. nanoparticles, nanowires, nanofibers, nanotubes, etc.) show novel properties and functions of exceptional interest, in virtue of their unique architectures, tailored physico-chemical features, which make them materials of a central role in fabricating nanoelectronics and biosensing devices.

Therefore, the synthesis of multifunctional systems, to confer functional and specific properties, which allows their use in different applications, such as electronics, optoelectronics, biosensing, drug delivery, imaging, catalysis, is nowadays important.[4-7]

Nanostructures can be synthesized by two main approaches: the top-down and bottom-up methods. The top-down approach involves the construction of nanostructures starting from the miniaturization of macroscopic materials. Lithography is the main used technology, which provides the transfer of a pattern on the matrix of interest. This methodology is used for the fabrication of integrated circuits.[8]

Otherwise, the bottom-up approach deals with the synthesis of nanomaterials, using atoms and/or molecules as "molecular building blocks" which are assembled by weak interactions (self-assembly).[9-12] The self-assembly is a chemical process in which molecular systems self-assemble, that is form ordered structures. The bottom-up synthesis is the most promising approach for the design of hybrid inorganic/organic nanostructures constituted from organic molecules or inorganic metal complexes covalently bound to inorganic metal

nanoparticles with novel and peculiar properties.[13, 14] Such materials own the advantage to be inexpensive, miniaturized, robust and easy to fabricate. Currently, the surface functionalization with functional molecules, obtained with the bottom-up approach, produces multi-functional systems in which it can be observed an excellent structural control at the nanometric level.[15, 16]

1.2 Plasmonic and/or Luminescent Nanostructures

In the last decades, multifunctional nanomaterials showing simultaneously two or more functionalities, i.e., luminescence, magnetism, plasmonic and catalytic activity, have been extensively investigated because they are the combination of different properties in a single nanomaterial.[17-19]

Noble metals are exceptionally resistant metals to corrosion and oxidation even at high temperatures and these include Rh, Ru, Pd, Ag, Os, Ir, Pt and Au. This class of elements has found a wide range of applications ranging from the aerospace to electronics industries and healthcare.[20]

Therefore, noble metals nanoparticles (NM NPs) recently have become one of the central points of nanomaterial fabrication, due to their peculiar and tuneable chemical-physical properties, which cannot be observed in bulk materials.

Important features shown by this class of nanomaterials are (i) the presence of surface plasmon resonance (SPR) which gives rise to the intense absorptions or scattering bands (Surface-Enhanced Raman Scattering, SERS) in the visible or near-infrared regions (NIR);[20] (ii) surface plasmon-induced enhancement or quenching fluorescence of emissive molecules;[21] (iii) the easy surface

functionalization with a wide series of molecules;[22] (iv) the great chemical and physical stability that determine resistance to high temperature, photoirradiation, acids or oxidation;[22, 23] (v) important properties related to the high surface area and the particular electronic structure.[22, 24]

The dominant property of noble metal nanoparticles arises due to their ability to form surface plasmons. However, depending on their size, these nanoparticles can alternatively be luminescent or plasmonic and this represents a limit to their use as an optical material.

In this context, the combination of plasmonic nanoparticles with emissive molecules allows the manufacture of luminescent-plasmonic nanostructures that can exhibit novel spectroscopic properties, due to the interactions between both systems. These effects mainly depend on the spectral position of the SPR bands and on their overlappping with the absorption/emission bands of the luminescent dye, as well as on the distance between the plasmonic and luminescent systems.[25] Such mutual interactions can lead to enhancement or quenching of fluorescence intensity of the dye, alterations of luminescence lifetimes, etc.

1.3 Gold Nanoparticles: Synthesis and Properties

An important class of NM NPs is represented by gold nanoparticles (Au NPs), which are attracting the attention of a large community of scientists because of their tuneable and distinctive chemical, optical, magnetic and electronic properties, due to their modifiable electronic structures.[26, 27] In fact, Au NPs with large surface area-to-volume ratio show size- and shape-dependent physico-chemical properties, which represent invaluable features for

applications in different technological fields such as photonics, heterogeneous catalysis, electronics, biosensors, drug delivery, therapeutics, imaging, etc (Figure 1.1).[28-30]
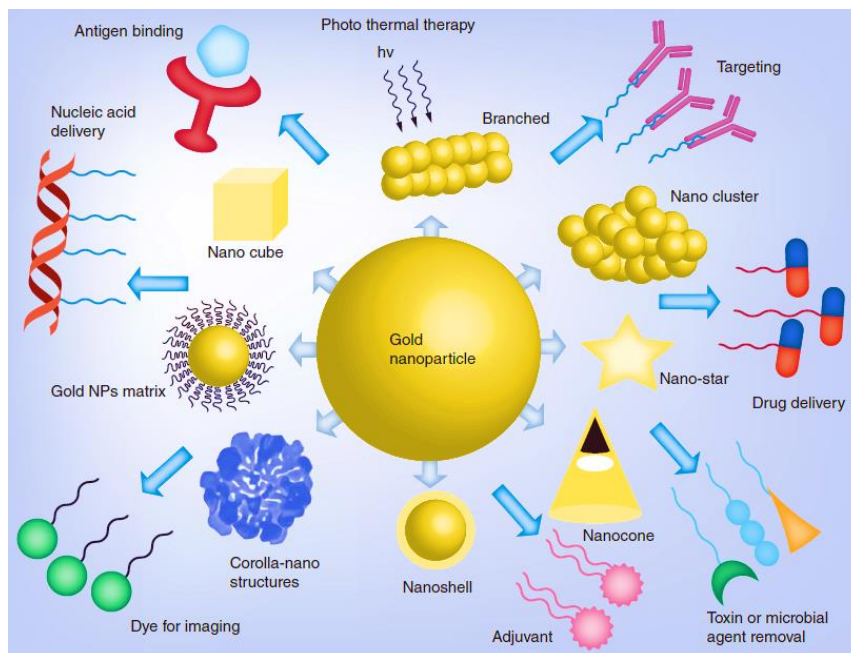

Figure 1.1. Functionalization of different shapes of Au NPs.

The first scientist who related the optical properties of gold nanoparticles to their small size was Michael Faraday in 1857 when he successfully prepared a ruby-red gold colloid through the reduction method. This work laid down the foundation for later colloid science.[31] Nevertheless, a better understanding of this experimental observation occurs in 1908, when Gustav Mie provided an analytical solution to Maxwell's equations for a spherical particle using the complex dielectric constants ($\varepsilon_1 + i\varepsilon_2$) of metals and successfully modelled the optical extinction spectra of gold colloids.[32]

Gold nanoparticles are essentially inert, non-toxic, biocompatible, and exhibit several interesting properties such as surface plasmon resonance,

surface-enhanced Raman scattering, redox activity, fluorescence quenching and nonlinear optical properties.[33-35]

Doubtless, the most fascinating property of the Au NPs derives from dimensional confinement (sizes smaller than the wavelength of light), which leads to the alteration of their optical response following the appearance of a phenomenon called "surface plasmon resonance" (SPR), which fundamentally arises from the collective and coherent oscillation of the free conduction electrons in a continuous band structure, due to the resonant excitation caused by the incident photons or electromagnetic radiation.[27, 34, 36] Figure 1.2 shows a schematic illustration of this phenomenon for an Au nanoparticle.
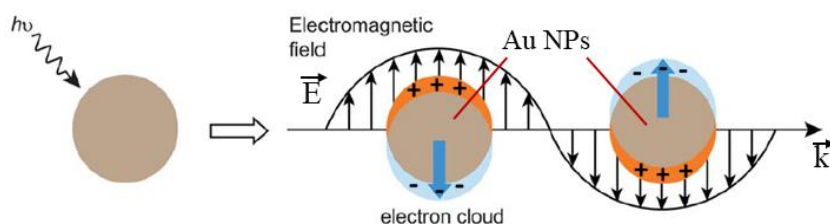

Figure 1.2. Schematic representation of the oscillation of conduction electrons across the nanoparticle in the electromagnetic field of the incident light.

In general, this process is due to two different types of light-matter interactions: scattering, in which the incident light is re-radiated in all directions at the same frequency, and absorption, in which the light is converted to heat (e.g., phonons or vibrations of the crystal lattice).[30] In addition, the collective charge oscillation causes a large resonant enhancement of the local electric field inside and near the NP, which can be used to greatly enhance the optical signals (e.g., fluorescence or Raman scattering) arising from molecular species in the vicinity of the surface.[35, 37, 38] Nowadays, the field of nanoplasmonics is rapidly and successfully developing in numerous applications, such as Surface-

Enhanced Raman Spectroscopy (SERS),[35] plasmon-enhanced fluorescence,[39, 40] amplification of non-linear optical signals,[41] light-harvesting,[42] photocatalysis,[43] and chemical and biological sensing (Figure 1.3).[44, 45]
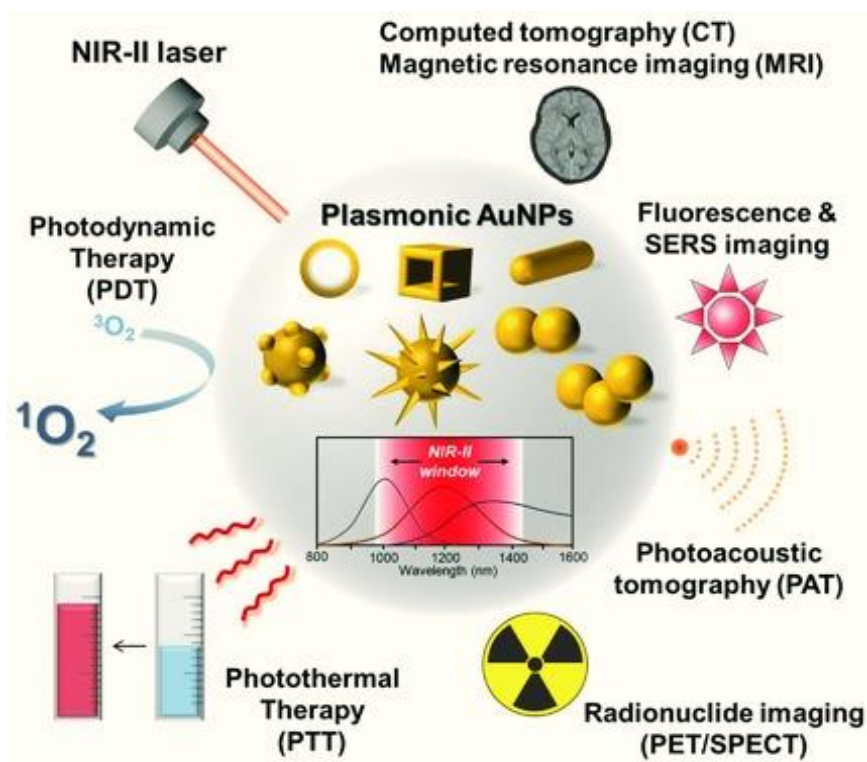
Figure 1.3. Some applications of Plasmonic Gold nanoparticles.

Moreover, the position of the surface plasmon peak can be significantly influenced by structural factors, such as particle size, aggregation and shape irregularity, dielectric environment, refractive index, and proximity of other nanoparticles.[46-49] Indeed, the increase in the core size of the nanoparticles from 1 to 100 nm and their aggregation, results in significant red-shifting of SPR frequency, broadening of surface plasmon band (Figure 1.4A) and a variation in the solution colour from ruby red to blue due to the interparticle plasmon coupling (Figure 1.4B).[34]

Figure 1.4. A) Optical extinction spectra of gold colloids solutions between 3-100 nm diameters. B) The different size of the suspensions of gold nanoparticles causes the changing in colours of the solutions.

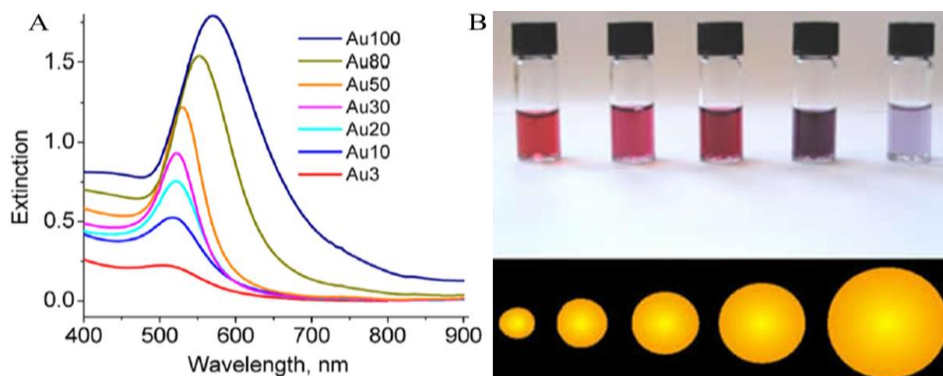However, this plasmonic band is absent in both the bulk material, in which the energy levels of the electrons are continuous, and small nanoparticles (diameter < ~3 nm), in which there are discrete energy levels.

The characterization of the photoluminescence properties of gold nanostructures was less thorough than the study of plasmonic properties. It has been reported that as the particle size becomes comparable to the electron Fermi wavelength of gold metal, Au NPs behave like "large molecules" with discrete energy levels.[41, 50] Therefore, the band structure evolves into discrete energy levels, allowing for interactions with light through the electronic transitions between the different energy levels, resulting in strong photoluminescence properties (Scheme 1.1).[30] On this extremely small size scale, Au NPs are often called "Au nanoclusters" (Au NCs).[27, 51, 52]
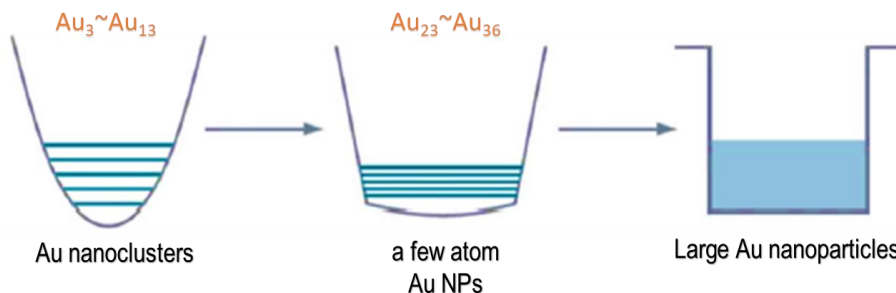
Scheme 1.1. Schematic of the size-dependent surface potentials of Au clusters on different size scales.

The observed quantized transitions (luminescence) from Au NCs follow the free-electron model (based on the assumption that the valence electrons can travel freely through the cluster due to the negligible interactions between the valence electrons and the cores) and arise from both intraband (sp–sp) and interband (sp–d) electronic transitions (Scheme 1.2).[53]
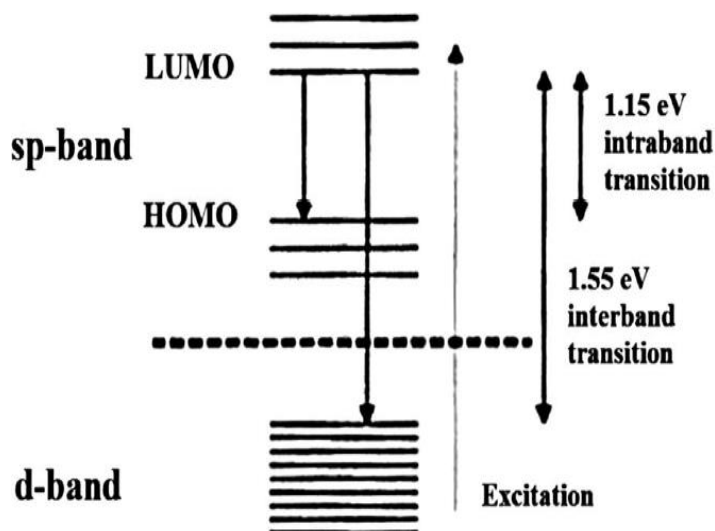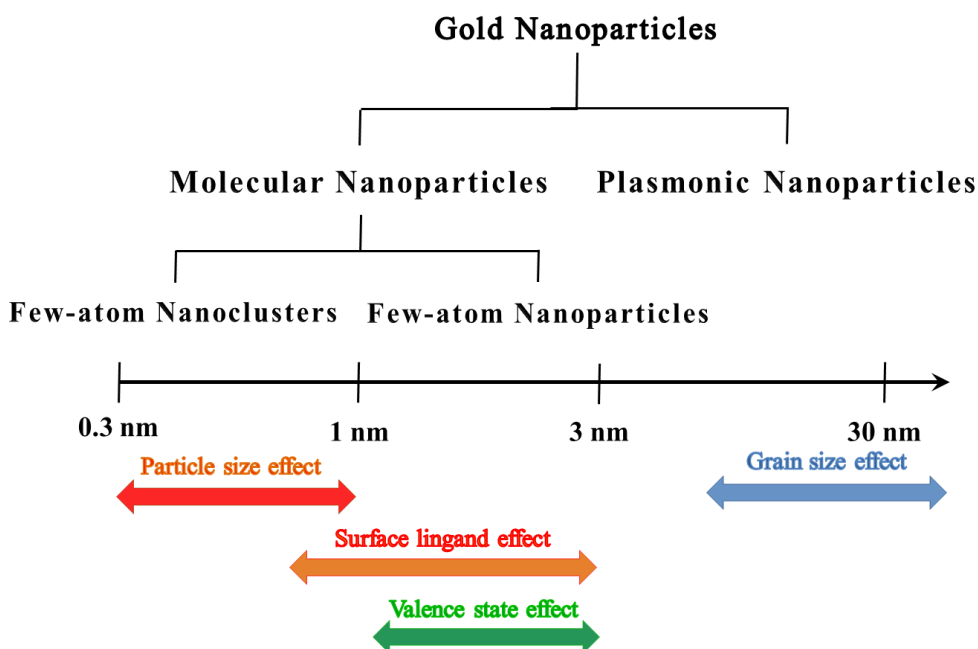

Scheme 1.2. Representation of the energy levels of the Au NCs involved in the luminescence mechanism.

Indeed, the high energy band is due to radiative interband recombination between the sp and d bands, while the low energy band results from radiative

intraband transitions within the sp band across the HOMO–LUMO gap. Furthermore, the intraband recombination must involve prior non-radiative recombination of the hole in the d-band created after excitation with an (unexcited) electron in the sp band.[41, 53]

Depending on their size, Au NPs can be classified into two major classes: Au molecular luminescent or plasmonic NPs (Scheme 1.3).[53] Molecular Au NPs (d < ~3 nm), do not exhibit any surface plasmon resonance absorption in the visible region, due to the limited number of free electrons on its surface, but they show fluorescence from the visible to near-infrared region. Also, other factors can significantly influence the luminescence properties of Au molecular luminescent NPs, such as the number of Au atoms in each cluster, the type of surface ligands, the aggregation valence states of metal atoms, and grain size.[30, 53]

Gold Nanoparticles

Molecular Nanoparticles   **Plasmonic Nanoparticles**

Few-atom Nanoclusters   **Few-atom Nanoparticles**

0.3 nm   1 nm   3 nm   30 nm

Particle size effect   Grain size effect

Surface lingand effect

Valence state effect

Scheme 1.3. Classification of Au NPs as a function of size.

Consequently, with advantages of long lifetime, large Stokes shift, and biocompatibility, Au molecular luminescent NPs have become interesting sensing and imaging materials.[34, 41, 50, 51]

Taking this into account, Au can be considered an excellent example of a multifunctional nanomaterial whose electronic and optical properties can be readily engineered by tuning the size, shape, and/or structure, all without altering the basic elemental composition.

Gold nanoparticles have been synthesized ever since ~1950. In the past few decades, they have typically been synthesized by reduction of tetrachloroauric acid ($HAuCl_4$), in presence of reducing and stabilizing molecules that control the size, shape, structure and surface functionality.[54-56] Specific molecules have been used to hamper the particle growth and confine their size within a few nanometers range. In fact, surface capping with appropriate molecular coupling layers is, so far, the most important method to achieve the purpose.[36,57-59] Therefore, phosphines, thiols, amines, citrate anion, dendrimers, DNA, proteins, tannic acid, etc. represent the most suitable and used capping molecules.[60-67]

Although many protocols have been reported in the literature, most of them can be considered variants of two methods originally developed by Turkevich and Brust-Schriffin, respectively.

Turkevich et al.[68] were the pioneers for the development of the synthetic method for Au NPs in 1951, which was further refined by Frens in the 1970.[69] In both synthetic methods, the $HAuCl_4$ solutions are treated with citric acid in boiling water, where the citrate anion acts as both a reducing agent of the $AuCl_4^-$ ions to Au(0) atoms, and a capping agent by binding to the Au surface to prevent the nuclei from aggregating together (Scheme 1.4). This process has been widely

employed to prepare dilute solutions of stable spherical monodisperse Au NPs with diameters of around 10-20 nm. In this thesis, the Au NPs solutions were prepared following these previous methods.
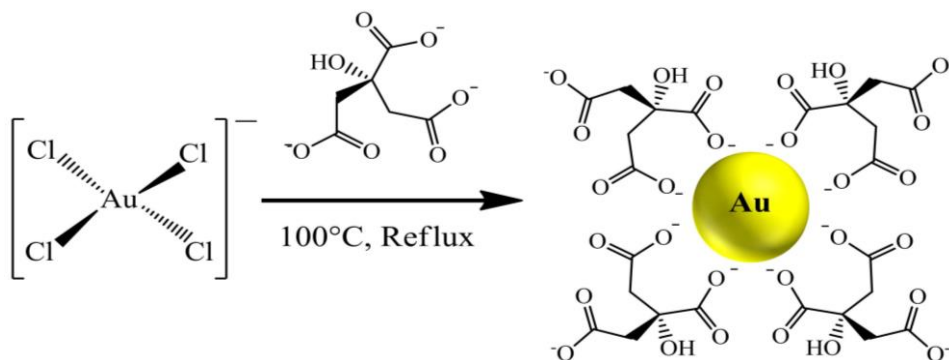
Scheme 1.4. Schematic representation of the citrate-stabilized Au NPs synthesis.

In early 1994, Brust and Schriffin[70] described a new facile method for synthesizing highly stable Au NPs in organic liquids. This synthesis is based on a two-phase process in which a water-soluble gold salt ($AuCl_4^-$) is transferred in toluene using tetraoctylammonium bromide (TOAB) as a phase-transfer agent. The Au^{3+} ions are reduced to Au^0 by sodium borohydride ($NaBH_4$) in the presence of alkanethiol acting as a stabilizing agent (Scheme 1.5).
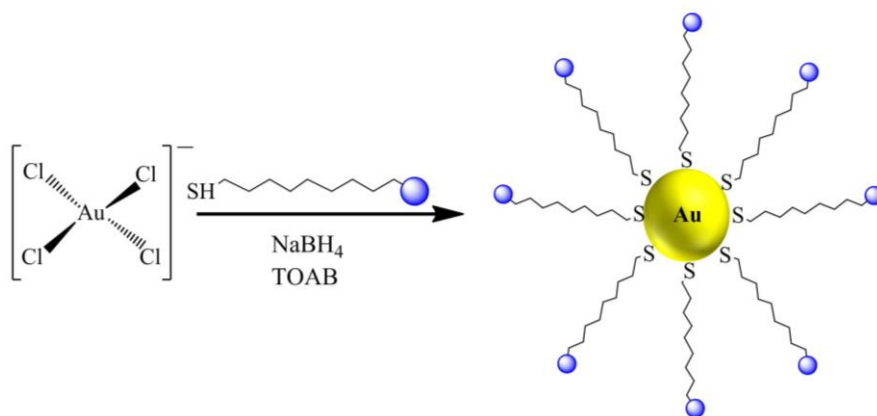
Scheme 1.5. Schematic representation of the two-phase synthesis of Au NPs by reduction of $HAuCl_4$ in the presence of TOAB, alkanethiols and $NaBH_4$.

Therefore, the robustness of the synthetic methods and the fine control of the chemical-physical properties of Au NPs are the main reasons for their potential use in various scientific fields, ranging from chemistry to nanomedicine.

1.4 Hybrid Organic–Inorganic Nanostructures: Synthesis and Properties

As discussed above, it appears that gold nanoparticles can alternatively be luminescent or plasmonic and this represents a severe constraint for their use as an optical material.

In this context, one of the most interesting research fields of the recent decades is the assembly of hybrid materials (those formed from the combination of two or more different materials) which opens the way for the development of a great variety of new nanomaterials with peculiar and multiple functionalities that have potential applications in different areas such as imaging,[22] nanomedicine,[71] energy storage,[72] catalysis[73] and solar energy.[74]

Indeed, the resulting hybrid nanomaterial is not a simple mixture of its components, but a synergistic system in which, in addition to a simple combination of properties, novel distinctive and enhanced properties may be expected due to the interactions at the interface between the components at the molecular or supramolecular level.

Hybrid materials investigated thus far include mixed metal oxides, inorganic particles (e.g., clusters, noble metal nanoparticles) coated with organic compounds (e.g., dyes, biological probes) or inorganic compounds (e.g.,

transition metal or lanthanide complexes), organic or inorganic compounds embedded in sol-gel matrices or in metal-organic frameworks (MOFs) and layered organic-inorganic materials.[75, 76]

Among them, hybrid molecular–nanoparticle materials, obtained by a bottom-up approach, are well-suited for the fabrication of functional nanostructures that exhibit structural control[77-79] (in terms of ability to direct the formation of large assemblies in solution and in solid state) and show well-defined properties, e.g., to obtain building blocks for molecular switches,[15, 16] systems for photocatalysis and photodynamic therapy,[80] nanowires for multienzyme-cooperative antioxidative systems,[81] specific complementarities and strong recognition properties of biomaterials[82], materials able to enhance light absorption,[83] and, in general, hybrid organic–inorganic materials showing desired functions.[84-86]

Gold nanoparticles are generally surface-stabilized by a shell of adsorbed organic molecules (capping ligands) which define the colloidal stability, solubility, size, surface charge and other potential applications.[22] Nevertheless, the labile capping ligands on Au NPs (citrates, phosphines, thiols, amines, or other adsorbed ligands) can be displaced (partially or totally) by other functional molecules through a ligand place-exchange reaction to synthesize hybrid molecular-Au NPs for synergistic applications.[87]

Figure 1.5 summarizes hybrid Au NPs can be synthesized based on their length scale and material complexity.
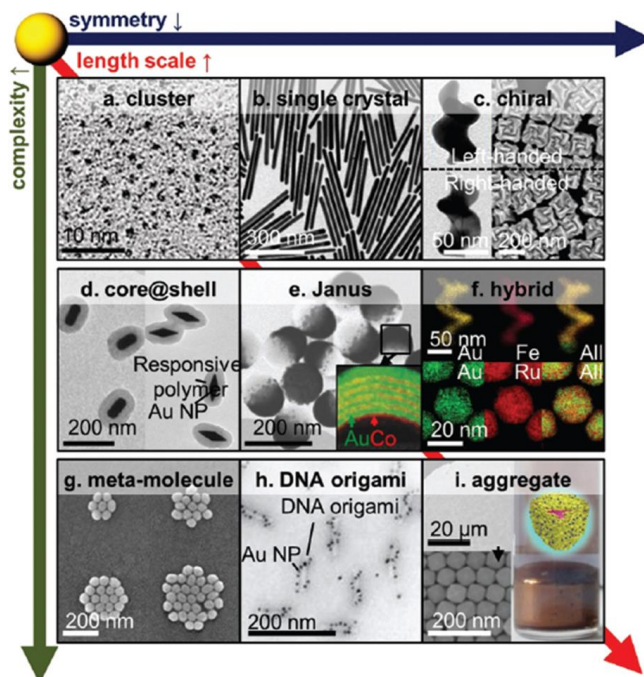
Figure 1.5. Representative hybrid Au nanoparticles are organized according to the structural dimensions.

The success of the ligand place-exchange reaction depends on the chemical nature (bond strength) of the capping ligand and the substituent functional molecule. In fact, the substituent functional molecules must have equal or higher binding affinity than the capping ligand for gold in order to obtain an efficient replacement.[75, 88] Therefore, the difference in binding strength of substituent functional molecule-Au and capping ligand-Au, and the size of the ligands determine the reaction rate and the degree of surface functionalization (quantitative or partial) of the Au NP hybrid shell.

Au NPs can be conjugated with a rich variety of biofunctional molecules (porphyrin, oligonucleotide, polymer, protein, inorganic complexes, etc.) through different interactions such as specific binding affinity, electrostatic

interactions, and hydrophobic interactions.[89] These non-covalent interactions are widely utilized in delivery and sensing areas due to their ease of release and reversible nature. Alternatively, covalent conjugation of molecules to Au NPs stabilizes the conjugates, which is more useful as stable constructs are required, e.g. for imaging.

In the last few years, many different synthetic methods have been proposed to get these hybrid Au NPs with multi-functionality, depending on the molecular functional group used as a linker for the Au NPs.[58, 59, 62, 90, 91] However, only a few of the synthesized systems were characterized by both these properties, surface plasmonic resonance and luminescence.

Taking all the above-mentioned considerations into account, in the present thesis we used the bottom-up approach to anchor inorganic and organic emissive molecules on Au nanoparticles surfaces to fabricate new hybrid molecular–nanoparticle materials characterized by a strong surface plasmon resonance and an intense luminescence signal. For these reasons, we have chosen porphyrins, Eu(III) complexes and zinc citrate as building blocks to bind to plasmonic Au NPs in order to obtain novel nanosystems and investigate their optical properties.

Chapter 2

Covalently Conjugated Gold–Porphyrin Nanostructures

Porphyrin and metalloporphyrin molecules have attracted great attention because of their interesting chemical, biological, optical, magnetic and electronic properties.[92] For such reason they can be smartly modified by adding/changing the macrocycle peripheral substituents and/or by modulating the oxidation state of the metal centre. Moreover, surface-anchored molecular switches,[93] porphyrins for charge-based information storage,[94, 95] and porphyrin nanostructures with a long-range order on Si(100)[96] have been reported. In this context, porphyrin molecules anchored to electroactive surfaces can be used to build molecular memories that can be integrated into electronic circuits. Porphyrin-based information storage elements exhibit large charge retention times (minutes) compared to those of the semiconductor elements in dynamic random-access memory (tens of milliseconds).[95]

Taking into account all the above considerations, hybrid materials composed of both Au NPs and porphyrin molecules that cover their surfaces combine many of their distinctive characteristics, thus, originating unique properties fundamental for the development of new optical devices that can be used for many different applications, e.g., to mimic natural photosynthesis.[97-103]

Some different synthetic methods have been proposed to obtain these assemblies, depending on the porphyrin functional group used as a linker for the Au NPs.[58, 59, 62, 90, 91, 104]

For this purpose, we have synthesized a new porphyrin with two triazine moieties in two opposite positions of the porphyrin ring, useful to connect these Au NPs to each other. This porphyrin molecule is well suited to act as a bridge for Au NPs in order to obtain an extensive and organized network of Au NPs, covalently linked by organic and emissive connections. To our knowledge, this represents one of the first few cases of an Au NPs–porphyrin organized, plasmonic, and emissive network.[105-110] Hence, we investigated the formation of a new composite assembly consisting of Au NPs covalently anchored to each other by 5,15-Di(phenyl) 10,20-Di-benzamide, N-ethyl, N- 1,3,5 Tri-aminotriazine, 21H,23H-porphine- (DTAzDPH2P) molecules (Figure 2.1).
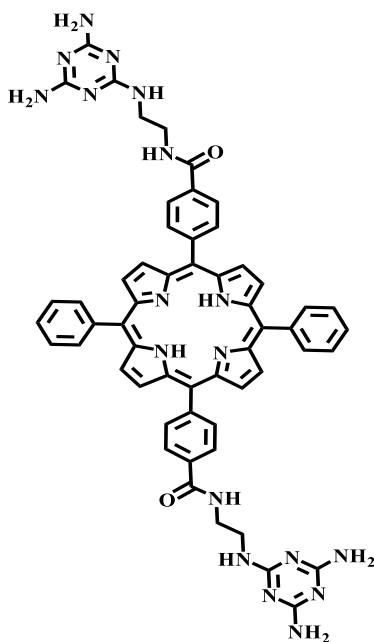

Figure 2.1. Structure of the 5,15-Di(phenyl) 10,20- Di-benzamide, N-ethyl, N-1,3,5 Tri-aminotriazine, 21H,23H-porphine (DTAzDPH2P).

The rationalization of the mutual interactions in this assembled nanocomposite 3D architecture will allow the addressing of applications of this novel plasmonic and emissive material.

2.1 Synthesis of Di-Triazine-Porphyrin

The functionalization of the porphyrin was performed by a synthetic procedure modified as follows[111-113]: 0.14 mmol of 5,15-di-(p-carboxyphenyl)-10,20-diphenyl porphyrin,[114] 0.336 mmol of 1-[Bis(dimethylamino)methylene]-1H-1,2,3-triazolo[4,5-*b*]pyridinium 3-oxid hexafluorophosphate,*N*-[(Dimethylamino)-1H-1,2,3-triazolo-[4,5-*b*]pyridin-1-ylmethylene]-*N*-methylmethanaminium hexafluorophosphate *N*-oxide (HATU, a coupling reagent for the synthesis of amides) were dissolved in 10 mL of dry DMF under N_2 atmosphere (Scheme 2.1). Then, 0.427 mmol of N^2-(2-aminoethyl)-1,3,5-Triazine-2,4,6-triamine[115] and 58 µL of N,N-Diisopropylethylamine (DIPEA, an organic base) were added to the mixture. The reaction mixture was stirred at room temperature for 24 h under nitrogen and then, poured in cooled n-hexane, thus, obtaining a brown precipitate which was filtered and washed with n-hexane. The Di-Triazine-Porphyrin was purified by flash chromatography (Al_2O_3, $CHCl_3$:CH_3OH 95:5) and further crystallized by ethanol (yield 51%).
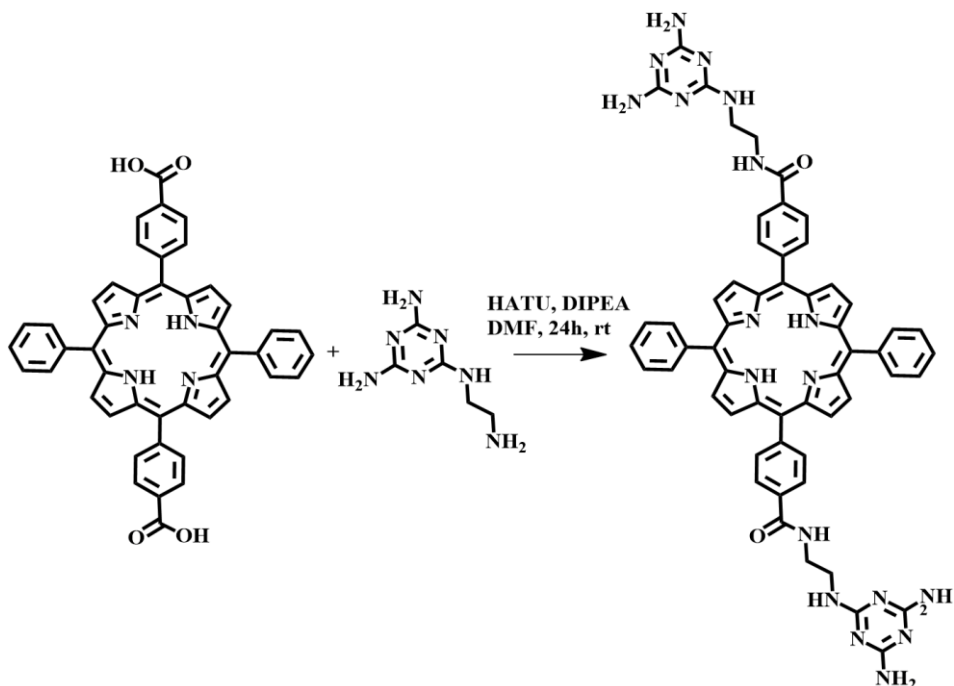
Scheme 2.1. Reaction pathway for the Di-Triazine-Porphyrin.

The characterization of Di-Triazine-Porphyrin was performed by Proton Nuclear Magnetic Resonance (^{1}H-NMR) and Electrospray Ionization Mass Spectrometry (ESI-MS) measurements. ^{1}H NMR (Figure 2.2, 500 MHz, DMSO-d_6) δ -2.91 (s, 2H, NH-Pyr), 3.31 (m, 4H, CH$_2$), 3.61 (m, 4H, CH$_2$), 7.42 (br. s. 8H, NH$_2$-triazine), 7.85 (m, 6H, meso-ArH), 7.89 (br. 2H, NH-triazine), 8.22 (d, J = 6 Hz, 4H, meso-ArH), 8.31 (m, 8H, meso-ArH-triazine), 8.84 (m, 8H, β-Pyr), and 8.94 (s. br. 2H, NH amide) ppm. ESI-MS (Figure 2.3): m/z 1005.8 [M + H]$^+$; m/z 503.5 [M + 2H]$^{2+}$. Anal. Calcd. for C$_{56}$H$_{48}$N$_{18}$O$_2$: C, 66.92; H, 4.81; N, 25.08. Found: C, 66.88; H, 4.77; N, 25.01.
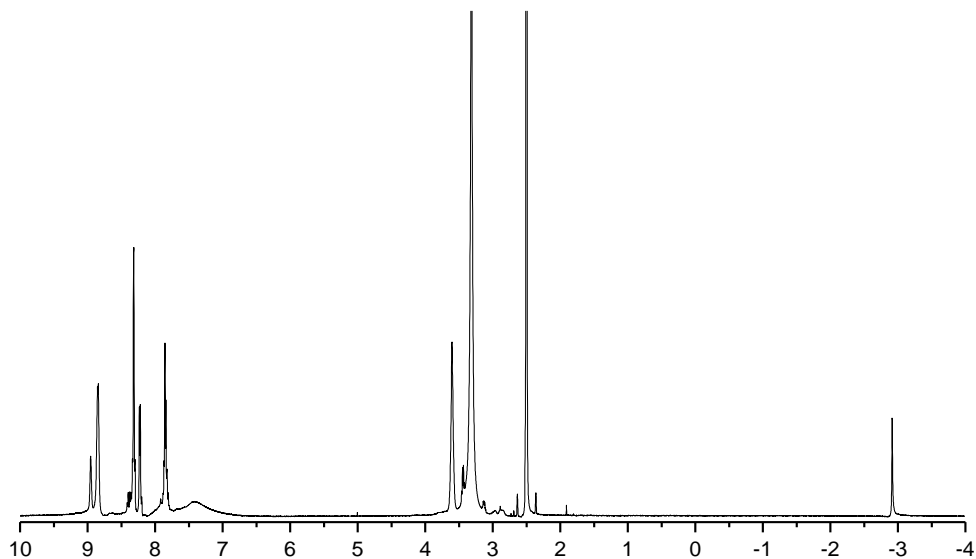
Figure 2.2. ^{1}H NMR spectrum of the 5,15-Di(phenyl) 10, 20 -Di-benzamide, N-ethyl, N- 1,3,5 Tri-aminotriazine, 21H,23H-porphine, recorded in DMSO-d_6.
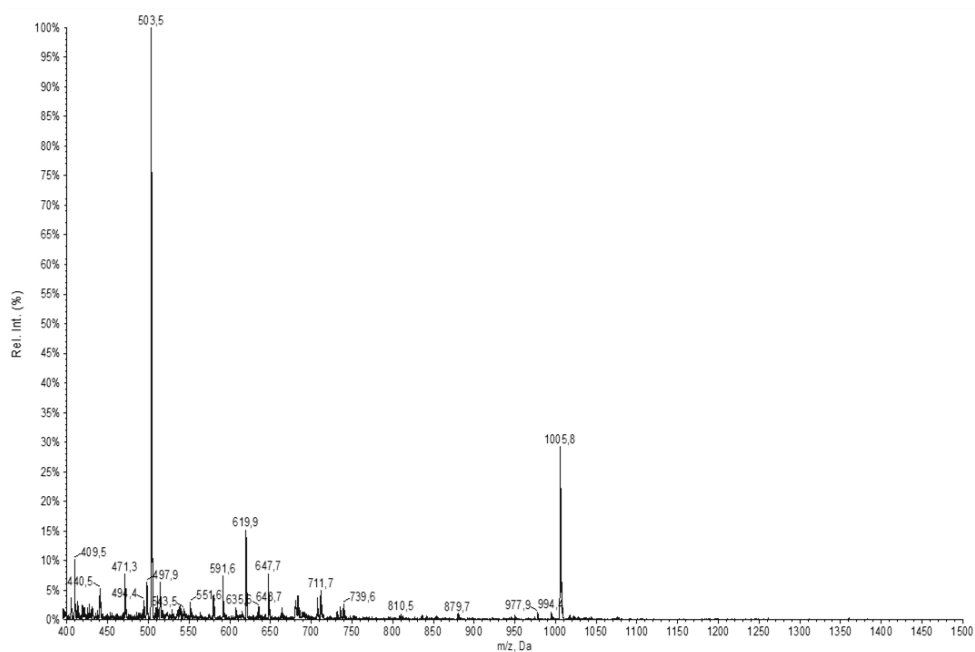

Figure 2.3. ESI-MS spectrum of the 5,15-Di(phenyl) 10, 20 -Di-benzamide, N-ethyl, N- 1,3,5 Tri-aminotriazine, 21H,23H-porphine.

2.2 Synthesis of Gold–Porphyrin Nanostructures

First of all, the Au NPs solutions were prepared as reported in the literature.[68,][69] All the glassware used in the present synthesis was carefully washed with aqua regia (conc. HNO_3 and HCl: 1:3 v/v ratio). A total of 0.036 g of sealed tetrachloroauric acid ($HAuCl_4 \cdot 3H_2O$, MM = 393.835 g/mol, purity $\geq$ 99.9 %) were dissolved in 180 mL of double distilled H_2O (concentration of this stock solution 5.08×10^{-4} M, mole of $Au^{3+} = 9.14 \times 10^{-5}$). Then, we added 18 mL of this Au^{3+} stock solution in a three-necked flask, equipped with a reflux condenser, and brought it on a heating plate to boil, while stirring. Meanwhile, 0.014 g of sodium citrate dihydrate ($Na_3C_6H_5O_7 \cdot 2H_2O$, MM = 294.10 g/mol) were dissolved in 2 mL of fresh, double distilled H_2O (2.38×10^{-2} M, mole of $Cit^{3-} = 4.76 \times 10^{-5}$) and added to the boiling tetrachloroauric acid solution while stirring, thus obtaining a Cit^{3-}/Au^{3+} ratio = 5.21.[116] This solution was refluxed 20 min and its colour turned to ruby red, thus suggesting the formation of Au NPs in water. The obtained solution was centrifuged, the supernatant liquid removed, the Au NPs re-dissolved in double distilled water five times, the last of which using 20 mL of water.

To synthesize the Au NPs–porphyrin nanostructures, we added aliquots of a 2.07×10^{-5} M porphyrin CH_3OH solution (final added volume 900 µL, in 400 min, corresponding to 1.86×10^{-8} mol) to 100 µL of an Au NPs aqueous 1.97×10^{-7} M solution, diluted with 2 mL of CH_3OH (final total volume 3 mL).[36] The synthetic reaction pathway is represented in Scheme 2.2.
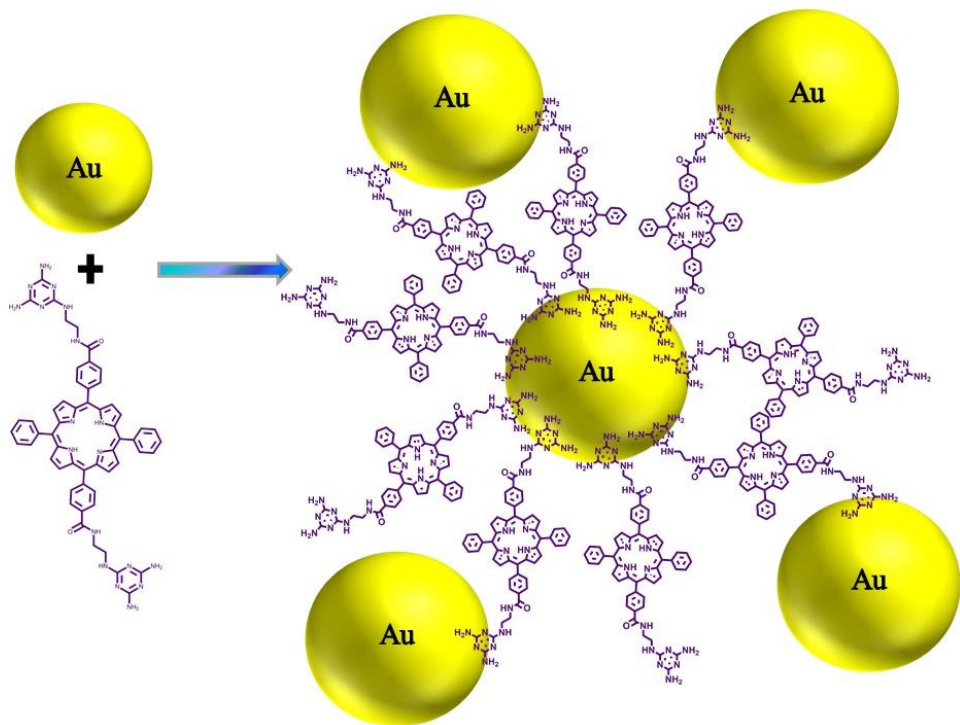
Scheme 2.2. Reaction pathway for the Au NPs–porphyrin nanostructures.

In this proposed scheme, the triazine moieties, which are at 180° with respect to the porphyrin core, covalently bind different Au nanoparticles. The possibility of back-folding of the porphyrin substituents, with both legs attached to the same Au NPs, was investigated by accurate quantum mechanical calculations (vide infra) and resulted in being unlikely. Moreover, quantum mechanical calculations used to optimize the grafting geometry of similar polyfunctional porphyrin molecules on surfaces always indicated geometries tilted with respect to the normal to the surface plane but reminiscent of perpendicular arrangements.[96]

2.3 Quantum Mechanical Calculations

The self-assembly geometry of this porphyrin on the Au NPs (Scheme 2.2) was studied by investigation of the conformational properties of the porphyrin derivative at the Density Functional Theory (DFT) level. All DFT calculations have been performed with the G09 package.[117] Geometry optimizations have been carried out at the B3LYP/6-31G(d, p) level of theory.

To verify the potential conformations of the triazine-based substituents, Potential Energy Surface (PES) scans of the rotational barriers involved along the α–ε bonds of the chain by considering 10 scans of 36° each were performed.[117] To avoid long computational times, we have considered the model reported in Figure 2.4, where also, the labelling of the investigated bonds is given. Indeed, the presence of the meso aromatic spacer allows the safe consideration of a negligible contribution of the porphyrin ring on the rotational barriers.
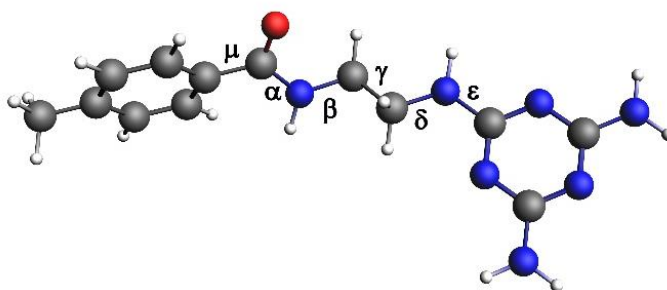

Figure 2.4. Labelling of the bonds for which the PES scan has been performed. μ represents the bond with the meso substituent.

As expected, rotations on the α and ε bonds are hampered, at standard conditions, by energy barriers around 17–20 kcal/mol. Nonetheless, rotations around the μ, β, γ, and δ bonds require about 4–6 kcal/mol, which indicates the

possibility of a virtually free rotation around these bonds. This flexibility allows the inference of the easy occurrence of different conformations of the porphyrin derivative. In this context, two main typologies of conformations have been considered as opposite conformational paradigms. They are shown in Figure 2.5 and are labelled as chair-like (CL) and as boat-like (BL) conformations, respectively.

CL

BL
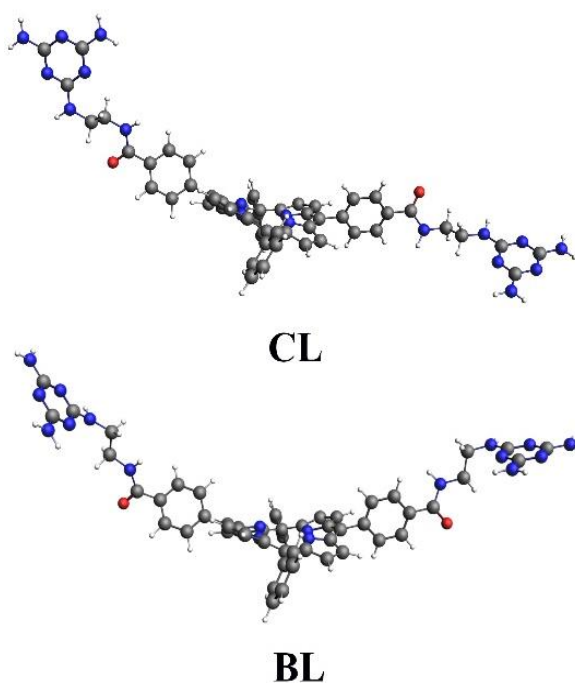
Figure 2.5. Starting geometries of the chair-like (CL) and as boat-like (BL) conformations.

CL conformation is recognized as suitable to arrange the framework in Scheme 2.2, hence, able to coordinate different Au NPs. In the BL conformation, by the back-folding of the porphyrin substituents, the two substituents can virtually act as a tweezer by bonding to just one Au NP. On these grounds, we optimized the corresponding structures by considering the starting geometries

reported in Figure 2.5. The optimized geometries are reported in Figure 2.6 and indicate that the CL conformation tends to be more preferred. Indeed, the optimized BL conformation, Figure 2.6, displayed a configuration similar to that of the CL one, but the optimized CL conformer resulted in 1.6 kcal/mol more stable than the optimized BL one. A Boltzmann analysis of the population ratio indicated that CL represents 95% of the total population among these two conformers. Consequently, the possibility of the back-folding of the porphyrin substituents so that the two substituents can virtually act as a tweezer by bonding to just one Au NP may be related just to 5% of the porphyrin molecules.

To summarize, though the porphyrin substituents have some rotational degrees of freedom (bonds μ, β, γ, δ, in Figure 2.4), the CL conformation is more likely. This result corroborates our reaction path in Scheme 2.2.
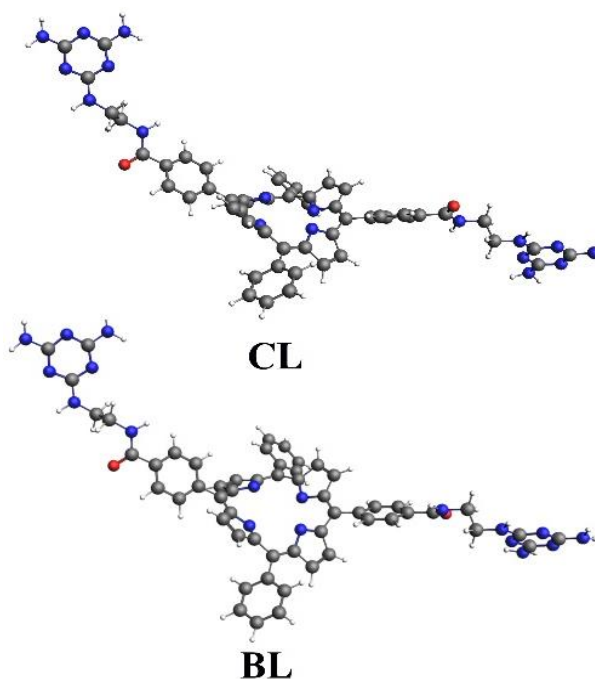
Figure 2.6. Optimized geometries of the chair-like (CL) and boat-like (BL) conformations.

2.4 Characterization of Gold–Porphyrin

The study of the electronic structure of the Au NPs–porphyrin nanostructures is fundamental to investigate the Au – porphyrin electron interactions, which are the basis of the coupling of the plasmon Au resonance with the porphyrin emission, and X-ray photoelectron spectra (XPS) represents the most suited tool to accomplish this task.[103, 118-120]

Figure 2.7 shows the XP spectra of pure Au NPs and Au NPs–porphyrin nanostructures, in the Au 4f binding energy region. The $4f_{7/2,5/2}$ levels for the Au NPs before any porphyrin addition were observed at 84.0 and 87.7 eV, respectively.[83, 121] These states lie at 82.8 and 86.5 eV (3.7 eV spin-orbit coupling), respectively, for the Au NPs–porphyrin nanostructures, and indicate the presence of Au^0 states. Therefore, the considerably decreased values are in tune with the strong electron-donating capability of this di-triazine porphyrin to the positively charged Au NPs surfaces.
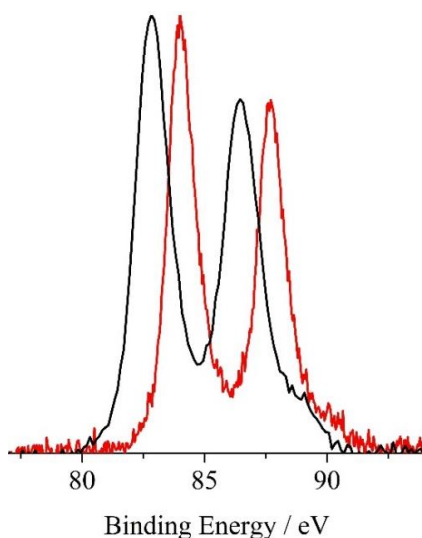
Binding Energy / eV

Figure 2.7. Al-Kα excited XPS of the pure Au NPs solution (red line) and Au NPs–porphyrin system (black line) in the Au 4f binding energy region.

Figure 2.8 shows the XPS of the Au NPs–porphyrin system in the C 1s binding energy region. An accurate fitting of this spectrum required five Gaussian components centered at 285.0, 285.5, 286.7, 287.9, and 288.9 eV. The first component (285.0 eV) is due to both aliphatic and aromatic backbones.[118-120] The peaks at 285.5 and 286.7 eV are assigned to the C–N and C=N groups, respectively.[120, 122] The peak at 287.9 eV is assigned to the HN-C=N(-NH) and N-C=N(-NH$_2$) triazine groups.[122] The peak at 288.9 eV is assigned to the carbon of the amide group (Ar-CO-NH).[122]

Figure 2.8. Al-Kα excited XPS of the Au NPs–porphyrin system in the C 1s binding energy region. The green, blue, magenta, orange, and dark yellow lines refer to the 285.0, 285.5, 286.7, 287.9, and 288.9 eV components; the cyan line refers to the background and the red line superimposed on the experimental black profile refers to the sum of all Gaussian components.

Figure 2.9 shows the XPS of the Au NPs–porphyrin system in the N 1s binding energy region. A careful fitting of the experimental profile required five Gaussian components at 397.9, 398.6, 399.5, 399.9, and 400.4 eV. The

component at 397.9 eV is assigned to two ionization of the two porphyrin non-protonated imine nitrogen core, that at 398.6 to the six triazine ring nitrogen atoms, that at 399.5 eV is assigned to the four $-NH_2$ triazine substituents, that at 399.9 eV is assigned to the two porphyrin protonated pyrrole nitrogen core and to the two $-NH-$ groups bound to the triazine moiety and, finally, that at 400.4 eV is consistent with the two O=C(Ar)-NH- amide functionalities.[83, 120, 122-126]
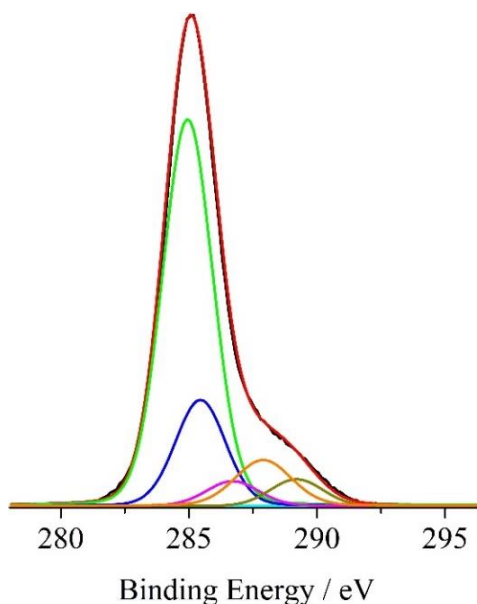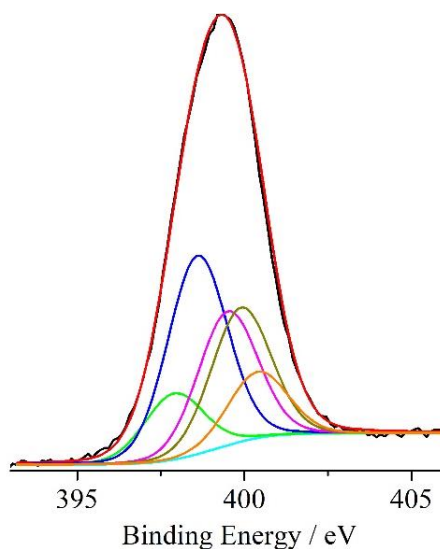

Figure 2.9. Al-Kα excited XPS of the Au NPs–porphyrin system in the N 1s binding energy region. The orange, dark yellow, magenta, blue and green lines refer to the 400.4, 399.9, 399.5, 398.6 and 397.9 eV components; the cyan line refers to the background and the red line superimposed to the experimental black profile refers to the sum of all Gaussian components.

The transmission electron microscopy (TEM) of the conjugated Au NPs–porphyrin system is reported in Figure 2.10. While single and highly dispersed Au nanoparticles, having a mean radius of about 5 nm, have been obtained from the reduction of the tetrachloroauric acid with sodium citrate (Figure 2.10a), large organized (even though not apparently ordered) nanoscale assemblies of Au nanoparticles are evident in the presence of 5,15,-Di(phenyl) 10, 20-Di-

benzamide, *N*-ethyl, *N*-1,3,5 Tri-aminotriazine, 21H,23H-porphine molecules (Figure 2.10b,c). The role of this porphyrin in the formation of the new composite assembly, consisting of Au NPs covalently anchored to each other, is evident in Figure 2.10d, where the ~3 nm texture surrounding the Au NPs represents the "glue" for the covalent assembly of gold nanoparticles.
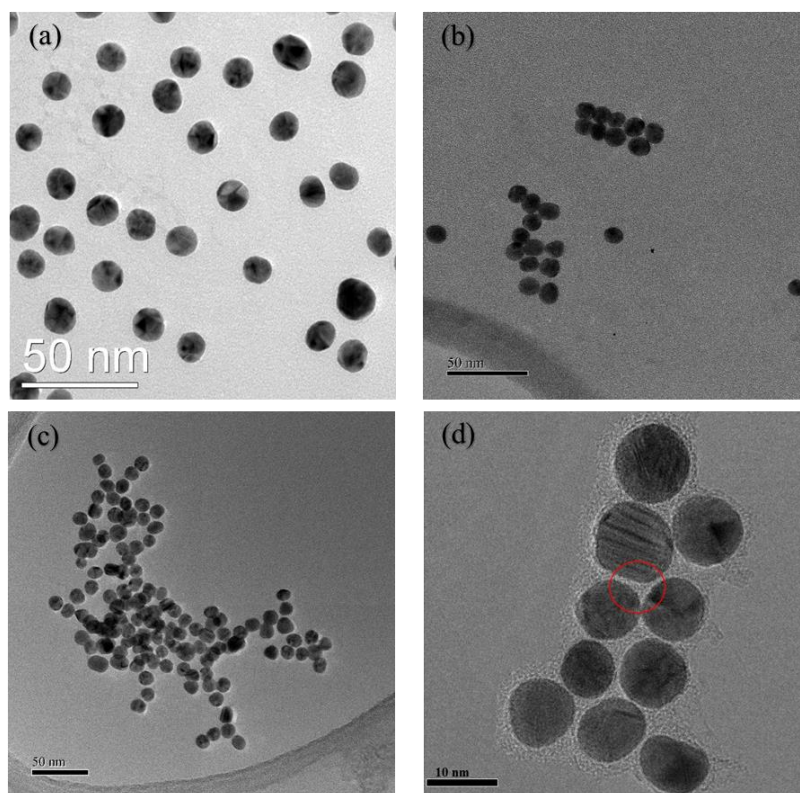
Figure 2.10. TEM images of conjugated gold – porphyrin nanostructures: (**a**) Au nanoparticles obtained from the reduction of the tetrachloroauric acid with sodium citrate; (**b**) Au NPs obtained from 100 µL of an Au NPs aqueous 1.97×10^{-7} M solution diluted with 2 mL of CH$_3$OH upon the addition of 240 µL of a 2.07×10^{-5} M porphyrin CH$_3$OH solution; (**c**) Au NPs obtained from 100 µL of an Au NPs aqueous 1.97×10^{-7} M solution diluted with 2 mL of CH$_3$OH upon the addition of 450 µL of a 2.07×10^{-5} M porphyrin CH$_3$OH solution; (**d**) higher magnification of the Au NPs obtained from 100 µL of an Au NPs aqueous 1.97×10^{-7} M solution diluted with 2 mL of CH$_3$OH upon the addition of 450 µL of a 2.07×10^{-5} M porphyrin CH$_3$OH solution; the red circle represents the representative area investigated with EDX to obtain Figure 2.11.

The chemical composition of these assemblies was analyzed by Energy dispersive X-ray (EDX, Figure 2.11) and the results are indicative of Au nanoparticles surrounded by a thin layer of a nitrogen-containing compound, consistent with a ~ 3 nm, layer of porphyrin molecules. Therefore, the bi-functional porphyrin molecules work as covalent bridges between different gold nanoparticles.
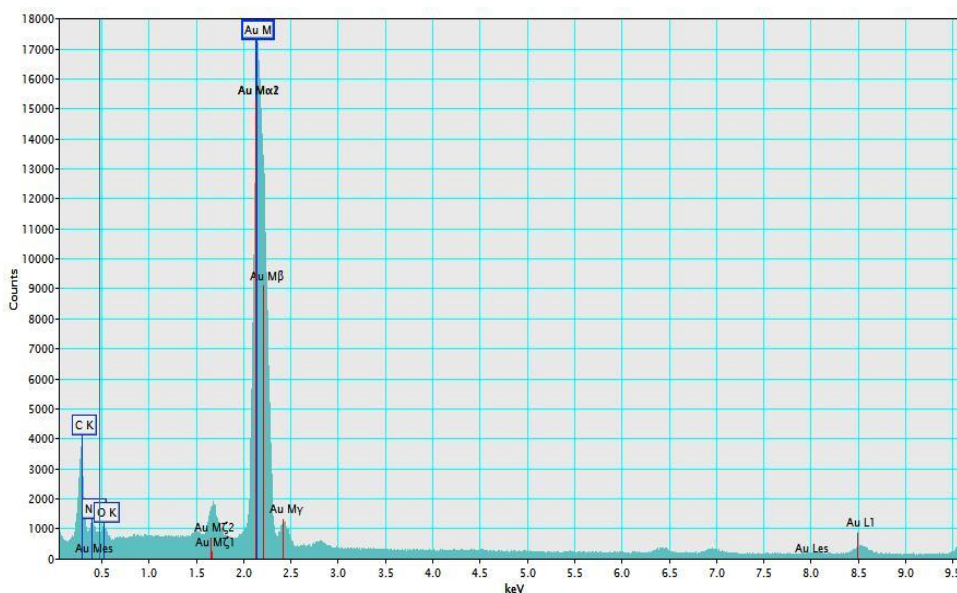
Figure 2.11. EDX spectrum of the Au NPs conjugated with the 5,15-Di(phenyl) 10, 20 -Di-benzamide, N-ethyl, N- 1,3,5 Tri-aminotriazine, 21H,23H-porphine.

Dynamic light scattering (DLS) analysis of these two solutions (Figure 2.12) showed two radius distributions centred at 12 nm and 135 nm for the Au NPs and Au NPs–porphyrin nanostructures, respectively. These values confirm the increasing size of the Au nanostructures upon the porphyrin bonding. However, they strongly depend on the relevant number of solvent molecules that solvate the NPs. In fact, the DLS theory states that the electric dipole layer of both capping layer and solvent adhering to the surface of the particles influences their

movement in the medium. Thus, the hydrodynamic radius gives information of the inorganic core along with any coating material and solvent layer attached to the particle. For example, it has been reported that the diameter of some magnetite (Fe_3O_4) particles was found to be 25 nm from TEM while their average hydrodynamic size was 164 nm from DLS.[127]
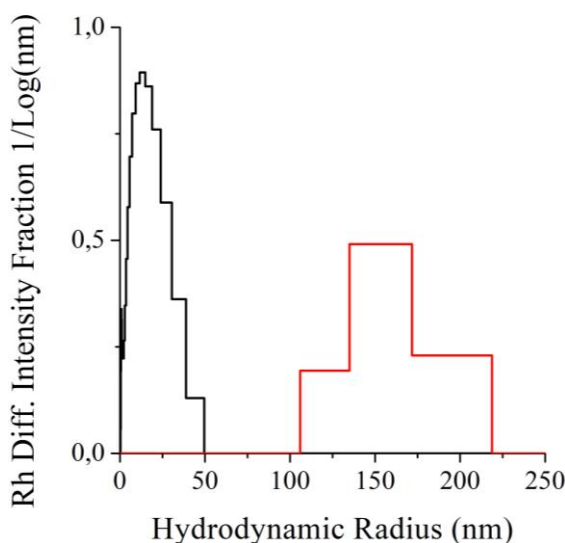
Figure 2.12. DLS measurements for the $6.57 \cdot 10^{-9}$ M Au NPs (black line) and $6.22 \cdot 10^{-6}$ M Au NPs–porphyrin nanostructure (red line) methanol solutions.

2.5 Properties of Gold–Porphyrin Nanostructures

The main purpose of our study was the nanoscale self-assembly of Au NPs by means of porphyrin molecules having two functional groups in opposite positions, useful to connect these Au NPs to each other. It is well known that Au NPs can either be luminescent or plasmonic and this hampers many possible applications as an optical material. Therefore, the goal we would achieve with this final functional architecture is not only to maintain the strong surface plasmon resonance, typical of Au nanoparticles, but also the conservation of a

strong luminescence signal, coming from porphyrin molecules. Additionally, this property is strongly related to the absence of porphyrin aggregates which causes luminescence quenching. Obviously, we can observe and follow variations of the Au NPS surface plasmon resonance with absorbance spectra and detect the porphyrin fluorescence with emission measurements.

Figure 2.13 shows the UV-Vis spectrum of the as-synthesized aqueous Au NPs solution. The Au surface plasmon resonance (SPR) peak lies at 520.6 nm (Abs = 1.5). By using a literature data for the related extinction coefficient (ε = $7.6 \cdot 10^6 \, M^{-1} \cdot cm^{-1}$), we obtained a 1.97×10^{-7} M concentration value for this Au NPs solution.[36]
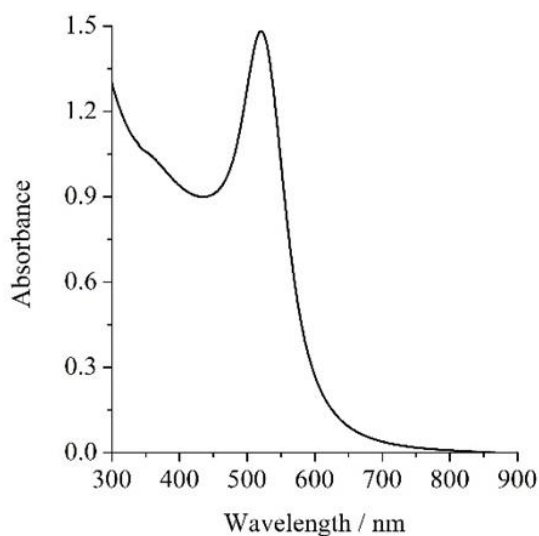
Figure 2.13. UV-Vis absorbance spectrum of the as synthesized aqueous Au NPs 1.97 $\times 10^{-7}$ M solution.

Figure 2.14 shows the absorbance spectra of 100 µL of this Au NPs aqueous solution, diluted with 2 mL of CH_3OH (V_{tot} = 2.1 mL), and those upon the successive addition of aliquots of a 2.07×10^{-5} M porphyrin CH_3OH solution, up to a final added porphyrin volume of 900 µL, corresponding to 1.86×10^{-8}

mol, (final total volume 3 mL). The Au SPR peak, before any porphyrin addition, almost does not move (520.4 nm, Abs = 0.14) with respect to the position observed for the aqueous solution, but the calculated extinction coefficient now is $\varepsilon = 1.5 \cdot 10^7\ M^{-1} \cdot cm^{-1}$ for this Au NPs CH$_3$OH solution, almost double, once the dilution from 100 µL up to 2.1 mL is taken into account.
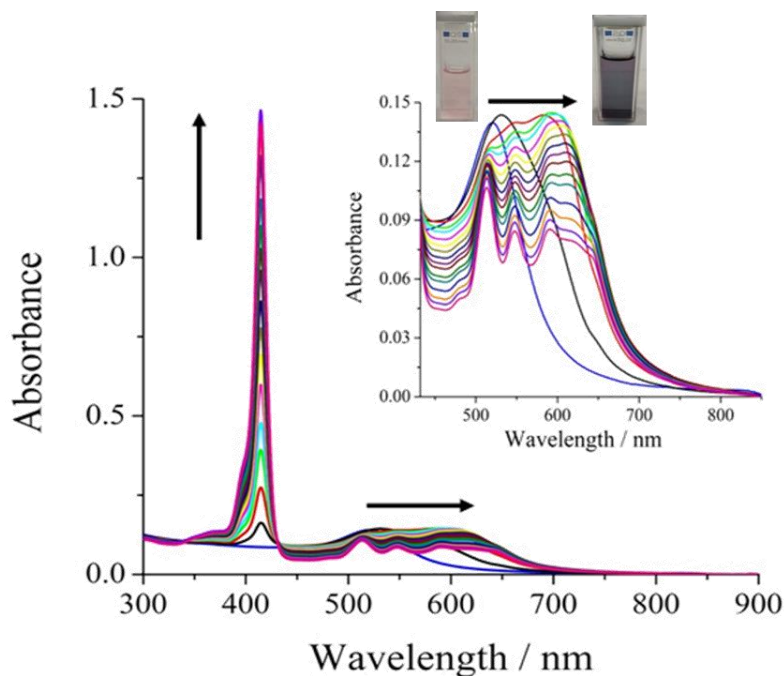
Figure 2.14. UV–vis absorbance spectra of 100 µL of an Au NPs aqueous 1.97×10^{-7} M solution diluted with 2 mL of CH$_3$OH (blue line), and upon the addition of 40 (black line), 80 (red line), 120 (green line), 160 (cyan line), 200 (magenta line), 240 (yellow line), 280 (dark yellow line), 320 (navy line), 360 (purple line), 400 (wine line), 450 (olive line), 500 (dark cyan line), 600 (royal line), 700 (orange line), 800 (violet line), and 900 (pink line) µL aliquots of a 2.07×10^{-5} M porphyrin CH$_3$OH solution (final total volume 3 mL). All the spectra were corrected for the volume variation. Inset: expanded scale of the Au NPs plasmon–porphyrin Q-bands region. It can be observed the colour variation from red to blue of the Au NPs solution, following the addition of porphyrin.

34

As the titration goes on, it is evident the progressive and monotonic increase in the Soret at 414.8 nm and Q-bands at 513.6, 547.8, 590.6, and 642.0 nm. The Soret band of a CH_3OH 2.016×10^{-6} M pristine porphyrin solution (Figure 2.15, Abs = 0.60, ε = 289300 M^{-1} cm^{-1}) appears at 414.4 nm and the related Q-bands are at 512.8, 546.8, 589.2, and 644.0 nm, thus, indicating about 1 nm red shift upon the interaction with the Au NPs. Therefore, the light-induced surface plasmon resonance, coherent collective oscillation of the valence electrons, and porphyrin absorptions result in an intense band over a wide wavelength range and this system can mediate excitation energy transport, e.g., to mimic a natural "light-harvesting" function.

Figure 2.15. UV-Vis absorbance spectrum of a 2.016×10^{-6} M porphyrin CH_3OH solution.

The "footprint" of the porphyrin molecule was calculated by a Molecular Mechanics optimization, with the HypChem^TM (v8.0.7.) code, using the so-called MM+ as the force 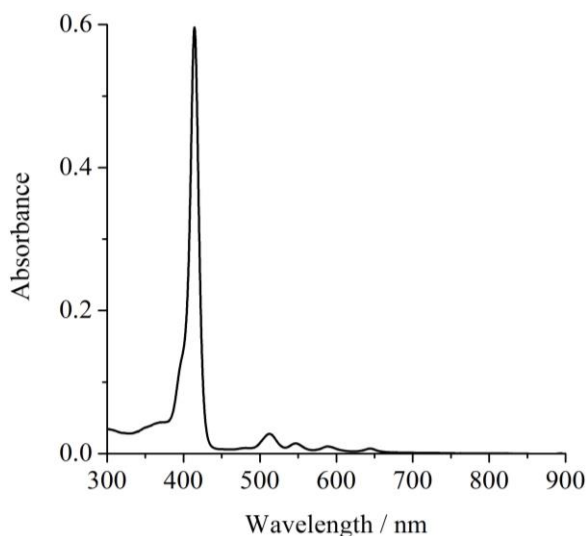field. This software optimizes the molecular geometry (length and angle bonds) to obtain a minimum of the total energy. In addition,

non-covalent interactions such as hydrogen bonds, van der Waals interactions, steric hindrance, and electrostatic interactions were included. In our case, we used a conjugated gradient (Polak–Ribière) to obtain a minimum of energy, setting the end of the optimization when the gradient energy between the optimized structure was lower than 0.01 kcal/mol.

The concentration of the porphyrin in the final solution containing the self-assembled Au NPs–porphyrin nanostructures is 6.22×10^{-6}, about 950 times larger than that of the Au NPs (100 µL 1.97×10^{-7} M diluted to 3 mL = 6.57×10^{-9} M), thus, indicating the possibility of a total Au surface coverage with porphyrin molecules. In fact, each Au nanoparticle with a ~5 nm radius has a surface area of 314 nm^2 (31.400 Å^2), while the footprint of the porphyrin molecule, assumed perpendicular to the Au NP surface (95% of the total porphyrin population) and calculated with a MM+ method, is about 65 Å^2, thus, confirming the possibility to accommodate about 480 porphyrin molecules per Au nanoparticle. Therefore, this 480/1 porphyrin/Au NP ratio was obtained upon the addition of 450 µL of the porphyrin solution to the starting Au NPs aqueous 1.97×10^{-7} M solution diluted with 2 mL of CH_3OH. It is important to note that in these exact conditions, we observed the maximum emission intensity of the Au NPs–porphyrin system (vide infra). The literature data show that the binding of Au NPs with luminescent dyes could lead to strong coupling of the plasmonic mode with molecular modes, but, in the present case, no peaking splitting was observed because of the mismatch resonance peak between AuNP and the porphyrin molecule.[128-130]

Figure 2.16 shows the emission spectra of the above solution (100 µL of an Au NPs aqueous $1.97 \cdot 10^{-7}$ M solution diluted with 2 mL of CH_3OH, and those

upon the successive addition of aliquots of a $2.07 \cdot 10^{-5}$ M porphyrin CH_3OH solution, up to a final added porphyrin volume of 900 µL). The emission intensities of both 648 and 716 nm bands reach maximum values upon the addition of 450 µL of the porphyrin solution (9.3×10^{-9} mol; 3.652×10^{-6} M) and in these conditions, the porphyrin concentration corresponds to that for the total Au surface coverage. It is also important to stress that at each porphyrin concentration obtained in our experiments, the porphyrin emission intensity was always lower than that observed for pure porphyrin solutions with the same concentrations (Figure 2.17), and this is due to the well-known quenching effect of the Au NPs. In fact, after the addition of 240 and 450 µL of the porphyrin solution, we noted a 16% and 34% emission decrease, respectively.

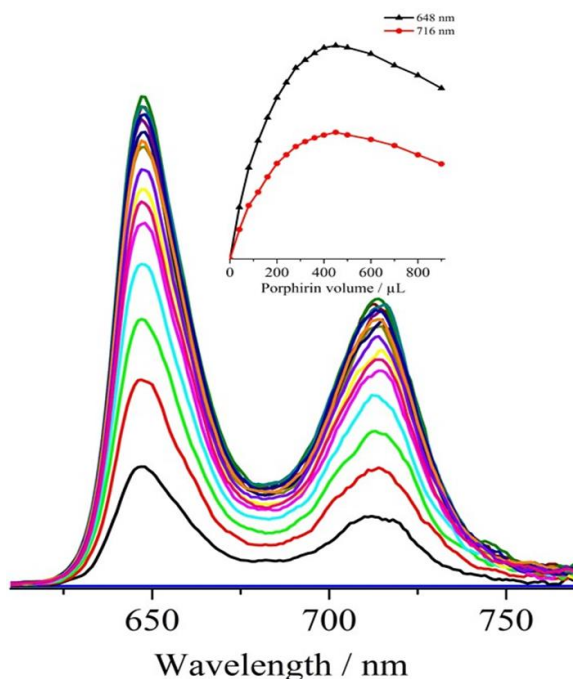**Figure 2.16**. Fluorescence spectra (λex = 410 nm) of 100 µL of an Au NPs aqueous 1.97×10^{-7} M solution diluted with 2 mL of CH_3OH (blue line superimposed to the x-axis), 40 (black line), 80 (red line), 120 (green line), 160 (cyan line), 200 (magenta line),

240 (yellow line), 280 (dark yellow line), 320 (navy line), 360 (purple line), 400 (wine line), 450 (olive line), 500 (dark cyan line), 600 (royal line), 700 (orange line), 800 (violet line), and 900 (pink line) µL aliquots of a 2.07×10^{-5} M porphyrin CH_3OH solution (final total volume 3 mL). All the spectra were corrected for the volume variation. Inset: intensity behaviour of the emission maxima upon the porphyrin additions.
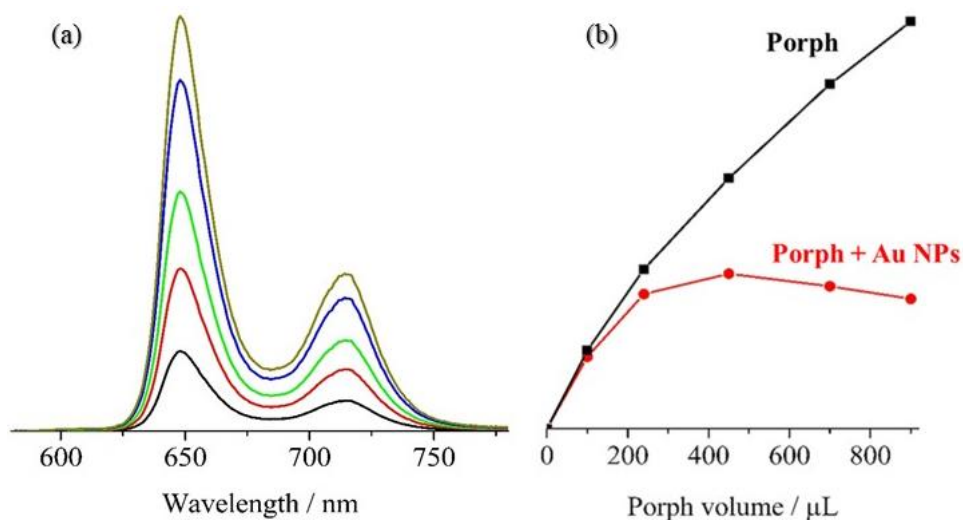
Figure 2.17. a) Trend of the luminescence spectra of the porphyrin CH_3OH solution at different concentrations: $9.41 \cdot 10^{-7}$ M, black line; $2.13 \cdot 10^{-6}$ M, red line; $3.66 \cdot 10^{-6}$ M, green line; $5.18 \cdot 10^{-6}$ M, blue line; $6.22 \cdot 10^{-6}$ M, dark yellow line and b) Comparison between the PL intensities of the porphyrin CH_3OH solutions (black line) and those obtained during the Au NPs titration at different concentrations (red line): $9.41 \cdot 10^{-7}$ M, black line; $2.13 \cdot 10^{-6}$ M, red line; $3.66 \cdot 10^{-6}$ M, green line; $5.18 \cdot 10^{-6}$ M, blue line; $6.22 \cdot 10^{-6}$ M, dark yellow line.

An identical behaviour was observed for the centrifuged Au NPs systems deposited on quartz substrates (Figure 2.18), thus, stressing that the luminescence is maintained at the solid-state and that the maximum luminescence is observed upon the addition of 450 µL of a 2.07×10^{-5} M porphyrin CH_3OH solution to 100 µL of an Au NPs aqueous 3.66×10^{-7} M solution diluted with 2 mL of CH_3OH (final total volume of the solution 3 mL).
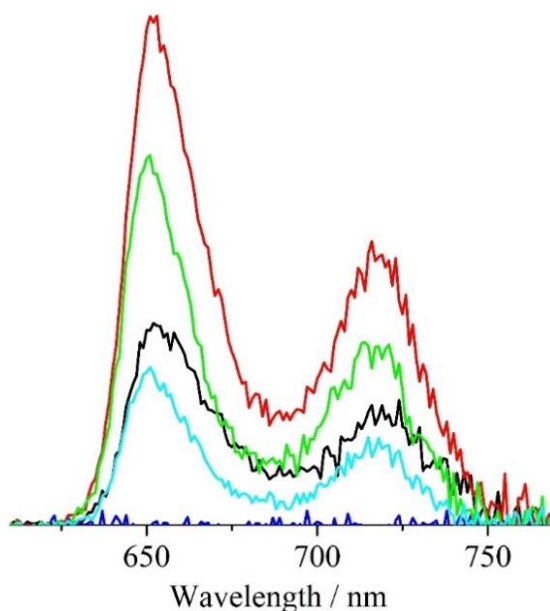
Figure 2.18. Fluorescence spectra (λ_{ex} = 410 nm) of the Au NPs–porphyrin systems centrifuged and deposited on quartz substrates. Starting Au NPs (blue line), centrifuged solutions upon the addition of 240 (black line), 450 (red line), 700 (green line), and 900 (cyan line) µL aliquots of a 2.07×10^{-5} M porphyrin CH_3OH solution (final total volume of the solution 3 mL).

The photoluminescence of emitting dyes chemically bound to Au NPs has already been explored.[131-136] Results are always indicative of pronounced fluorescence quenching of the given dyes. In some studies, it emerged that quenching was caused not only by an increased nonradiative rate, but equally important, by a drastic decrease in the dye's radiative rate.[131] Additionally, reduced fluorescence, for particular Au NPs–dye distances, almost exclusively governed by a phase-induced suppression of the radiative rate, has been shown.[132] This behaviour has been confirmed and the strongly distance-dependent fluorescence quenching in Au NPs covered with some polyelectrolytes has been ascribed to the fact that gold nanoparticles decrease

the transition probability for radiative transitions.[133] Furthermore, it has been reported that the quenching behaviour may be consistent with $1/d^4$ separation distance from dye to the surface of the nanoparticle and that energy transfer to the metal surface is the dominant quenching mechanism.[134] Therefore, to maintain the dye's emission intensity, Au NPs and the emissive dye should be distant.[135] Consequently, in our system, upon the addition of 450 µL of the porphyrin solution, the porphyrin molecules extensively reticulate with the gold nanoparticles to produce an organized Au NPs–porphyrin network and this partially quenches the porphyrin emission because the Au NPs and porphyrin molecules are close each other. In addition, this experimental observation confirms that the porphyrin molecules bond different Au NPs, since, if a relevant number of porphyrin molecules would back-fold and bond the same Au NPs, the emission quenching would be severe because of the reduced Au NPs–porphyrin distance. This quenching is rather a plasmonic quenching effect as already observed in many cases where the Au NPs are mixed with fluorescent molecules. In fact, (vide infra), the porphyrin molecules alone do not show any concentration-dependent aggregation nor quenching of absorption and luminescence at the concentrations used in the present experiments and, in contrast, in this Au NPs–porphyrin system, we noted an increase in the porphyrin ε value (vide infra). As a result, a delicate balance of Au NPs and porphyrin concentration will allow the synthesis of an organized Au network that remains plasmonic and emissive, and we observed the maximum emission intensity upon the addition of 450 µL of the porphyrin solution, exactly that needed for the total Au surface coverage. After the addition of 450 µL of the porphyrin solution, all Au NPs are covered with porphyrins and the decrease in luminescence intensity,

observed upon further porphyrin addition, is now due to some possible interactions between the porphyrin molecules in solution that can interact with those linked to Au NPs and be partially responsible for the observed optical behavior.

Figure 2.19a shows three selected spectra of Figure 2.14, in particular, the absorbance spectrum of 100 µL of an Au NPs aqueous 1.97×10^{-7} M solution diluted with 2 mL of CH_3OH (black line), that after the addition of 240 µL of a 2.07×10^{-5} M porphyrin CH_3OH solution (red line), and that after the addition of 450 µL of this porphyrin CH_3OH solution (blue line). The comparison of these three spectra reveals that the first two porphyrin Q-bands are evident and slightly affected by the rather broad Au NPs surface plasmon resonance that, in contrast, moved to 612 nm (already upon the addition of 240 µL of porphyrin), thus, overlapping with the two higher wavelength Q-bands. In principle, this red-shift of the Au plasmon may be due either to aggregation or a strong coupling of the two systems, but the Au NPs–porphyrin bonding distance is not close enough for strong coupling, being the length (distance between the two opposite triazine moieties) of the porphyrin molecule ~30 Å.[128-130] In this condition (porphyrin conc. 1.95×10^{-6} M), the porphyrin shows an ε value of 353800 M^{-1} cm^{-1} with an increase of 22%, with respect to the starting 289300 M^{-1} cm^{-1} value (for the 2.016×10^{-6} M solution). Since it is well known that porphyrin aggregation causes a decrease in the molar extinction coefficient, this experimental observation strongly suggests that, after the addition of 240 µL of a 2.07×10^{-5} M porphyrin CH_3OH solution to the Au NPs solution, there are no porphyrin aggregates in solution and all these molecules are involved in the formation of the Au NPs–porphyrin nanostructures. After the addition of 450 µL of a 2.07 ×

10^{-5} M porphyrin CH$_3$OH solution to that of the Au NPs, we just noted an overall absorbance intensity decrease (blue line). A similar trend was observed for the centrifuged same Au NPs–porphyrin solutions deposited on quartz substrates (Figure 2.19b), being the starting Au NPs plasmon resonance at 559 nm and that after the addition of 450 µL of the porphyrin CH$_3$OH solution at 595 nm.
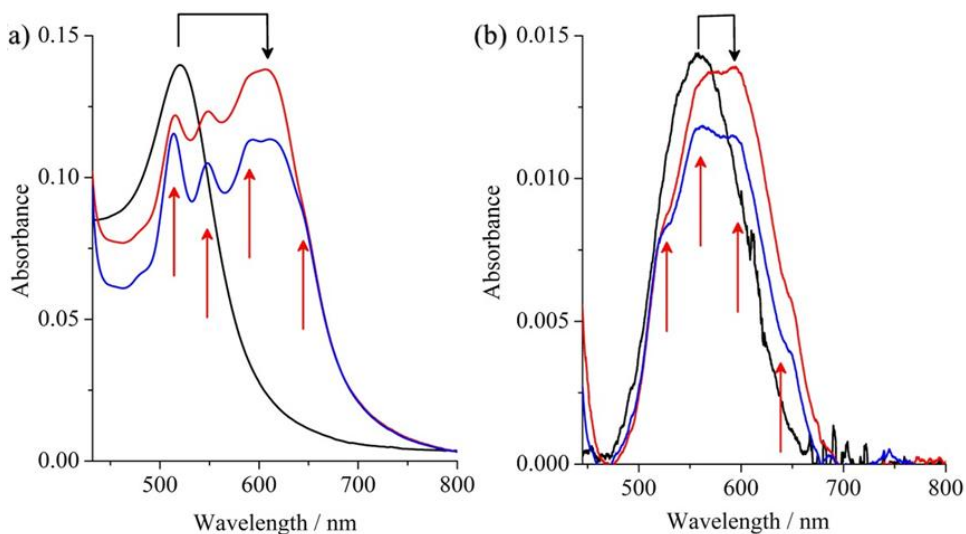
Figure 2.19. UV–vis absorbance spectra of (a) 100 µL of an Au NPs aqueous 1.97×10^{-7} M solution diluted with 2 mL of CH$_3$OH (black line), upon the addition of 240 µL of a 2.07×10^{-5} M porphyrin CH$_3$OH solution (red line, corrected for the volume variation), and upon the addition of 450 µL of a 2.07×10^{-5} M porphyrin CH$_3$OH solution (blue line, corrected for the volume variation), and of (b) the centrifuged same Au NPs–porphyrin solution deposited on quartz substrates, in the 430–850 nm wavelength range. The red arrows indicate the four Q-bands at 513.6, 547.8, 590.6, and 642.0 nm and the black arrow indicates the Au NPs surface plasmon resonance that, in solution, moved from 520.4 to 612 nm and on quartz substrates moved from 559 to 595 nm.

It is important to point out that, in these conditions, we have obtained Au NPs–porphyrin nanostructures showing both strong surface plasmon resonance and strong luminescence signals. Therefore, the gold–porphyrin assembly

continues to show the surface plasmon resonance that is typical of semiconducting Au nanoparticles and that, in contrast, disappears on bulk gold.

Consequently, the whole Au NPs–porphyrin assembly behaves as a semiconductor, thanks to the extensive electron conjugation granted by the porphyrin molecules that work as the wiring between the different Au NPs.

Conclusions

In this chapter, the bottom-up approach was used for the fabrication of nanoscale assemblies of Au nanoparticles self-assembled through a new bi-functional porphyrin molecule. In total, 95% of the porphyrin molecules are bound to the surface of gold NPs by one triazine side/leg and some of them, lying close to the core-to-core axis, are bridging different gold nanoparticles. This functional architecture exhibits a strong surface plasmon, due to the Au nanoparticles, and a strong luminescence signal coming from porphyrin molecules, thus, giving a new optical material with unique characteristics, like those of highly organized networks. Therefore, the present network organization continues to grant the Au surface plasmon resonance typical of Au single nanoparticles, while it is well known that bulk Au loses this property, and also grants the porphyrin luminescence that, in contrast, is lost in aggregated porphyrin systems because of π-π stacking interactions.

In summary, this artificial Au NPs network may be used for plasmon-enhanced fluorescence, heat generation, photocatalysis, nonlinear optics, solar cells, nanofluidics, photoacoustic, photothermal imaging, cancer therapy, drug delivery, nanotherapeutics, etc., under atmospheric conditions, since our system is not reactive to air nor to water and does not need to be stored in a vacuum or inert gas.

Chapter 3

Optical Properties of Emitting Dyes Bound to Au Nanostructures

In the previous chapter, we focused our attention on fabricating nanoscale assemblies of Au nanoparticles self-assembled through a novel bi-functional porphyrin molecule useful for plasmon-enhanced fluorescence, photocatalysis and photothermal imaging applications. Other important luminescent systems are lanthanide complexes. In fact, lanthanides have exceptional luminescent characteristics such as high luminous intensity, long fluorescence lifetime, large Stokes shifts and sharp emission profiles from the f−f electron transitions which make them useful in fluorescence, DNA hybridization, cell activity, bioimaging assays etc..[137-145]

Besides, photoluminescence (PL) of trivalent europium ions, upon ultraviolet light irradiation, is involved in efficient light-conversion molecular devices.[146] In addition, because of the effective intramolecular energy transfer from the coordinated ligands to the luminescent central lanthanide ion, emission of Eu(III) results in being strongly influenced by its environment.[147, 148]

As mentioned above, gold nanoparticles can alternatively be luminescent or plasmonic. Lanthanide complexes bound to nanometre-sized gold nanoparticles

could overcome this problem. In this context, we experimentally investigated luminescence quenching for europium complexes bound to Au nanostructures. We have studied this effect for two very similar europium complexes, one of which can covalently assemble on gold nanoparticle surfaces while the other cannot do it. We found that the Au nanostructures covalently surrounded by the Eu complex remained plasmonic and luminescent, while a total emission quenching was observed for the Eu complex not suited to covalent interact with the Au nanostructures. This behaviour was rationalized in terms of through bond vs. through space interactions between the Eu complex and the Au nanoparticles. The present nanostructures can be useful for all applications requiring plasmonic emitters.

3.1 Gold−Eu Nanostructures: Through Bond vs. Through Space Interactions

Nanostructures comprised of emissive europium (III) complexes[143] on plasmonic gold nanoparticles[28, 29, 96, 121, 149-151] could combine their distinctive properties thus greatly enhancing the range of optical applications.[152-160] Unfortunately, pronounced fluorescence quenching of emitting dyes chemically bound to Au NPs has already been observed.[131-136] In some studies, it emerged that quenching was caused not only by an increased non-radiative rate but, equally important, by a drastic decrease in the dye's radiative rate.[131] Additionally, it has been shown reduced fluorescence, for particular Au NPs – dye distances, governed by a phase-induced suppression of the radiative rate.[132] The strongly distance-dependent fluorescence quenching in Au NPs covered with some polyelectrolytes has been ascribed to the fact that gold nanoparticles decrease the transition probability for radiative transitions.[133] Furthermore, it has been reported that the quenching behaviour may be a function of the separation distance from dye to the surface of the nanoparticle, and that energy transfer to the metal surface is the dominant quenching mechanism.[134-136]

In contrast, enhanced luminescence for emissive chromophores is an optical phenomenon that involves two or more associated photo-physical events such as Rayleigh scattering and surface plasmon resonance. Metallic nanostructures as Au or Ag NPs show surface plasmons that can experience resonance with an external electromagnetic source, thus enhancing optical effects. Apart from the plasmon enhancement effects observed in localised surface regions of

nanomaterials such as Au NPs, switching of a part of this energy via dipole-dipole interactions can enhance luminescence and light scattering in the emissive molecules in close proximity. This plasmon resonance energy transfer strongly depends upon the overlap of the plasmon frequency of the metallic nanomaterials and the electronic states of the emissive molecule.[161-165] Therefore, a delicate balance between these two quenching and enhancing effects will govern the final optical properties of emissive chromophores - noble metal nanomaterial hybrids.

On this basis, in the present study, we investigated the optical properties of two very similar, high stable, Eu-complexes in solutions of Au nanostructures: tris(dibenzoylmethane) mono(5-amino-1,10-phenanthroline)europium (III) (**1**, Figure 3.1), hereafter EuNH$_2$@Au, and tris(dibenzoylmethane) mono(1,10-phenanthroline)europium (III) (**2**, Figure 3.2), hereafter Eu@Au. Results indicated that covalent assembly in EuNH$_2$@Au granted a better optical performance to the final nanostructures that remained both plasmonic and luminescent and this behaviour was rationalized in terms of through bond vs. through space interactions. To our knowledge, this represents one of the few cases of europium - Au NPs plasmonic and luminescent nanostructures.[152-160]
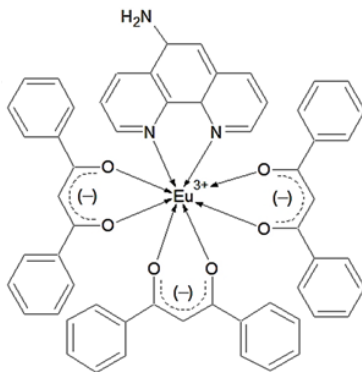

Figure 3.1. Structure of the tris(dibenzoylmethane) mono(5-amino-1,10-phenanthroline)europium (III) complex (**1**).
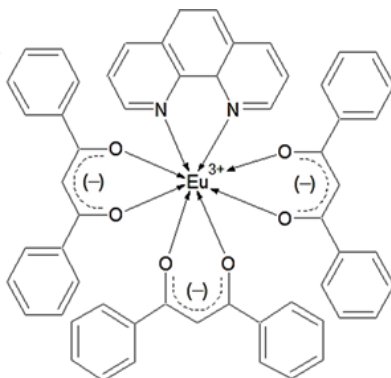
Figure 3.2. Structure of the tris(dibenzoylmethane) mono(1,10-phenanthroline)europium (III) complex (**2**).

3.2 Synthesis of the Eu@Au and EuNH$_2$@Au

The synthesis of the Au NPs solution was performed as reported in the previous chapter.[57] These Au NPs resulted in high stability being the UV-vis spectrum recorded after seven months from the synthesis identical to that obtained soon after the synthesis (Figure 2.13).

Then, we added 90 µL of acetonitrile to 10 µL of this previous solution, thus obtaining 100 µL of a 1.97×10^{-8} M (1.97×10^{-12} mol) Au NPs (CH$_3$CN/H$_2$O 9:1 v/v) solution. At that point, we dropwise added (in 350 min) these 100 µL of the 1.97×10^{-8} M Au NPs solution to 1.5 mL of **1** 1.77×10^{-5} M (2.65×10^{-8} mol) CH$_3$CN solution, to get EuNH$_2$@Au covalent nanostructures, thanks to the ability of the –NH$_2$ group of this Eu complex to coordinated Au NPs.[36, 57-59] A similar synthesis was performed using a solution of **2**, that differs from **1** just because of the absence of the –NH$_2$ group and therefore is not able to covalently coordinate the Au NPs, to get Eu@Au. Note that both total Au NPs and mols of

each different Eu (III) complex are identical in the two experiments. In addition, the final total volume for both experiments was 1.6 mL.

3.3 Characterization and Properties of the Eu@Au and EuNH₂@Au Nanostructures

After having preliminary reduced Au^{3+} with sodium citrate to obtain Au NPs, we decorated them with **1** or **2** complex molecules.[56] In particular, **1** has an amine group useful to displace the citrate anion and covalently bind the Au NPs surface (Scheme 3.1), as already reported for similar systems.[36, 57-59] In contrast, this group is absent in **2** that cannot covalently bind the Au NPs.[66, 166-168]
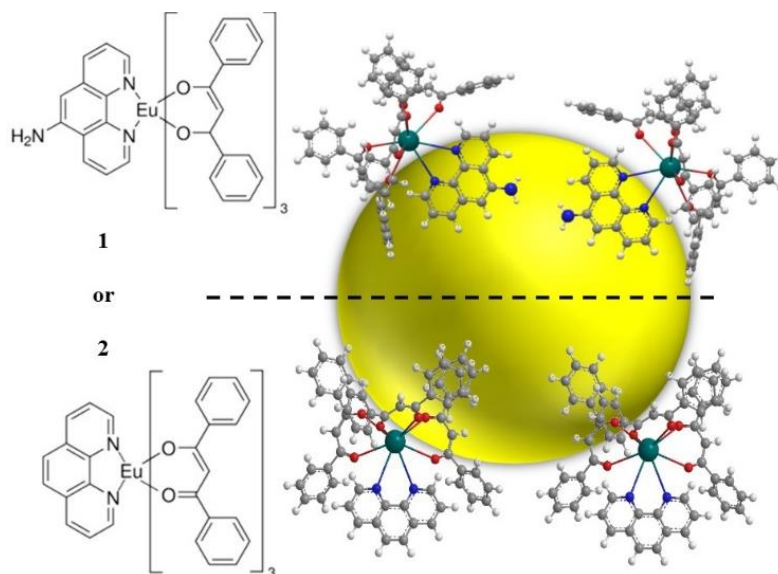
Scheme 3.1. Reaction pathway for the assembly of **1** or **2** on Au NPs to get the covalent EuNH₂@Au or ionic Eu@Au nanostructures.

The rationalization of the electronic structure of both EuNH₂@Au and Eu@Au nanostructures is fundamental to investigate the Au – Eu electron

interactions that are at the basis of the coupling of the Au plasmon resonance with the Eu(III) luminescence emission, and XPS represents the most suited tool to accomplish this task.[118-120]

Figure 3.3 shows the high-resolution XP spectra for both EuNH$_2$@Au and Eu@Au nanostructures, in the Au 4f binding energy region. The Au $4f_{7/2,5/2}$ spin-orbit components of Eu@Au nanostructures were observed at 83.7 and 87.3 eV (3.6 eV spin-orbit coupling), respectively, while these states lie at 83.3 and 87.0 eV (3.7 eV spin-orbit coupling), respectively, in the case of EuNH$_2$@Au nanostructures. In both cases, these binding energy values are consistent with Au^0 states.[169] The ~ 0.4 eV lower binding energy of the Au 4f levels of EuNH$_2$@Au with respect to binding energy values observed for Eu@Au nanostructures is in tune with the strong electron-donating capability of the -NH$_2$ group of the amino-phenanthroline ligand to the positively charged Au NPs surfaces.[57, 169]
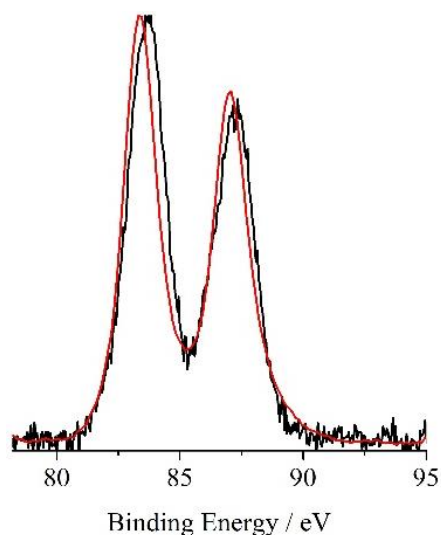
Figure 3.3. Al-Kα excited XPS of the centrifuged and washed with CH$_3$CN EuNH$_2$@Au (red line) and Eu@Au (black line) nanostructures in the Au 4f binding energy region. The two spectra have been normalized to the same intensity.

Figure 3.4 shows the high-resolution XP spectra of EuNH$_2$@Au and Eu@Au nanostructures in the Eu 3d binding energy region. The binding energies of the 3d$_{5/2,3/2}$ spin-orbit doublet for Eu@Au are at 1136.0 and 1165.9 eV, respectively (29.9 eV spin-orbit separation), while those for EuNH$_2$@Au are at 0.3 eV higher binding energy.[170, 171] These results, consistent with Eu(III) states, once more stress that, the transferring of electrons to the positively charged Au NPs surfaces, via the -NH$_2$ group the amino-phenanthroline ligand, makes poorer the Eu ions whose 3d level ionizations now are at 0.3 eV higher binding energy.
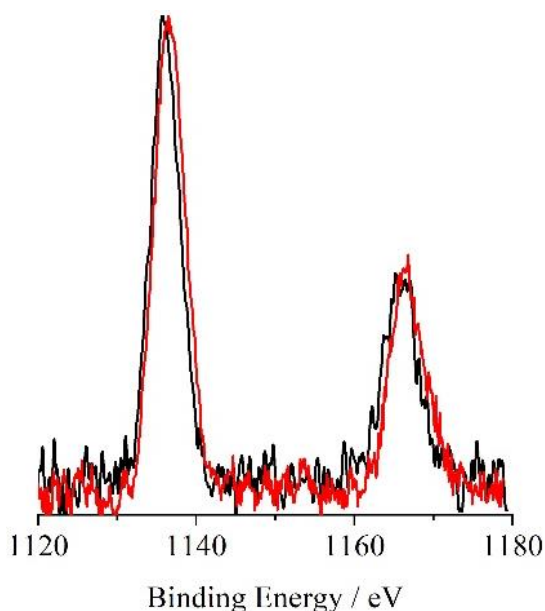
Figure 3.4. Al-Kα excited XPS of the centrifuged and washed with CH$_3$CN EuNH$_2$@Au (red line) and Eu@Au (black line) nanostructures in the Eu 3d binding energy region. The two spectra have been normalized to the same intensity.

Figure 3.5 shows the high-resolution XP spectra for Eu@Au and EuNH$_2$@Au in the N 1s binding energy region. The N 1s spectrum for Eu@Au shows only one band centered at 399.8 eV, due to the two nitrogen atoms of the phenanthroline ligand while, in the case of EuNH$_2$@Au, a careful fitting of the

experimental profile required two Gaussian components centred at 398.6 and 400.1 eV (1:2 intensity ratio). The component at 398.6 eV is assigned to the ionization of the nitrogen of the amine group (-NH$_2$), and that at 400.1 eV is due to the above-mentioned two nitrogen atoms of the phenanthroline ring that now lie at 0.3 eV higher binding energy with respect to the Eu@Au system, in tune with some electron depletion of the phenanthroline when its –NH$_2$ group donates to the positively charged surfaces of Au NPs.[172, 173]
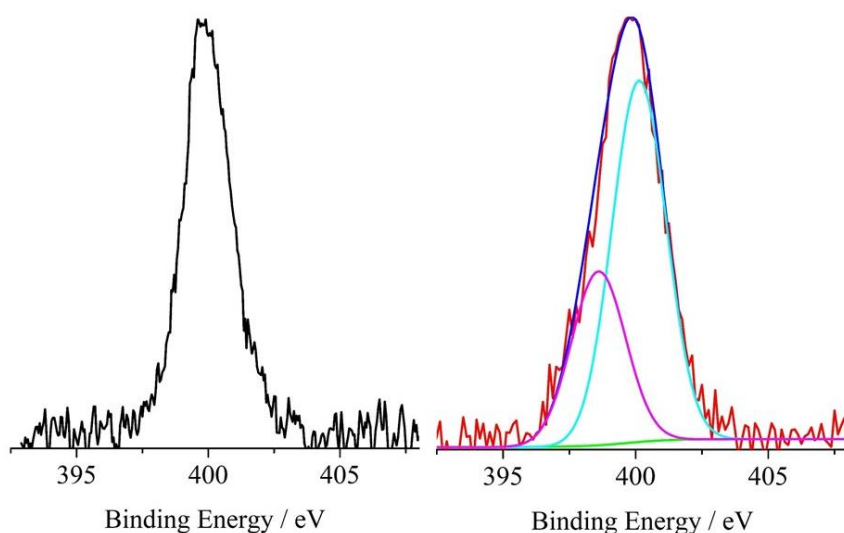
Figure 3.5. Al-Kα excited XPS of the centrifuged and washed with CH$_3$CN Eu@Au (black line) and EuNH$_2$@Au (red line) nanostructures in the N 1s binding energy region. For EuNH$_2$@Au, magenta and cyan lines represent the two Gaussian components at 398.6 and 400.1 eV, respectively; the green line refers to the background and the blue line, superimposed to the experimental profile refers to the sum of the Gaussian components. The two spectra have been normalized to the same intensity.

The XPS surface atomic concentration analyses indicated Eu/Au atomic ratios of 1.5 for EuNH$_2$@Au and of 0.1 for Eu@Au. This experimental evidence finds a counterpart in TEM and EELS data (vide infra) and suggests that the concentration of the overlay of **1** on the Au NPs is 15 times larger than that of **2**.

This result is not unexpected since **1** can covalently bind, and therefore organize on the Au NPs while **2** cannot do it. In this context, given the mean radius of the Au NPs ~ 5 nm, XPS should be able to probe almost a half of the Au NP thickness, being the probed depth about three times the electron inelastic mean free path of the Au 4f electrons (~ 16.3 Å for electron kinetic energy of ~ 1400 eV).[174]

DLS analysis of as-synthesized aqueous Au NPs solution (Figure 3.6) indicated a prevailing hydrodynamic radius (R_H) value of 5.6 nm and a radius distribution in the 2.7 - 10.6 nm range. These values include the citrate capping layer that covers the Au NPs. In fact, the TEM means radius resulted in 4.8 nm (vide infra).
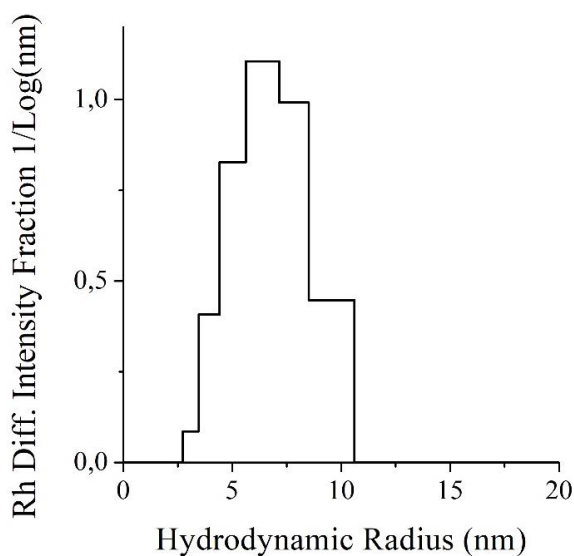
Figure 3.6. DLS of Au NPs in water solution.

The TEM microscopy of the Au NPs, EuNH$_2$@Au and Eu@Au nanostructures is reported in Figure 3.7. Single and highly dispersed Au nanoparticles, having a mean radius of about 5 nm (10 nm diameter), have been

obtained from the reduction of the tetrachloroauric acid with sodium citrate (Figure 3.7a). Furthermore, we observed that the Au NPs mainly show the (111) plane with a 2.36 Å interplanar distance (Figure 3.8). In presence of **1**, Au nanoparticles show a contour of ~ 1 nm around each Au NP (Figure 3.7b, c). In contrast, no contour at all is evident for Au nanoparticles in presence of **2** (Figure 3.7d). It is important to stress that **1** can covalently coordinate to the Au NPs while **2** cannot do it. Therefore, the texture surrounding the Au NPs represents complex **1** covalent assembled on gold nanoparticles.
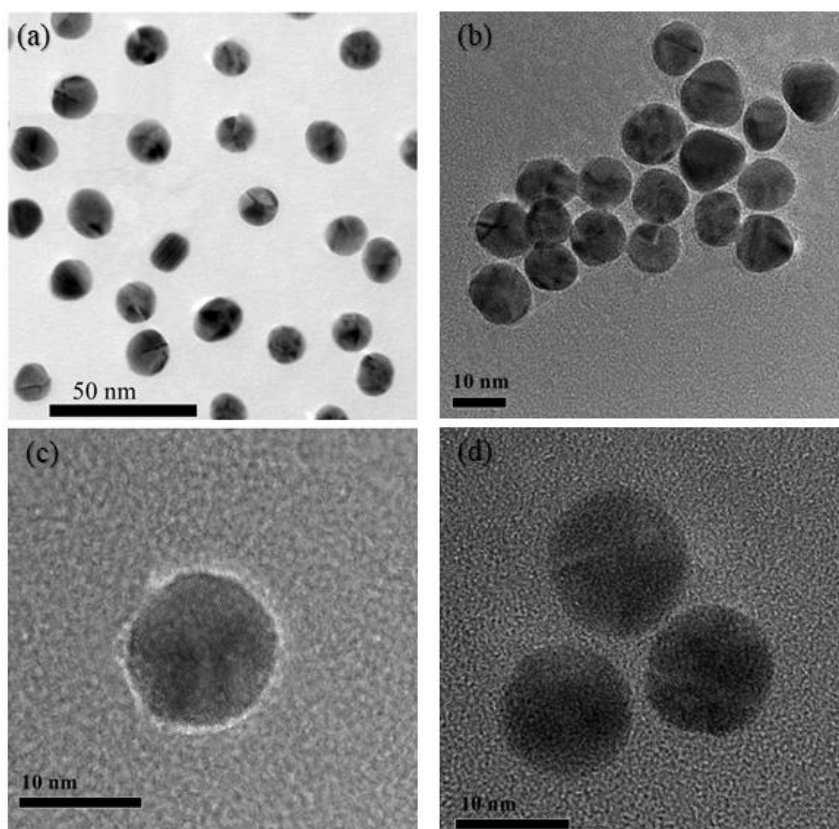
Figure 3.7. TEM images of: (a) Au nanoparticles obtained from the reduction of the tetrachloroauric acid with sodium citrate; (b) Au nanoparticles reacted with **1**; (c) expanded scale of Au nanoparticles reacted with **1** showing a contour of ~ 1 nm around each Au NP; (d) Au nanoparticles reacted with **2**.
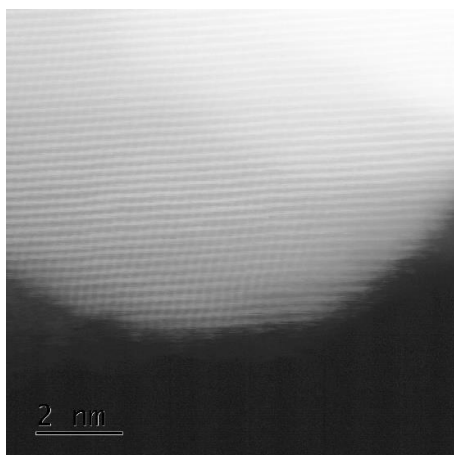
Figure 3.8. HAADF-STEM at atomic resolution showing a representative Au NP highly oriented towards the (111) plane with an interplanar distance of 2.36 Å.

We analyzed the chemical composition of these assemblies by Electron energy loss spectroscopy (EELS) and the results are indicative of Au nanoparticles surrounded by a thin layer of an Eu-complex, in the case of **1** (Figure 3.9), while **2** on Au NPs is negligible (Figure 3.10).
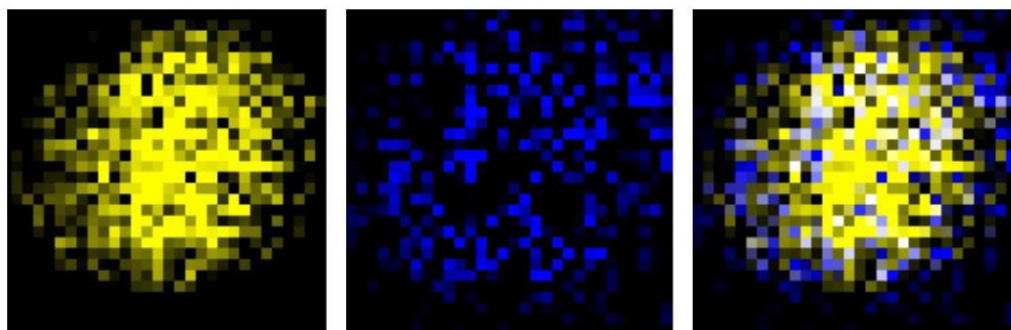
Figure 3.9. EELS of Au nanoparticles reacted with **1** (EuNH$_2$@Au) showing: Au (left), Eu (middle) and both Au-Eu (right) for a representative Au NP.
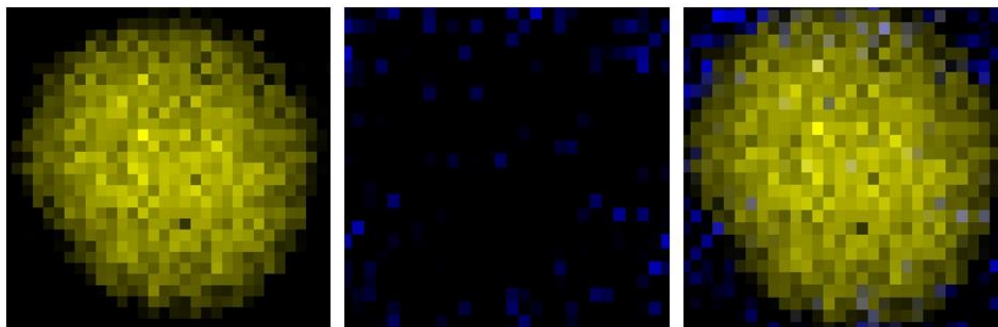
Figure 3.10. EELS of Au nanoparticles reacted with **2** (Eu@Au) showing: Au (left), Eu (middle) and both Au-Eu (right) for a representative Au NP.

It is well known that Au NPs can either be luminescent or plasmonic and this restricts many possible applications as an optical material. Therefore, the goal we would achieve with this functional architecture is to maintain the surface plasmon resonance, typical of Au nanoparticles, as well as the luminescence signal, coming from the Eu complex. Figures 3.11 and 3.12 show the UV-visible spectra of $EuNH_2$@Au and Eu@Au, upon the additions of the Au NPs solution to solutions of **1** and **2**. We continued the addition of the Au NPs solution until detected zero-emission for one of the two investigated systems (vide infra). The final CH_3CN/H_2O 99.375:0.625 v/v solution is 1.23×10^{-9} M in Au NPs and 1.66×10^{-5} M in **1** or **2**. For $EuNH_2$@Au, there is evidence of a strong band at 340.4 nm and of a broad envelope extending from 225 to 300 nm with peaks at 232.2, 252.8 and 280.8 nm, all of them attributed to the π–π* transitions of the large π-conjugated system.[170, 175] The Inset shows the 400-900 nm expanded scale and highlights the intensity increase of the surface plasmon resonance due to the Au NPs, whose position, now at 522.2 nm, is slightly affected by the Eu-complex coordination (see also the UV-vis of the as-synthesized Au NPs in Figure 2.13). The main band of the Eu complex show an evident and monotonic intensity

increase upon the addition of Au NPs, thus indicating a gradually increase of the extinction coefficient of EuNH$_2$@Au from 68700 (that of **1**) to 83600 M^{-1}·cm^{-1}.

Figure 3.11. Selected UV-vis spectra of 1.5 mL of **1** 1.77×10^{-5} M (2.65×10^{-8} mol) CH$_3$CN solution (black line), and upon the addition of 10 (red line), 20 (green line), 30 (blue line), 40 (cyan line), 50 (magenta line), 60 (yellow line), 70 (dark yellow line), 80 (navy line), 90 (purple line) and 100 (orange line) µL of a 1.97×10^{-8} M (1.97×10^{-12} mol) Au NPs (CH$_3$CN/H$_2$O 9:1 v/v) solution (final total volume 1.6 mL CH$_3$CN/H$_2$O 99.375:0.625 v/v). The final concentrations of **1** and Au NPs are 1.66×10^{-5} M (2.65×10^{-8} mol) and 1.23×10^{-9} M (1.97×10^{-12} mol), respectively. All spectra have been corrected for the volume variation. Inset: expanded scale of the 400-900 nm wavelength range.

Figure 3.12 shows the UV-visible spectra of Eu@Au upon the additions of the Au NPs solution. In analogy with the previous case, we noted a strong band at 340.1 nm and, at variance, now we did not observe any broad envelope but strong peaks at 228.3 and 261.0 nm, being the last one representative of the previous 252.8 and 280.8 nm small peaks of EuNH$_2$@Au. Also, in this case, the Inset shows the intensity increase of the surface plasmon resonance, at 521.6 nm,

due to the Au NPs, whose highest intensity is ~ 20% less intense than that observed for $EuNH_2@Au$.

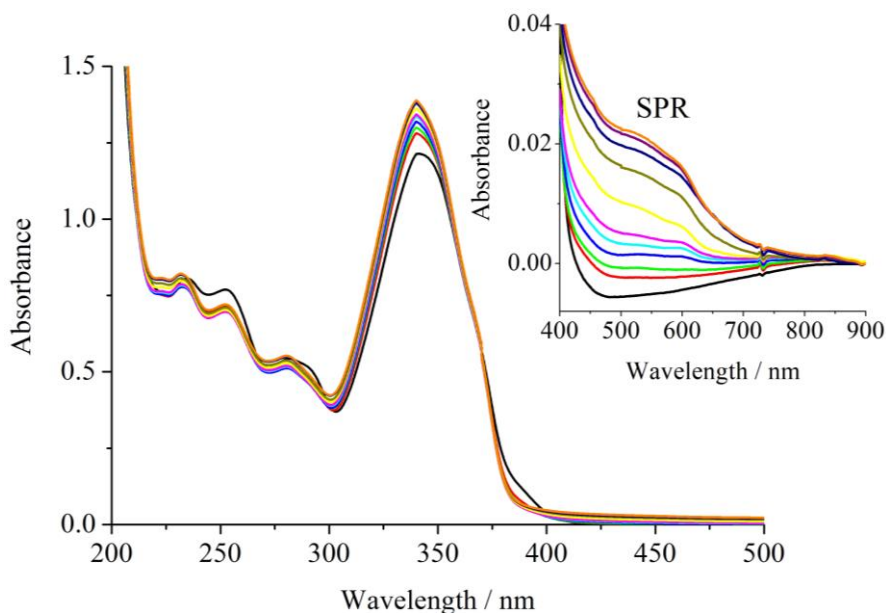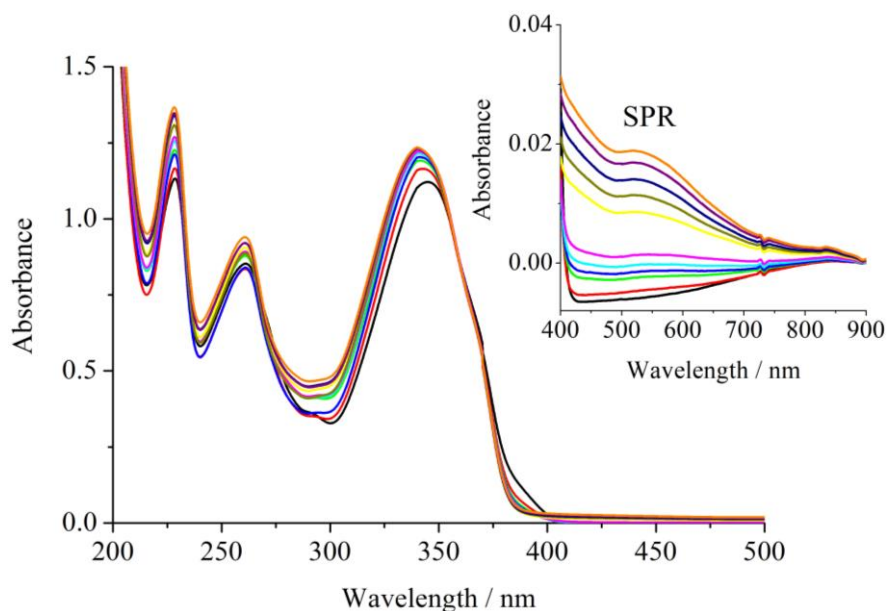**Figure 3.12**. Selected UV-vis spectra of 1.5 mL of **2** 1.77×10^{-5} M (2.65×10^{-8} mol) CH_3CN solution (black line), and upon the addition of 10 (red line), 20 (green line), 30 (blue line), 40 (cyan line), 50 (magenta line), 60 (yellow line), 70 (dark yellow line), 80 (navy line), 90 (purple line) and 100 (orange line) µL of a 1.97×10^{-8} M (1.97×10^{-12} mol) Au NPs (CH_3CN/H_2O 9:1 v/v) solution (final total volume 1.6 mL CH_3CN/H_2O 99.375:0.625 v/v). The final concentrations of **2** and Au NPs are 1.66×10^{-5} M (2.65×10^{-8} mol) and 1.23×10^{-9} M (1.97×10^{-12} mol), respectively. All spectra have been corrected for the volume variation. Inset: expanded scale of the 400-900 nm wavelength range.

Figure 3.13 shows the emission spectra for solutions of **1** and **2** bare complexes, whose intensities at 612 nm were normalized to 100 to make some important relative comparisons. The band at 488 nm was observed only for **1** and is due to the presence of the amino group on the phenanthroline ligand. The absence of this amino group in **2** causes the total absence of this band in its emission spectrum. The transition band $^5D_0 \rightarrow {}^7F_2$ at 612.0 nm indicates that

both Eu^{3+} complexes efficiently emit red light.[176] In this context, filled $5s^2$ and $5p^6$ levels shield 4f orbitals from ligand field effects so that 4f levels in lanthanide compounds have generally been considered essentially atomic in nature and simple spectators with respect to the chemical bond.[177-179] This certainly holds for ionic oxides and halogenated lanthanides.[177-179] In contrast, quantum mechanical calculation combined with photoelectron spectroscopic studies highlighted some lanthanide-ligand covalency in discrete organometallic molecules.[179-182] In addition, because of the effective intramolecular energy transfer from the coordinated ligands to the luminescent central lanthanide ion, emission of Eu(III) results to be strongly influenced by the metal environment.[183] In fact, Eu(III) has five narrow emission bands corresponding to the $^5D_0 \rightarrow {^7F_J}$ transitions, where $J = 0, 1, 2, 3, 4, 5, 6$ and the cross-section for the $^5D_0$ (lowest excited state) $\rightarrow {^7F_{0-6}}$ (ground states) transitions depends on the Eu site symmetry.[183] Eu(III) in sites with inversion symmetry shows the magnetic-dipole $^5D_0 \rightarrow {^7F_1}$ transition at ~590 nm whilst, Eu(III) in sites with no inversion symmetry undergoes the electric-dipole $^5D_0 \rightarrow {^7F_2}$ strong transition with emissions in the 610-620 nm range.[183] In practice, the various states arising from f^n configurations are split by external fields only to a small extent (~100 cm^{-1}).[180, 183] Therefore, even though with different intensities, both electric- and magnetic-dipole transitions are evident in emission spectra of Eu(III)-containing materials.
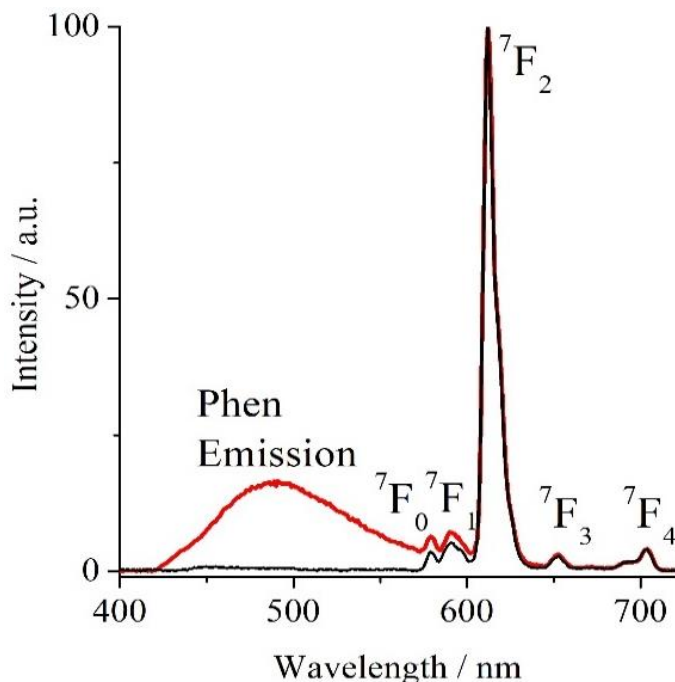
Figure 3.13. Relative emission spectra of **1** (red line) and **2** (black line) CH$_3$CN 1.77 $\times$ 10^{-5} M solution; λ_{exc} = 380 nm.

Figure 3.14 shows the variation of the intensity emission for both **1** and **2**, measured at 612 nm, upon the addition of Au NPs to get EuNH$_2$@Au and Eu@Au and Figures 3.15-3.16 show these emission spectra.

A strong plasmonic quenching of this Eu(III) emission intensity is evident, as already observed in many cases where Au NPs are mixed with fluorescent molecules.[152-160] In contrast, the emission centred at 488 nm (Figure 3.13), due to the 5-amino-1,10-phenanthroline ligand, gradually increased up to 36% of its initial intensity and moved to 497 nm. Worthy of note, (vide supra), we did not observe any concentration-dependent quenching of absorption but, in contrast, for these systems we noted an increase of the Eu-complex ε value. The binding of Au NPs with luminescent dyes could lead to coupling of plasmonic mode with

molecular mode but, in the present case, no peaking splitting was observed.[128-130] As mentioned above, we continued the addition of the Au NPs solution until detected zero-emission at 612 nm for one of the investigated systems and observed that, when Eu@Au was not emitting any more, in contrast, the emission of $EuNH_2$@Au reached a plateau with some residual, but significant intensity. At this point the emission band centered at 488 nm (now at 497 nm) for $EuNH_2$@ Au has not undergone any quenching, indeed it is now 136% more intense than the starting band, while the emission at 612 nm is now only 6% of its initial intensity.

Such an increase in the luminescence of the emission at 497 nm may be explained by the fact that the electronic system of metallic nanostructured surfaces interacts with the photonic emission from fluorophores thus resulting in signal enhancement and this phenomenon is called surface plasmon coupled emission.[161, 184]

Plasmonic near-field enhancement is a phenomenon that involves competition among emission or excitation enhancement and quenching. Both phenomena largely depend upon the distance between the metal surface and the fluorophores. Therefore, we modelled the ground state Eu(III) complex **1** anchoring geometry using the Sparkle/PM6 model implemented in the MOPAC2012 semi-empirical software.[185] The MOPAC keywords used in the semiempirical Sparkle/PM6 calculations were: PRECISE, GEO-OK, GNORM = 0.25, SCFCRT =1.D-10 and XYZ.

The resulting pseudo-tetrahedral angle of the lone pair of the amino group with respect to the hydrogen atoms is 111° instead of 109°. These results indicate that the Eu-complex molecules are tilted by 69° with respect to the normal to the

Au NPs surface. The distance between the Eu(III) ion and the -NH$_2$ lone pair is 10.2 Å and the separation distance between the Eu(III) and the Au NPs surface is 9.5 Å.

It has already been reported that AuNPs decrease the transition probability for radiative transitions and effectively quench the fluorescence of dye molecules even for dye-Au NP separation distances as long as 22 nm.[186] Moreover, the strong fluorescence quenching, caused by energy transfer from the excited dye molecules to the AuNP, occurs with efficiencies as high as 95%. Therefore, the energy transfer to the metal surface is the more dominant quenching mechanism and this may explain why in solution, molecules of **1** and **2** suffer a strong emission quenching.[134-136]
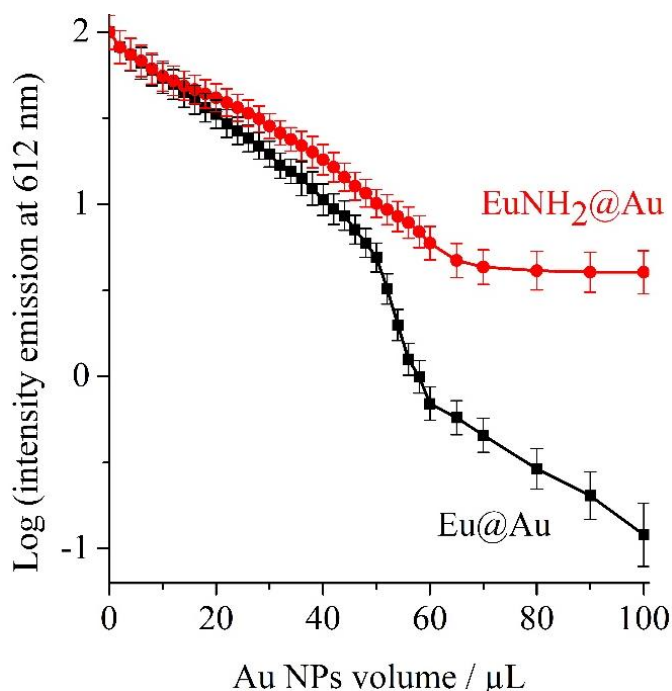
Figure 3.14. Relative variation of the intensity emission measured at 612 nm, for both **1** and **2** upon the addition of the Au NPs 1.97×10^{-8} M CH$_3$CN/H$_2$O 9:1 v/v solution (2 ÷ 100 μL), to get EuNH$_2$@Au and Eu@Au, respectively.
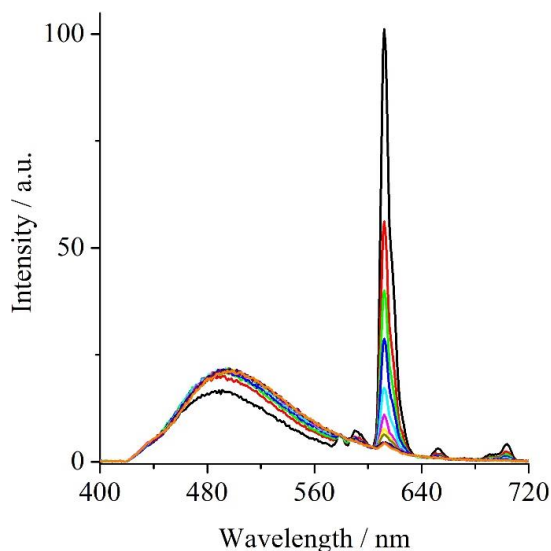
Figure 3.15. Selected emission spectra of 1.5 mL of **1** 1.77×10^{-5} M (2.65×10^{-8} mol) CH_3CN solution (black line), and upon the addition of 10 (red line), 20 (green line), 30 (blue line), 40 (cyan line), 50 (magenta line), 60 (yellow line), 70 (dark yellow line), 80 (navy line), 90 (purple line) and 100 (orange line) µL of a 1.97×10^{-8} M (1.97×10^{-12} mol) Au NPs (CH_3CN/H_2O 9:1 v/v) solution (final total volume 1.6 mL CH_3CN/H_2O 99.375:0.625 v/v). The final concentrations of **1** and Au NPs are 1.66×10^{-5} M (2.65×10^{-8} mol) and 1.23×10^{-9} M (1.97×10^{-12} mol), respectively. All spectra have been corrected for the volume variation.

Figure 3.16. Selected emission spectra of 1.5 mL of **2** 1.77×10^{-5} M (2.65×10^{-8} mol) CH_3CN solution (black line), and upon the addition of 10 (red line), 20 (green line), 30

(blue line), 40 (cyan line), 50 (magenta line), 60 (yellow line), 70 (dark yellow line), 80 (navy line), 90 (purple line) and 100 (orange line) µL of a 1.97×10^{-8} M (1.97×10^{-12} mol) Au NPs (CH_3CN/H_2O 9:1 v/v) solution (final total volume 1.6 mL CH_3CN/H_2O 99.375:0.625 v/v). The final concentrations of **2** and Au NPs are 1.66×10^{-5} M (2.65×10^{-8} mol) and 1.23×10^{-9} M (1.97×10^{-12} mol), respectively. All spectra have been corrected for the volume variation.

We centrifuged, washed until no UV-signal of any Eu(III) complex was observed in the supernatant, re-dissolved by sonication the $EuNH_2@Au$ in 1.6 mL of CH_3CN and measured its UV-vis spectrum (Figure 3.17).

Figure 3.17. UV-vis spectrum of the $EuNH_2@Au$ 7.87×10^{-10} M Au NPs solution, after centrifugation, washing and re-dissolution by sonication in CH_3CN.

This spectrum is dominated by the surface plasmon resonance of the Au NPs at 529.4 nm. Moreover, the shoulders at 232.6 and 252.8 nm and the bands at 290.0 and 340.4 nm are close to those already observed for the solution of $EuNH_2@Au$ shown in Figure 3.11 and indicate that this residual absorbance was granted by the Eu(III) monolayer covalently bound to the Au NPs. The surface

coverage of the Au NPs with europium molecules was calculated using the Beer−Lambert law, (A = εcl, where A is the absorbance, l is the path of the quartz cell (1 cm), ε and c are the extinction coefficient and the concentration of the EuNH$_2$ molecules covalently bound to the Au NPs surface, respectively). The intensity of the Au NPs SPR band after centrifugation and sonication is 64% of that observed in Figure 3.11. Then, we can safely assume that the concentration of Au NPs is now 64% of the starting one (1.23 × 10^{-9} × 0.64 = 7.87 × 10^{-10} M, 1.26 × 10^{-12} mol). By taking into account the ε value of 83600 M^{-1} cm^{-1} for the band at 340.4 nm of EuNH$_2$ in CH$_3$CN (Abs = 0.012), the calculated number of Eu molecules covalently bound to the centrifuged Au NPs is 1.38 × 10^{14}. This means that 181 molecules of **1** are bound to each Au NP whose surface area is 314 nm^2 (area of a sphere of 5 nm radius) thus giving a footprint of 1.73 nm^2 for each Eu molecule. Both these values are highly reasonable, in tune with many already reported data for similar systems, and state the presence of a monolayer of **1** around each Au NP with a full surface coverage.[155, 171] In addition, this footprint is also in agreement with the Eu molecule's cross-sectional area of 201 Å^2 previously estimated with the Gaussian 03 code.[170] Also the UV-vis spectrum of Eu@Au, after centrifugation, washing and re-dissolution by sonication in CH$_3$CN is dominated by the Au plasmon resonance band at 522.0 nm but it does not show any relevant Eu absorbance bands, in tune with the overall previously discussed results (Figure 3.18).
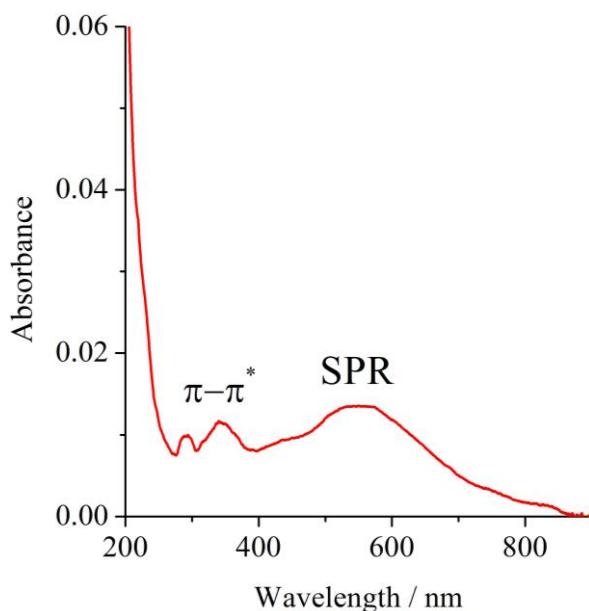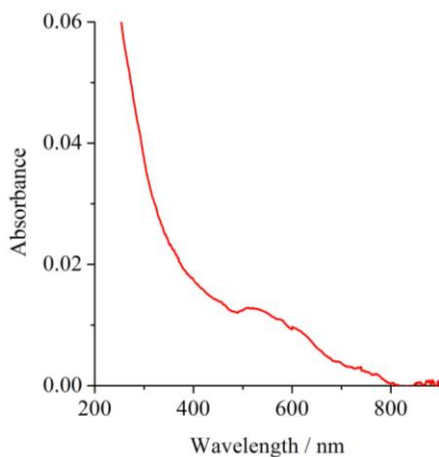
Figure 3.18. UV-vis spectrum of the Eu@Au 7.87×10^{-10} M Au NPs solution, after centrifugation, washing and re-dissolution by sonication in CH_3CN.

Then we measured also the emission spectrum of these centrifuged, washed and re-dissolved $EuNH_2$@Au 7.87×10^{-10} M in CH_3CN (Figure 3.19) and observed residual emissions at 488 and 612 nm granted by the Eu(III) monolayer covalently bound to the Au NPs.
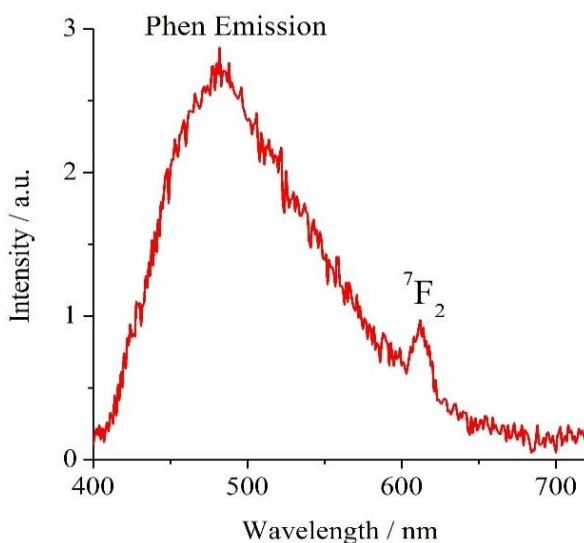
Figure 3.19. Emission spectrum of the $EuNH_2$@Au 7.87×10^{-10} M Au NPs solution (1.65×10^{-7} M in Eu(III)), after centrifugation, washing and re-dissolution by sonication in CH_3CN, showing residual emissions at 488 and 612 nm; $\lambda_{exc} = 380$ nm.

The intensity of the remaining emission due to the Eu(III) at 612 nm is 1 % of the starting intensity. If this emission is due to 1% of the starting Eu-complex molecules (corresponding to 2.65×10^{-10} mol $= 1.60 \times 10^{14}$ Eu-complex molecules), this value is very close to that obtained by UV-vis data (1.38×10^{14}) and further confirms the presence of a monolayer of Eu-complex molecules on each Au NPs. As a result, we synthesized $EuNH_2@Au$ nanostructures that remained plasmonic and relatively emissive and this means that the strongly different assembly modes of **1** and **2** on Au NPs govern this property. In this context, TEM results indicated that, thanks to its amino group, **1** surrounds Au NPs and this, in turn, grants a better optical performance to the final nanostructures that remain both plasmonic and luminescent.[57] We suppose that this is the case of covalent-assembly of **1** through bonds on Au NPs. Also, XPS demonstrated that the number of the Eu-complex molecules bound to Au NPs is 15 times larger in case of **1**, with respect to that of **2**. Therefore, the through-bond interaction by the $-NH_2$ group and the Au NPs causes a change in the electronic structure of **1** that disfavors some energy transfer to the Au metal surface and assures some remaining Eu luminescence. In contrast, **2** is only physisorbed, mainly through weak interactions, on Au NP surfaces, and the through-space Eu(III) complex – Au NPs interaction causes a complete quenching of the Eu(III) emission.

Conclusions

In this chapter, it was shown the synthesis of Au nanoparticles decorated with two slightly different Eu(III) complexes. Both functional architectures exhibit a surface plasmon, due to the Au nanoparticles but only EuNH$_2$@Au maintains, in addition, some luminescence signal, thus giving a new optical material having unique characteristics. The difference between the two nanostructures is represented by the possibility of **1** to covalent assembly on the Au NPs and, therefore, interact through bond with them. Apparently, the covalent N-Au interaction in EuNH$_2$@Au limits some energy transfer to the metal surface that would result in a total quenching mechanism. In contrast, **2** can only interact through space with Au NPs. This different interaction preserves some emission intensity in the EuNH$_2$@Au while a total emission quenching was observed for Eu@Au. In summary, from our study, it emerges that the covalent dye-Au NP interaction hinders some Eu(III) emission quenching mechanisms. In addition, we observed an increase in luminescence of the emission at 497 nm of the amino-phenanthroline due to surface plasmon coupled emission. Therefore, the present EuNH$_2$@Au nanostructures can be useful for all applications requiring plasmonic emitters under atmospheric conditions since our system is not reactive to air nor to water and does not need to be stored in vacuum or inert gas.

.

Chapter 4

Core–Shell Plasmonic Nanostructures for Environmental Applications

In the previous chapters of this thesis, it has been shown that the properties of the synthesized hybrid nanostructures are strongly dependent on the electronic structure of the emissive molecules bound to plasmonic Au nanoparticles.

Now we want to investigate some semiconductor photocatalysts that are a class of emerging nanomaterials that show many applications comprising the degradation of toxic pollutants in wastewater. When the photocatalytic semiconductor is exposed to photons having energy equal to or higher than its bandgap, the generated electron−hole pairs can react with atmospheric oxygen and produce highly reactive oxygen species suitable to promote oxidation processes for the degradation of many organic compounds.

However, the major disadvantage of some of these materials is due to the wide-bandgap that makes them promising for ultraviolet (UV) detection but less efficient for sun-driven applications. So, one way to overcome this limitation is the synthesis of hybrid metal-semiconductor photocatalysts based on inorganic semiconductors, especially metal oxides, and noble metal plasmonic nanoparticles. In particular, the core-shell structure, in which a very thin shell

layer of metal oxide surrounds the noble metal nanoparticle core, has significant potential application as a photocatalyst because the presence of noble metal improves solar light-harvesting capacity, enhance the efficiency of the interfacial charge separation process and as well as reduce the recombination possibilities of hole and electron pair which initiated the photocatalytic reaction.

Noble metal nanoparticles such as Ag, Au, Pd and Pt in ZnO materials increase the lifetime of e^-/h^+ pairs due to their plasmon resonance produced by the collective oscillations of surface electrons (Figure 4.1).
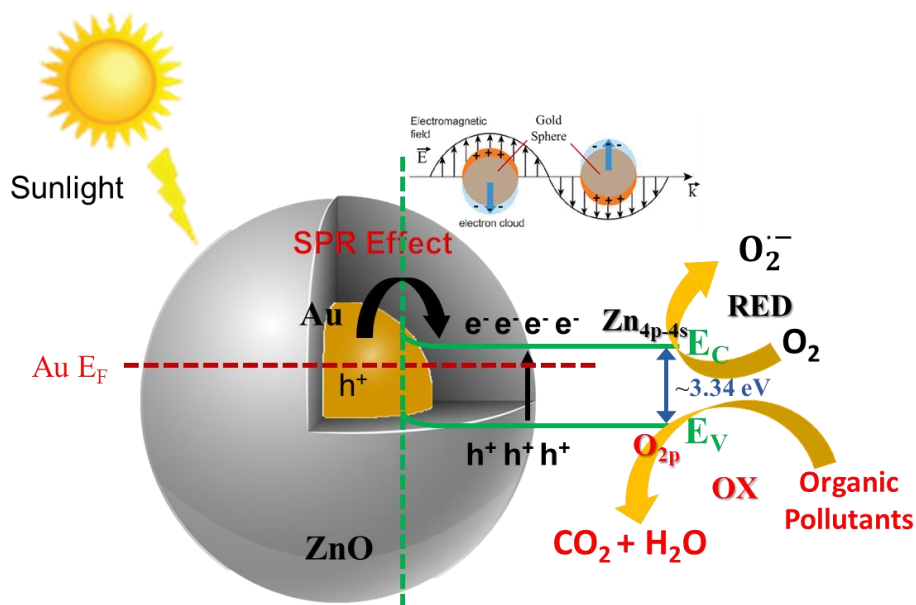
Figure 4.1. SPR effect on Au_ZnO core−shell nanoparticles.

In this context, Au_ZnO core−shell nanoparticles are promising for applications in the fields of photocatalysis because of the coupling of surface plasmon resonance of Au NPs with the exciton emission in the ZnO shells represents the best-suited way to boost photodetection.

4.1 Sun Light Photocatalytic activity of Au_ZnO Core–Shell Nanoparticles

The need of clean water is one of the main urgent problems of humanity. Typical wastewater treatments (filtration, chlorination, desalination, reverse osmosis, etc.) suffer from severe limitations because of the ineffective decontamination and/or elevate related costs. In this context, the peculiar properties of some new nanostructures may overcome these issues and promote unconventional water purification methods.

From this perspective, the ZnO-based photocatalyst has attracted great attention because of the low cost of ZnO and its excellent stability, abundance, and photoactivity. The main disadvantage of ZnO is the wide-bandgap that makes it promising for UV detection but less efficient for visible sun-driven applications. ZnO is a semiconductor with a wide-bandgap of about 3.37 eV, a large free exciton binding energy of 60 meV and a high electron mobility of ∼ 400 cm^2 V^{-1} s^{-1}.[187, 188] It shows a great surface area/volume ratio, quantum confinement effect and is an exceptional electronic and photonic material that finds applications in dye-sensitized solar cells, field emission devices, sensors, catalysis, light-emitting diodes etc.[189]

However, noble metal–ZnO composite nanostructures may overcome this problem as noble metal nanoparticles absorb visible light and generate localized surface plasmon resonances, useful to enhance photodetection of visible–light.[190] Therefore, the conjugation of gold NPs and the wide-bandgap ZnO

semiconductor is one of the most suitable ways to enhance ultraviolet–visible (UV–vis) photodetection.[169, 191, 192]

In this context, there have been many reports concerning the photocatalytic activity of Au on ZnO materials, useful in many different technological fields.[193-201] Conversely, a few studies of Au_ZnO having a core-shell structure (ZnO shell on Au NPs core) have been reported. Between them, the optical properties of ZnO shell grown on Ag and Au nanoparticle cores by a solution method, have been investigated.[202] It was found that both the ZnO/Ag and ZnO/Au particles exhibit strongly enhanced near-band-edge UV exciton emission from the ZnO shells of coupling with surface plasmon resonance of the metal nanoparticles. These observations suggested the suitability of metal NPs for improving optical detection.

In another study, Au/ZnO core–shell NPs with different shell thicknesses were obtained by chemically depositing zinc oxide on gold NPs surfaces.[203] A significant effect on the photoluminescence intensity and shortening of the decay time of the Rhodamine 6G dye in presence of Au/ZnO core–shell NPs was observed. The current–voltage curve of hybrid Au/ZnO exhibited a rectifying nature and represented the n-type Schottky diode characteristics with a typical turn-on voltage between 0.6 and 1.3 V. It was also found that the rectifying ratio increases with decreasing the thickness of the ZnO shell, whereas the electrical transport through the core–shell was similar to what was observed for pure ZnO sample NPs. Also, the nature of the O vacancy in graphitic-like ZnO bilayer films supported on Cu, Ag, and Au(111) surfaces was studied by quantum mechanical calculations.[204] Furthermore, hybrid semiconductor plasmonic nanostructures of zinc oxide on gold NPs were synthesized by direct addition of

ZnO quantum dots to aqueous dispersions of gold nanoparticles of different sizes and so forth.[205]

Recently, we obtained some core–shell Au_ZnO NPs by reacting zinc citrate $Zn_3(C_6H_5O_7)_2 \cdot 2H_2O$ and $HAuCl_4 \cdot 3H_2O$ in a one-pot synthesis in which the [Zinc Citrate]$^-$ complex (Figure 4.2) acted as the ZnO precursor, a reducing agent for Au^{3+}, and a capping anion for the obtained Au NPs (Figure 4.3).[169] Transmission electron microscopy (TEM) and energy dispersive X-ray (EDX) measurements provided evidence of Au(111) NPs with a mean radius of about 5 nm, surrounded by ~2 nm layer of [Zinc Citrate]$^-$ that evolved in $Au\_Zn(OH)_2$ and then in Au_ZnO.

Therefore, in the present investigation, we report on the photocatalytic activity of the above-mentioned Au_ZnO core–shell nanoparticles, prepared by a one-pot synthesis, toward a standard methylene blue (MB) solution, according to ISO 10678:2010. Worthy of note, sun light was used as the irradiation source, and observing a fast and efficient MB decomposition. Finally, we accurately calculated the number of adsorbed photons, the reaction rate, and the quantum efficiency.
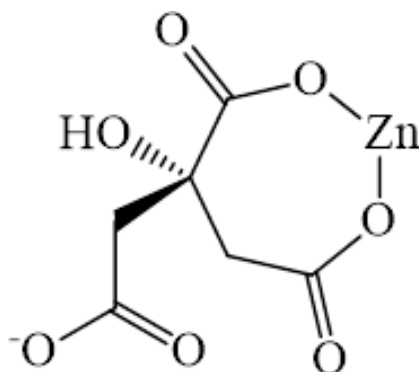
Figure 4.2. Structure of the [Zinc Citrate]$^-$ complex.
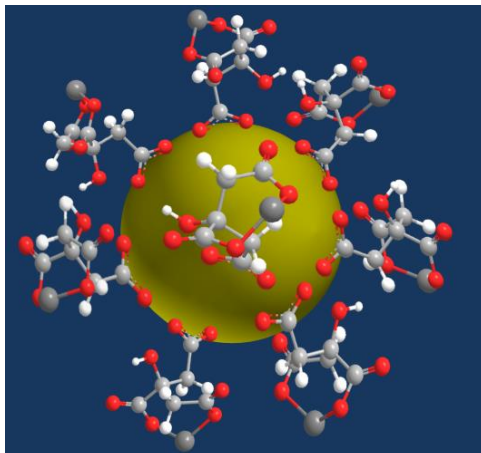
Figure 4.3. Schematic draw of the Au NPs capped with the ZnCit⁻ anion.

4.2 One-Pot Synthesis of Au_ZnO Core–Shell NPs

The synthesis of Au NPs capped with ZnO nanoparticles was performed as previously reported.[169] In particular, an appropriate quantity of zinc citrate $Zn_3(C_6H_5O_7)_2 \cdot 2H_2O$ [hereafter $Zn_3(Cit)_2$] was introduced into a three-necked flask and stored in the refrigerator at 5°C. After 24 h the mixture was totally clear (zinc citrate is more soluble in cold than warm water, because it has an inverse solubility [2.60 g/L]) and the measured pH was 6.50. Then, we brought this solution on a heating plate and slowly added aliquots of a $HAuCl_4 \cdot 3H_2O$ solution to have a final 1.5% Au^{3+} concentration in Zn^{2+}. Before, the solution was left to cool thus leaving Au nanoparticles, thanks to the reducing action of the [ZnCit]⁻ complex. [169] Afterward, we dropwise added conc. NH_3 to obtain a white gel of Au_Zn(OH)₂ at pH = 8.9. Finally, the overall gel was purified by dialysis against deionized water, left to evaporate up to a few mL and dried at 130°C. A similar synthetic procedure was used to synthesise ZnO, without any addition of $HAuCl_4 \cdot 3H_2O$. In the present study, we are dealing with ZnO and

75

Au_ZnO dried at 130°C, since the photocatalytic behaviour of the materials obtained at this temperature is better than that observed for the same materials sintered at higher temperatures (up to 1000°C). At this temperature (130°C) we observed the presence of some hydrated ZnO (vide infra) but, for convenience, we will refer to ZnO throughout the paper. The synthetic reaction scheme is represented in Scheme 4.1.
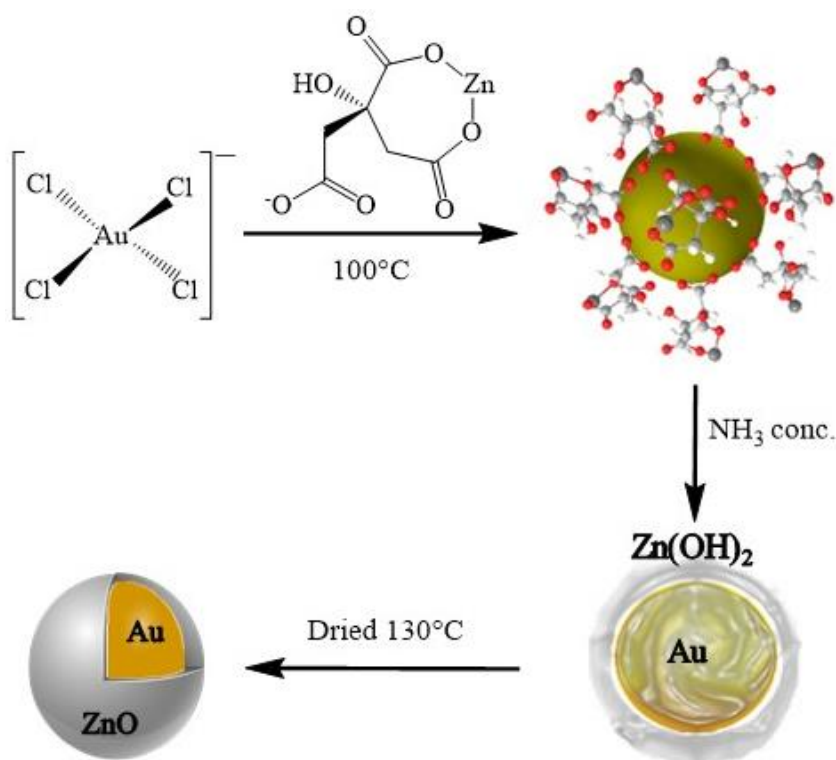
Scheme 4.1. Reaction pathway for the synthesis of the core-shell Au_ZnO nanostructures.

4.3 Characterization of Au_ZnO Core–Shell NPs

The electronic study of the Au_ZnO nanostructure, fundamental to investigate the Au-ZnO electron interactions, which are the basis of the

coupling of the plasmon Au resonance with the ZnO exciton emission, was carried out by XPS.[118-120]

Figure 4.4 shows the XP spectrum of Au_ZnO in the Au 4f–Zn 3p binding energy region. A careful deconvolution of this experimental profile reveals that the Au $4f_{7/2,5/2}$ spin–orbit components lie at 83.8 and 87.6 eV (3.8 eV spin–orbit coupling), thus indicating the presence of Au^0 states, usually expected at 84.0 eV $(4f_{7/2})$.[83] The Zn 3p levels, clearly resolved in their spin–orbit components, lie at 88.9 and 91.9 eV, respectively with a 3.0 eV spin–orbit coupling. These 3p levels are a couple of tens of eV at higher binding energy with respect to those previously reported for ZnO.[206]
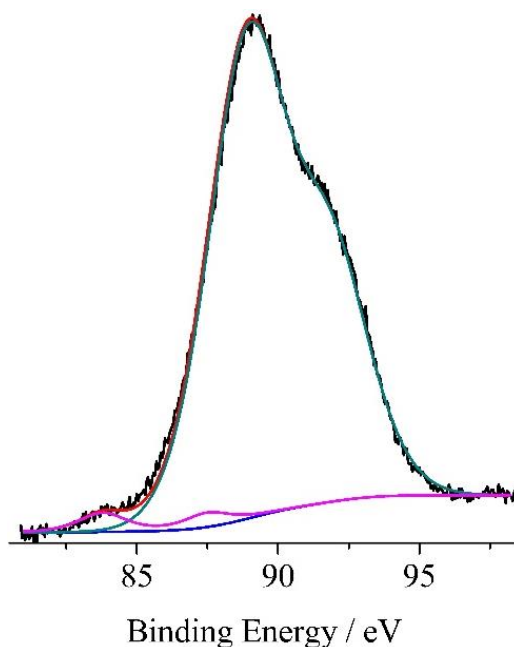
Figure 4.4. Al-Kα excited XPS of the Au_ZnO, dried at 130°C, in the Au 4f – Zn 3p binding energy region. The black line refers to the experimental profile. The blue line represents the background; the magenta line refers to the Au 4f spin–orbit components; the green line refers to the Zn 3p spin–orbit components; the red line superimposed on the experimental profile refers to the sum of the Gaussian components.

Figure 4.5 shows the XPS of Au_ZnO in the Zn 2p binding energy region. The $2p_{3/2,1/2}$ spin−orbit components have been observed at 1023.7 and 1046.7 eV, respectively. These values are about 2 eV at higher energy with respect to typical values observed for pure ZnO materials,[207-209] but almost identical to those previously reported for some Au−ZnO architectures.[210] This observation strongly confirms the electronic communication between ZnO and Au in a way that ZnO electrons are supplied to Au.
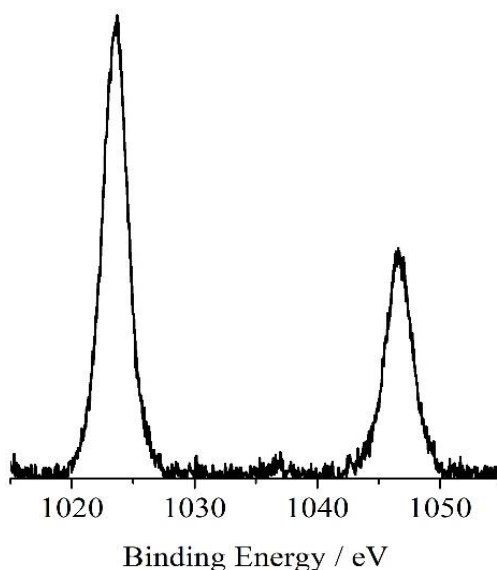
Figure 4.5. Al-Kα excited XPS of the Au_ZnO, dried at 130°C, in the Zn 2p binding energy region.

Finally, the XPS atomic concentration analysis revealed an Au/Zn percentage of 0.6, roughly corresponding to half of the nominal Au concentration. This result is acceptable since XPS probes only the surface of the Au_ZnO material whose composition is 98.5 % in Zn.

The crystal structure of both ZnO and core–shell Au_ZnO powders was investigated by X-ray Diffraction (XRD) measurements. The obtained

patterns, shown in Figure 4.6, have multiple contributions that have been attributed to different phases. The gold nanoparticles provide clear and intense 111, 200 and 220 reflections of the face-centred cubic lattice with $Fm\overline{3}m$ symmetry (PDF 00-04-0784). Besides the gold contributions, the two patterns share common phases mostly ascribed to orthorhombic (PDF 00-020-1435) and tetragonal (PDF-00-38-0356) sweetite structures with stoichiometry $Zn(OH)_2$. The additional reflections 100, 002 and 102 (space group $P6_3mc$, COD ID 00-101-1258) and 101 and 110 (space group $P6_3mc$, PDF 01-075-1533) belong to the ZnO hexagonal zincite structure.
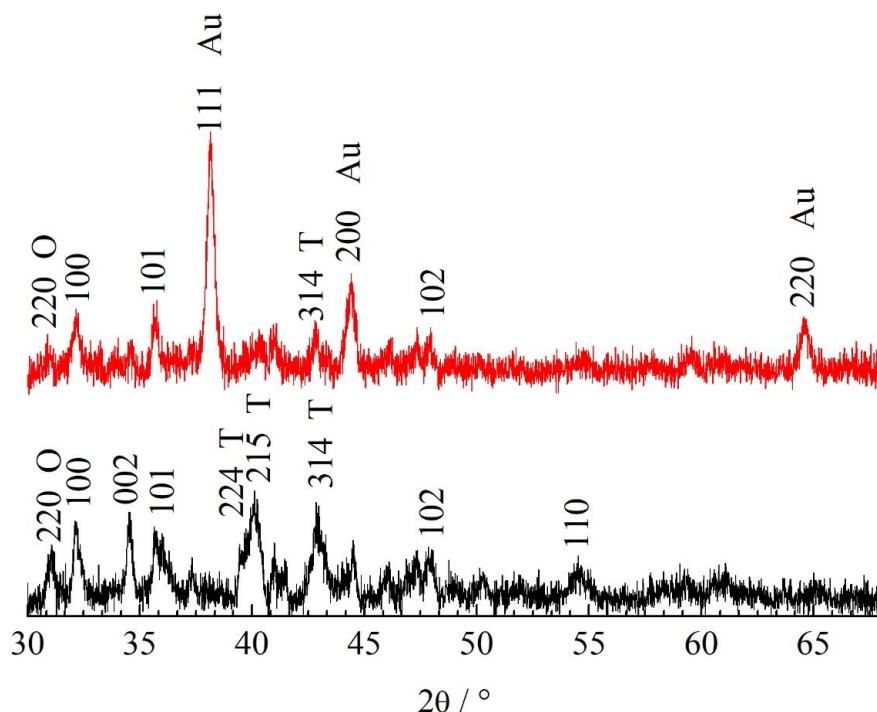
Figure 4.6. XRD patterns for ZnO (black line) and core–shell Au_ZnO (red line). The 100, 002, 102, 101 and 110 reflections belong to the ZnO hexagonal zincite structure. The 220 reflection belongs to the orthorhombic $Zn(OH)_2$ sweetite structure (indicated with the symbol O), whereas the 224, 215 and 314 reflections belong to the tetragonal (indicated with the symbol T) $Zn(OH)_2$ sweetite structure.

79

The morphology and chemical analyses of the core–shell Au_ZnO sample were investigated by TEM and EDX. The TEM microscopy (Figure 4.7a) shows the presence of nanoparticles having a mean radius of about 5-10 nm. In addition, we noted that the Au nanoparticles are highly oriented towards the (111) plane being the measured interplanar distance 2.36 Å (Figure 4.7b). Moreover, Figure 4.7c shows a typical Au_ZnCit⁻ nanoparticle having the core-shell structure. The dark area represents the core Au and the surrounding shell represents the thin, ~ 1-2 nm, layer of ZnCit⁻ capping layer.
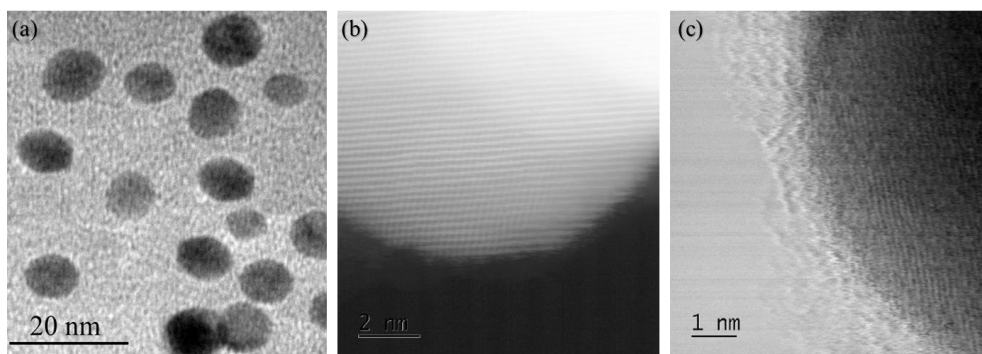
Figure 4.7. a) TEM image showing a large-scale Au_ZnO NPs morphology; b) HAADF-STEM at atomic resolution showing a representative Au NP highly oriented towards the (111) plane with an interplanar distance of 2.36 Å; c) bright-field TEM showing a typical Au_ZnCit⁻ nanoparticle having the core-shell structure. The dark area represents Au and the surrounding shell represents the Zn complex.

EDX analyses (Figure 4.8) demonstrated that the experimental composition of the Au_ZnO nanostructures is identical to the nominal 1.5 % of Au in ZnO.
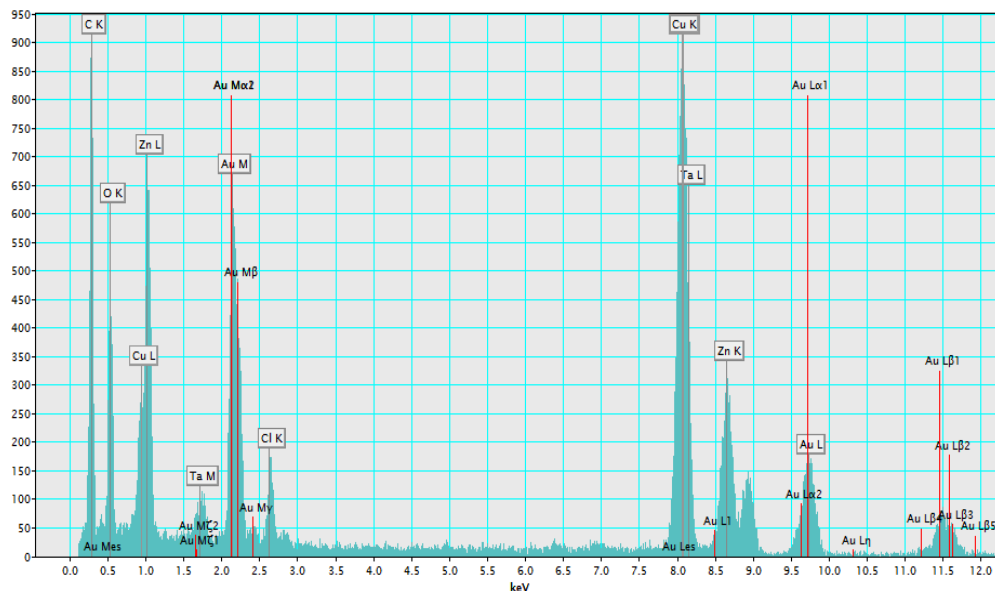
Figure 4.8. EDX of a typical core–shell Au_ZnO nanoparticle.

The optical properties of the synthesized systems were investigated through UV-Vis measurements. UV-Vis experiments were performed by suspending 0.2 mg of ZnO or Au_ZnO in 3 mL of water. A small magnet was used to stir these solutions that remained clear during UV-Vis measurements. The absorbance spectra (Figure 4.9) show a stronger absorption for the Au_ZnO system with respect to the ZnO counterpart, in the whole 200-900 nm range, and this is certainly due to the additional presence in the spectrum of Au_ZnO of the surface plasmon of the Au NPs. It is well known that the surface plasmon of Au NPs appears as a broad band peaked in the 500-600 nm wavelength region, depending on their size and shape.[54, 67, 211, 212] Thus, the absorption of the solution containing Au_ZnO is also due to the presence of the Au NPs plasmon resonance, thus confirming that the coupling of Au NPs with ZnO enhanced the UV-visible photodetection.
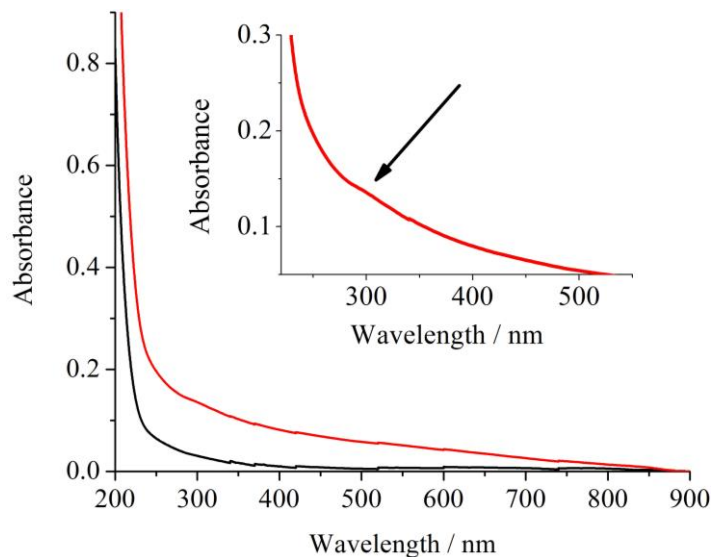
Figure 4.9. UV-Vis absorption spectra of the water solutions obtained by suspending 0.2 mg of ZnO (black line) or Au_ZnO (red line) in 3 mL of water. These solutions have been stirred during UV-Vis measurements. Inset: expanded scale of the UV-Vis Au_ZnO absorption spectrum.

4.4 Photocatalysis Activity of Au_ZnO Core–Shell NPs

Photocatalysis experiments were performed using two quartz cuvettes, each containing 3 mL of a 1.44×10^{-5} M MB aqueous solution, in which we added 0.2 mg of ZnO or Au_ZnO powders. The cuvettes were covered with lids, to avoid the evaporation of the solvent during the experiment and left in the dark for 60 min, to allow the physical adsorption of the dye on the oxides to reach the equilibrium. The measured pH of both solutions was 7.6. UV-Vis spectra before and after the 60 min dark were identical. Then, we added a small magnetic stir bar in each solution, placed them on a magnetic stirrer and left them, covered with lids, under the sun light up to 300 min. The solar irradiation, measured using a THORLABS power meter, was 70 mW/cm^2. Initially, the cuvette solutions

were subjected to fast UV-Vis absorbance measurements after cycles of 10 min irradiation. After 90 min sun light irradiation, UV-Vis measurements were performed every 30 min.

Starting UV-Vis spectra of the two aqueous solutions, each containing 3 mL of a 1.44×10^{-5} M MB and 0.2 mg of ZnO or Au_ZnO powders, significantly differ in the wavelength region below 600 nm, since in the spectrum of the solution containing Au_ZnO, there is the presence of the Au NPs plasmon resonance hidden under the MB absorbance band. For both MB solutions, we observed an evident and monotonic absorbance decrease, consistent with the decomposition/decolouration of the dye (Figure 4.10a, b) upon irradiation. This evidence confirms the ability of both our oxides to act as efficient photocatalysts for water decontamination. A careful inspection of Figure 4.10a, b also indicates that Au_ZnO is more effective than ZnO, and this behaviour is well evident in Figure 4.10. In fact, Figure 4.11 shows that the MB concentration decreases as a function of the irradiation time for all samples with a first-order kinetic law. The curves were fitted in the range between 0 and 6 h with the following decreasing exponential formula: $\ln C/C_0 = -kt$, where k is the discolouration rate constant. The values of the discolouration rate obtained by using sun light are 0.566 and 0.712 h^{-1} ($\pm$ 0.01) for the MB solution in the presence of pure ZnO and core–shell Au_ZnO, respectively, with an increase of the 26% in the latter case. These results are in agreement with the best, already reported, similar data for ZnO catalysts.[213]
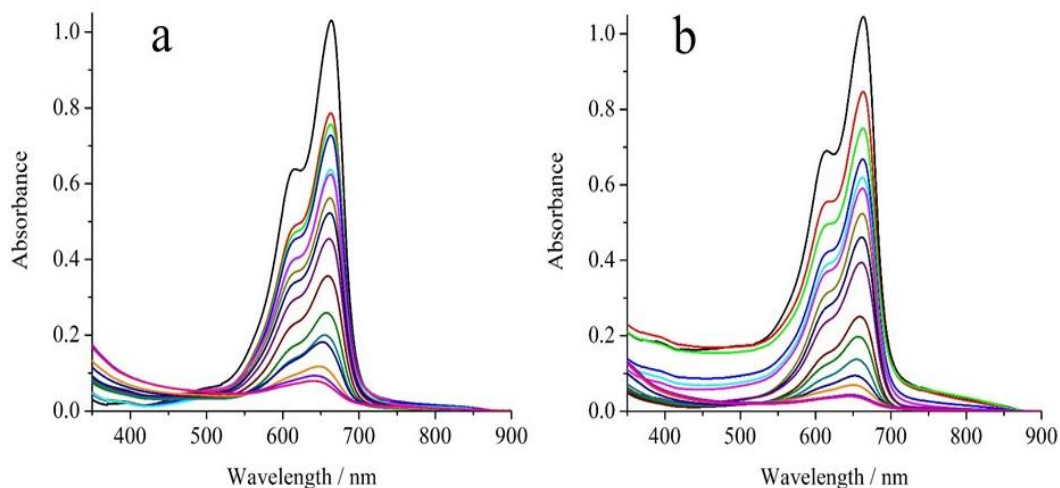
Figure 4.10. a, b) Absorbance spectra for a 1.44×10^{-5} M water solution of MB, exposed to different solar light irradiation times, in presence of ZnO or Au_ZnO. The black, red, green, blue, cyan, magenta, dark yellow, navy, purple, wine, olive, dark cyan, royal, orange, violet and pink lines refer to the starting MB solution at 0, 10, 20, 30, 40, 50, 60, 75, 90, 120, 150, 180, 210, 240, 270, and 300 minutes irradiation time, respectively.
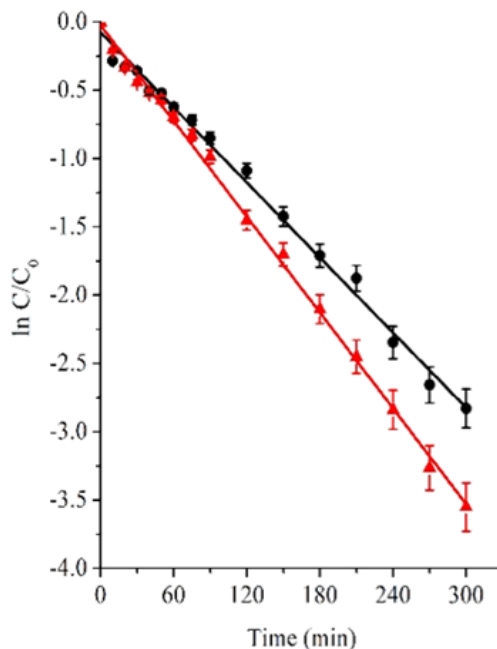
Figure 4.11. Integrated rate behaviour for first-order reaction kinetics, obtained from absorbance measured at 662.2 nm (band maximum) for 1.44×10^{-5} M water solutions of MB, exposed to solar light. Black and red lines are related to the MB with pure ZnO and Au_ZnO, respectively. In both cases the fit goodness was 99%.

The procedure to measure the efficiencies of MB decolouration for ZnO and Au_ZnO samples is described in the following. We started from the tabulated sun irradiance (Figure 4.12): the maximum sun irradiation is 1.32 W/m²/nm at 522 nm, and ~ 0.86 W/m²/nm is observed at both 400 and 800 nm visible limits. Integrating into the 300–2500 nm wavelength range, the solar intensity is calculated to be 830 W/m² (less than 1 kW/m²).
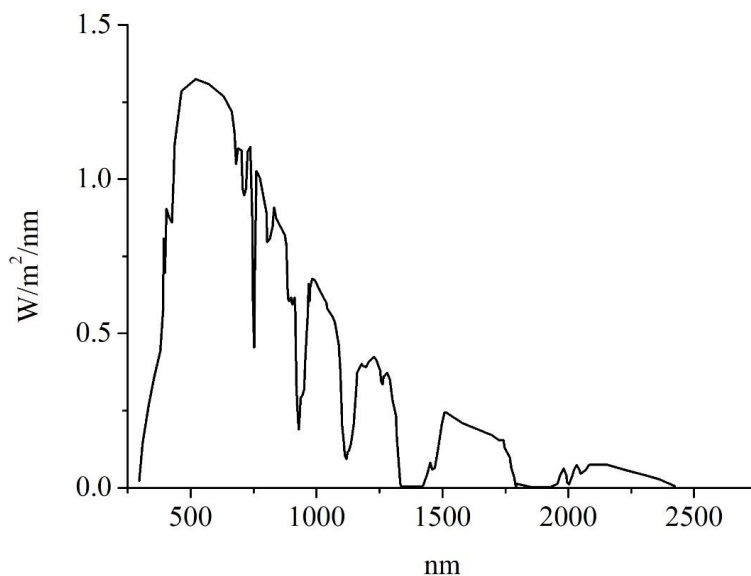
Figure 4.12. Solar irradiance in the 300-2500 wavelength range.

Nevertheless, during our discolouration experiments, we measured an integrated irradiance of 70 mW/cm² = 700 W/m² about 84% of the total tabulated sun irradiance (integrated over 300–2500 nm). To calculate the solar spectrum hitting sample during our experiment, we rescaled the tabulated spectra taking into account the effectively measured intensity. Dividing this solar spectral irradiation by the photon energy at each wavelength and taking into account the exposed surface of the cuvette, we can calculate the number of photons/m²·nm·s (N) hitting our cuvette. The number of photons adsorbed (N_{ass}) by the oxides is

calculated by using the formula $N_{Ass}=N \cdot (1-10^{-absorbance})$, where the absorbance spectra are reported in Figure 4.8 (absorbance of ZnO or Au_ZnO). The number of absorbed photons/m$^2 \cdot$nm$\cdot$s is shown in Figure 4.13 at each wavelength.
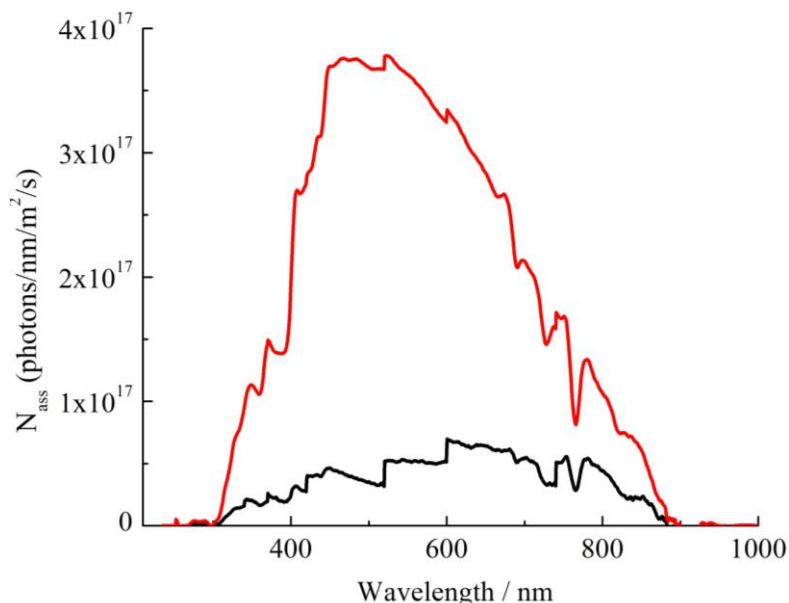
Figure 4.13. Calculated absorbed solar photons for ZnO (black line) and Au_ZnO (red line) catalysts.

According to the absorbance spectra reported in Figure 4.8 and in agreement with our expectation, Au_ZnO (pale grey) absorbs an order of magnitude more photons than ZnO (white) itself. The total number of photons/m$^2 \cdot$nm$\cdot$s between 300–2500 nm is calculated by integrating the curves shown in Figure 4.13 and are reported in Figure 4.14.
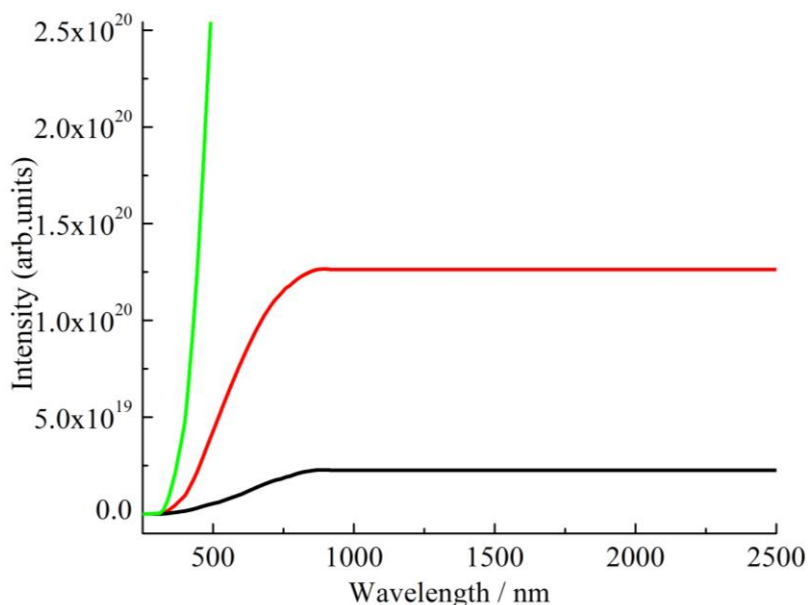
Figure 4.14. Integrated absorbed photons in the 300-2500 nm range corresponding to 2.3×10^{19} and 1.3×10^{20} photons/m^2·s for ZnO (black line) and Au_ZnO (red line) catalysts, respectively. The green line represents the solar irradiance.

The quartz cuvette contained 3 mL of the 1.44×10^{-5} M (2.60×10^{16} MB molecules) water solutions of MB, and only one side of it was exposed to sun light so that the total exposed surface was 3 cm^2. Therefore, after 4 h of solar irradiation (14 400 s), 9.9×10^{19} and 5.7×10^{20} photons are absorbed by each solution, containing ZnO or Au_ZnO, respectively. By using the data of Figure 4.10a,b, after 4h, 2.34×10^{16} and 2.45×10^{16} MB molecules were decomposed by ZnO and Au_ZnO, respectively. By dividing each of these values by the appropriate number of absorbed photons (2.34×10^{16} / 9.9×10^{19} × 100 = 0.024% and 2.45×10^{16} / 5.7×10^{20} × 100 = 0.0043%), we got the quantum efficiency values for the two catalysts (0.024% for ZnO and 0.0043% for Au_ZnO). Therefore, it is evident that Au_ZnO, with respect to ZnO itself, shows an order of magnitude increased absorption (5.7×10^{20}), 26% increased discolouration rate

87

(0.712 h^{-1}), and nevertheless lower quantum efficiency (0.0043%).

Concerning the MB photodegradation mechanism, the irradiation of a semiconductor moves electrons from the valence to the conduction band. The excited electrons and resulting holes have strong reductive and oxidative power, respectively, and produce reactive oxygen species. In this context, it has already been reported that energy edges of valence and conduction bands of semiconductors determine the type of generated reactive oxygen species.[200] Thus, in ZnO, holes react with water to produce hydroxyl radicals, and electrons react with dissolved oxygen to yield superoxide anions. Moreover, superoxide anions can react with holes to form singlet oxygen, during irradiation of ZnO/Au NPs. The reaction of methylen blue with these reactive oxygen species results in N-demethylation of its auxochromic dimethylamine groups plus water and carbon dioxide.

In general, photoactivity is a complex phenomenon which involves several steps: (i) generation of the electron–hole pairs (related to photon absorption), (ii) separation and diffusion of the charge carriers to the active surface sites, (iii) reaction of holes with defects or with the MB on the surface-solution interphase, and (iv) electron scavenging. Therefore, the observed different quantum efficiencies could be due to the different lifetimes of the electron–hole pairs generated by the photons impinging on the two ZnO and Au_ZnO catalysts. The inset reported in Figure 4.9 shows the expanded scale of the absorbance spectrum of Au_ZnO and indicates a small but significant feature at about 300 nm, consistent with the presence of states in the bandgap, absent in the present ZnO system.

It is important to mention that our present study does not allow us to

recognize the nature of compensating defects as cation vacancies, interstitial oxygen, or more complex defect clusters.[214, 215] Nevertheless, it has already been reported that some defect states, associated with the presence of zinc hydroxide $Zn(OH)_2$ layers on the surface of ZnO nanocrystallites, should enhance the photocatalytic activity and, by XRD measurements, we revealed some $Zn(OH)_2$ in the Au_ZnO core-shell NPs.[216, 217]

In addition, we cannot exclude the role of other defects at the grain boundaries as partially responsible for the lower quantum efficiency found using the present Au_ZnO catalyst. It could also be possible due to the presence of a few Au^{3+} ions as dopants that substitute for Zn^{2+} in the zincite ZnO structure. In this case, the extra electron provided by Au^{3+} could go in the 4s–4p hybrid empty conduction band or, more likely, form a localized state deep in the bandgap, as seems evident in the inset of Figure 4.9. These states could be traps for electrons of the electron–hole pair and be responsible for the decreased quantum efficiency of the Au_ZnO catalyst.

Conclusions

In this chapter, the UV–vis photodetection of ZnO was enhanced by about one order of magnitude by obtaining Au_ZnO core–shell nanostructures, prepared by a one-pot synthesis in which the [Zinc Citrate]⁻ complex acted as the ZnO precursor, a reducing agent for Au^{3+}, and a capping anion for the obtained Au(111) NPs. An increased absorption was observed in Au_ZnO because of the additional presence of the surface plasmon resonance of the Au nanoparticles. As already reported for similar systems, electronic interactions between gold and the n-type semiconductor ZnO at their interfaces allows the generation of superoxide species.[218] In fact, using this Au_ZnO photocatalyst, sun light efficiently decomposes a standard methylene blue solution, according to ISO 10678:2010, with a better photocatalytic activity (increased of 26%) than that observed using ZnO, even though the decomposition rate did not increase by an order of magnitude because of the lower quantum efficiency observed for the Au_ZnO system.

References

1. J. H. Gao and B. Xu. *Nano Today* 2009, **4**, 37–51.

2. S. J. Hurst, E. K. Payne, L. D. Qin and C. A. Mirkin. *Angew. Chem. Int. Edit.* 2006, **45**, 2672–2692.

3. E. C. Welch, J. M. Powell, T. B. Clevinger, A. E. Fairman and A. Shukla. *Adv. Funct. Mater.* 2021, **31**, 2104126.

4. F. I. Bohrer, A. Sharoni, C. Colesniuc, J. Park, I. K. Schuller, A. C. Kummel and W. C. Trogler. *J. Am. Chem. Soc.* 2007, **129**, 5640–5646.

5. T. Kudernac, N. Ruangsupapichat, M. Parschau, B. Macia, N. Katsonis, S. R. Harutyunyan, K. H. Ernst and B. L. Feringa. *Nature* 2011, **479**, 208–211.

6. S. Sanvito. *Chem. Soc. Rev.* 2011, **40**, 3336–3355.

7. R. Vincent, S. Klyatskaya, M. Ruben, W. Wernsdorfer and F. Balestro. *Nature* 2012, **488**, 357–360.

8. G. de Ruiter and M. E. van der Boom. *Accounts Chem. Res.* 2011 **44**, 563-573.

9. M. Altman, O. Zenkina, G. Evmenenko, P. Dutta and M. E. van der Boom. *J. Am. Chem. Soc.* 2008, **130**, 5040–5041.

10. F. Lupo, S. Gentile, F. P. Ballistreri, G. A. Tomaselli, M. E. Fragala and A. Gulino. *Analyst* 2010, **135**, 2273–2279.

11. S. V. Orski, A. A. Poloukhtine, S. Arumugam, L. D. Mao, V. V. Popik and J. Locklin. *J. Am. Chem. Soc.* 2010, **132**, 11024–11026.

12. S. Mahouche-Chergui, S. Gam-Derouich, C. Mangeney and M. M. Chehimi. *Chem. Soc. Rev.* 2011, **40**, 4143–4166.

13. D. D. Li and J. H. Yu. *Small* 2016, **12**, 6478–6494.

14. S. I. Stupp and L. C. Palmer. *Chem. Mater.* 2014, **26**, 507–518.

15. P. Murugan, M. Krishnamurthy, S. N. Jaisankar, D. Samanta and A. B. Mandal. *Chem. Soc. Rev.* 2015, **44**, 3212–3243.

16. J. L. Zhang, J. Q. Zhong, J. D. Lin, W. P. Hu, K. Wu, G. Q. Xu, A. T. S. Wee and W. Chen. *Chem. Soc. Rev.* 2015, **44**, 2998–3022.

17. F. K. Chame, M. M. Ojeda, G. F. Gonzalez, V. M. Renteria, M. L. Ojeda and O. C. Velasquez. *J. Alloy Compd.* 2018, **744**, 683–690.

18. M. Runowski, N. Stopikowska, S. Goderski and S. Lis. *J. Alloy Compd.* 2018, **762**, 621–630.

19. J. Reszczynska, T. Grzyb, J. W. Sobczak, W. Lisowski, M. Gazda, B. Ohtani and A. Zaleska. *Appl. Catal. B-Environ.* 2015, **163**, 40–49.

20. M. Azharuddin, G. H. Zhu, D. Das, E. Ozgur, L. Uzun, A. P. F. Turner and H. K. Patra. *Chem. Commun.* 2019, **55**, 6964–6996.

21. J. E. Park, J. Kim and J. M. Nam. *Chem. Sci.* 2017, **8**, 4696–4704.

22. M. C. Daniel and D. Astruc. *Chem. Rev.* 2004, **104**, 293–346.

23. C. J. Murphy, A. M. Gole, J. W. Stone, P. N. Sisco, A. M. Alkilany, E. C. Goldsmith and S. C. Baxter. *Accounts Chem. Res.* 2008, **41**, 1721–1730.

24. A. Corma and H. Garcia. *Chem. Soc. Rev.* 2008, **37**, 2096–2126.

25. W. Park, D. W. Lu and S. M. Ahn. *Chem. Soc. Re.v* 2015, **44**, 2940–2962.

26. N. Xia and Z. K. Wu. *Chem. Sci.* 2021, **12**, 2368–2380.

27. R. C. Jin, C. J. Zeng, M. Zhou and Y. X. Chen. *Chem. Rev.* 2016, **116**, 10346–10413.

28. J. J. Zhang, L. Mou and X. Y. Jiang. *Chem. Sci.* 2020, **11**, 923–936.

29. L. P. Song, Y. J. Huang, Z. H. Nie and T. Chen. *Nanoscale* 2020, **12**, 7433–7460.

30. X. Yang, M. X. Yang, B. Pang, M. Vara and Y. N. Xia. *Chem. Rev.* 2015, **115**, 10410–10488.

31. M. Faraday. *Philos. Trans. R. Soc. London* 1857, **147**, 145.

32. G. Mie. *Ann. Phys.* 1908, **330**, 377–445.

33. A. Klinkova, R. M. Choueiri and E. Kumacheva. *Chem. Soc. Rev.* 2014, **43**, 3976–3991.

34. Y. C. Yeh, B. Creran and V. M. Rotello. *Nanoscale* 2012, **4**, 1871–1880.

35. B. Yan, S. V. Boriskina and B. M. Reinhard. *J. Phys. Chem. C* 2011, **115**, 24437–24453.

36. A. Contino, G. Maccarrone, M. E. Fragala, L. Spitaleri and A. Gulino. *Chem.-Eur. J.* 2017, **23**, 14937–14943.

37. X. M. Qian and S. M. Nie. *Chem. Soc. Rev.* 2008, **37**, 912–920.

38. K. Aslan, I. Gryczynski, J. Malicka, E. Matveeva, J. R. Lakowicz and C. D. Geddes. *Curr. Opin. Biotech.* 2005, **16**, 55–62.

39. T. Ming, H. J. Chen, R. B. Jiang, Q. Li and J. F. Wang. *J. Phys. Chem. Lett.* 2012, **3**, 191–202.

40. J. R. Lakowicz, K. Ray, M. Chowdhury, H. Szmacinski, Y. Fu, J. Zhang and K. Nowaczyk. *Analyst* 2008, **133**, 1308–1346.

41. J. Olesiak-Banska, M. Waszkielewicz, P. Obstarczyk and M. Samoc. *Chem. Soc. Rev.* 2019, **48**, 4087–4117.

42. S. Pillai and M. A. Green. *Sol. Energ. Mat. Sol. C* 2010, **94**, 1481–1486.

43. W. B. Hou and S. B. Cronin. *Adv. Funct. Mater.* 2013, **23**, 1612–1619.

44. T. Y. Zheng, S. Bott and Q. Huo. *Acs Appl. Mater. Inter.* 2016, **8**, 21585–21594.

45. K. Saha, S. S. Agasti, C. Kim, X. N. Li and V. M. Rotello. *Chem. Rev.* 2012, **112**, 2739–2779.

46. B. L. V. Prasad, C. M. Sorensen and K. J. Klabunde. *Chem. Soc. Rev.* 2008, **37**, 1871–1883.

47. E. V. Shevchenko, D. V. Talapin, N. A. Kotov, S. O'Brien and C. B. Murray. *Nature* 2006, **439**, 55–59.

48. Y. Yin and A. P. Alivisatos. *Nature* 2005, **437**, 664–670.

49. A. C. Templeton, J. J. Pietron, R. W. Murray and P. Mulvaney. *J. Phys. Chem. B* 2000, **104**, 564–570.

50. L. B. Zhang and E. K. Wang. *Nano Today* 2014, **9**, 132–157.

51. L. Y. Chen, C. W. Wang, Z. Q. Yuan and H. T. Chang. *Anal. Chem.* 2015, **87**, 216–229.

52. S. A. Diaz, D. A. Hastman, I. L. Medintz and E. Oh. *J. Mater. Chem. B* 2017, **5**, 7907–7926.

53. J. Zheng, C. Zhou, M. X. Yu and J. B. Liu. *Nanoscale* 2012, **4**, 4073–4083.

54. M. R. Jones, K. D. Osberg, R. J. Macfarlane, M. R. Langille and C. A. Mirkin. *Chem. Rev.* 2011, **111**, 3736–3827.

55. S. K. Balasubramanian, L. M. Yang, L. Y. L. Yung, C. N. Ong, W. Y. Ong and L. E. Yu. *Biomaterials* 2010, **31**, 9023–9030.

56. P. X. Zhao, N. Li and D. Astruc. *Coordin. Chem. Rev.* 2013, **257**, 638–665.

57. L. Spitaleri, C. M. A. Gangemi, R. Purrello, G. Nicotra, G. T. Sfrazzetto, G. Casella, M. Casarin and A. Gulino. *Nanomaterials* 2020, **10**, 1644.

58. S. Shankar, M. Orbach, R. Kaminker, M. Lahav and M. E. van der Boom. *Chem.-Eur. J.* 2016, **22**, 1728–1734.

59. M. Boterashvili, T. Shirman, R. Popovitz-Biro, Q. Wen, M. Lahav and M. E. van der Boom. *Chem. Commun.* 2016, **52**, 8079–8082.

60. I. Ojea-Jimenez and V. Puntes. *J. Am. Chem. Soc.* 2009, **131**, 13320–13327.

61. J. W. Park and J. S. Shumaker-Parry. *J. Am. Chem. Soc.* 2014, **136**, 1907–1921.

62. K. Ikeda, K. Takahashi, T. Masuda, H. Kobori, M. Kanehara, T. Teranishi and K. Uosaki. *J. Phys. Chem. C* 2012, **116**, 20806–20811.

63. Y. K. Zheng, L. M. Lai, W. W. Liu, H. Jiang and X. M. Wang. *Adv. Colloid. Interfac.* 2017, **242**, 1–16.

64. R. C. Jin. *Nanoscale* 2015, **7**, 1549–1565.

65. Y. Fang, J. J. Tan, H. Choi, S. Lim and D. H. Kim. *Sensor Actuat B-Chem.* 2018, **259**, 155–161.

66. X. Rao, M. Tatoulian, C. Guyon, S. Ognier, C. L. Chu and A. Abou Hassan. *Nanomaterials* 2019, **9**, 1034.

67. R. J. Macfarlane, B. Lee, M. R. Jones, N. Harris, G. C. Schatz and C. A. Mirkin. *Science* 2011, **334**, 204–208.

68. J. Turkevich, P. C. Stevenson and J. Hillier. *Discuss. Faraday Soc.* 1951, **11**, 55–75.

69. G. Frens. *Nature Phys. Sci.* 1973, **241**, 20–22.

70. M. Brust, M. Walker, D. Bethell, D. J. Schiffrin and R. Whyman. *J. Chem. Soc. Chem. Comm.* 1994, **7**, 801–802.

71. E. Boisselier and D. Astruc. *Chem. Soc. Rev.* 2009, **38**, 1759–1782.

72. D. P. Dubal, O. Ayyad, V. Ruiz and P. Gomez-Romero. *Chem. Soc. Rev.* 2015, **44**, 1777–1790.

73. P. Reiss, E. Couderc, J. De Girolamo and A. Pron. *Nanoscale* 2011, **3**, 446–489.

74. M. B. Gawande, Y. Monga, R. Zboril and R. K. Sharma. *Coordin. Chem. Rev.* 2015, **288**, 118–143.

75. C. Quintana, M. P. Cifuentes and M. G. Humphrey. *Chem. Soc. Rev.* 2020, **49**, 2316–2341.

76. H. H. Jeong, E. Choi, E. Ellis and T. C. Lee. *J. Mater. Chem. B* 2019, **7**, 3480–3496.

77. R. C. Jin, G. Li, S. Sharma, Y. W. Li and X. S. Du. *Chem. Rev.* 2021, **121**, 567–648.

78. D. Garcia-Lojo, S. Nunez-Sanchez, S. Gomez-Grana, M. Grzelczak, I. Pastoriza-Santos, J. Perez-Juste and L. M. Liz-Marzan. *Accounts Chem. Res.* 2019, **52**, 1855–1864.

79. J. Z. Yan, B. K. Teo and N. F. Zheng. *Accounts Chem. Res.* 2018, **51**, 3084–3093.

80. D. Wang, L. J. Niu, Z. Y. Qiao, D. B. Cheng, J. F. Wang, Y. Zhong, F. Bai, H. Wang and H. Y. Fan. *Acs Nano* 2018, **12**, 3796–3803.

81. H. C. Sun, L. Miao, J. X. Li, S. Fu, G. An, C. Y. Si, Z. Y. Dong, Q. Luo, S. J. Yu, J. Y. Xu and J. Q. Liu. *Acs Nano* 2015, **9**, 5461–5469.

82. E. Katz and I. Willner. *Angew. Chem. Int. Edit.* 2004, **43**, 6042–6108.

83. M. Kanehara, H. Takahashi and T. Teranishi. *Angew. Chem. Int. Edit.* 2008, **47**, 307–310.

84. P. Bose, P. Chakraborty, J. S. Mohanty, Nonappa, A. R. Chowdhuri, E. Khatun, T. Ahuja, A. Mahendranath and T. Pradeep. *Nanoscale* 2020, **12**, 22116–22128.

85. R. Kaminker, M. Lahav, L. Motiei, M. Vartanian, R. Popovitz-Biro, M. A. Iron and M. E. van der Boom. *Angew. Chem. Int. Edit.* 2010, **49**, 1218–1221.

86. M. Altman, A. D. Shukla, T. Zubkov, G. Evmenenko, P. Dutta and M. E. van der Boom. *J. Am. Chem. Soc.* 2006, **128**, 7374–7382.

87. R. Hong, J. M. Fernandez, H. Nakade, R. Arvizo, T. Emrick and V. M. Rotello. *Chem. Commun.* 2006, 2347–2349.

88. S. Malola, P. Nieminen, A. Pihlajamaki, J. Hamalainen, T. Karkkainen and H. Hakkinen. *Nat. Commun.* 2019, **10**, 3973.

89. E. C. Dreaden, A. M. Alkilany, X. H. Huang, C. J. Murphy and M. A. El-Sayed. *Chem. Soc. Rev.* 2012, **41**, 2740–2779.

90. W. Xi, W. Zhang, B. K. An, P. L. Burn and J. J. Davis. *J. Mater. Chem.* 2008, **18**, 3109–3120.

91. J. Ohyama, K. Teramura, Y. Higuchi, T. Shishido, Y. Hitomi, K. Aoki, T. Funabiki, M. Kodera, K. Kato, H. Tanida, T. Uruga and T. Tanaka. *Phys. Chem. Chem. Phys.* 2011, **13**, 11128–11135.

92. K. M. Kadish, K. M. Smith and R. Guilard, *Handbook of Porphyrin Science with Applications to Chemistry, Physics, Materials Science, Engineering, Biology and Medicine, Vol 18: Applications and Materials*, 2012, **18**, Xi-Xi.

93. W. Auwarter, K. Seufert, F. Bischoff, D. Ecija, S. Vijayaraghavan, S. Joshi, F. Klappenberger, N. Samudrala and J. V. Barth. *Nat. Nanotechnol.* 2012, **7**, 41–46.

94. J. S. Lindsey and D. F. Bocian. *Accounts Chem. Res.* 2011, **44**, 638–650.

95. Z. M. Liu, A. A. Yasseri, J. S. Lindsey and D. F. Bocian. *Science* 2003, **302**, 1543–1545.

96. D. A. Cristaldi, A. Motta, S. Millesi, T. Gupta, M. Chhatwal and A. Gulino. *J. Mater. Chem. C* 2013, **1**, 4979–4984.

97. X. L. Huang, Y. F. Zhou, L. Ding, G. C. Yu, Y. K. Leng, W. H. Lai, Y. H. Xiong and X. Y. Chen. *Small* 2019, **15**, 1903861.

98. Z. Cao, S. B. Zacate, X. D. Sun, J. J. Liu, E. M. Hale, W. P. Carson, S. B. Tyndall, J. Xu, X. W. Liu, X. C. Liu, C. Song, J. H. Luo, M. J. Cheng, X. D. Wen and W. Liu. *Angew. Chem. Int. Edit.* 2018, **57**, 12675–12679.

99. Y. Kim, B. Kang, H. Y. Ahn, J. Seo and K. T. Nam. *Small* 2017, **13**, 1700071.

100. K. Ikeda, K. Takahashi, T. Masuda and K. Uosaki. *Angew. Chem. Int. Edit.* 2011, **50**, 1280–1284.

101. T. Hasobe, H. Imahori, P. V. Kamat, T. K. Ahn, S. K. Kim, D. Kim, A. Fujimoto, T. Hirakawa and S. Fukuzumi. *J. Am. Chem. Soc.* 2005, **127**, 1216–1228.

102. H. Imahori, A. Fujimoto, S. Kang, H. Hotta, K. Yoshida, T. Umeyama, Y. Matano, S. Isoda, M. Isosomppi, N. V. Tkachenko and H. Lemmetyinen. *Chem.-Eur. J.* 2005, **11**, 7265–7275.

103. H. Imahori, A. Fujimoto, S. Kang, H. Hotta, K. Yoshida, T. Umeyama, Y. Matano and S. Isoda. *Adv. Mater.* 2005, **17**, 1727–1730.

104. J. Ohyama, Y. Hitomi, Y. Higuchi, M. Shinagawa, H. Mukai, M. Kodera, K. Teramura, T. Shishido and T. Tanaka. *Chem. Commun.* 2008, 6300–6302.

105. M. Trapani, M. A. Castriciano, A. Romeo, G. De Luca, N. Machado, B. D. Howes, G. Smulevich and L. M. Scolaro. *Nanomaterials* 2019, **9**, 1026.

106. J. R. Lu, Z. H. Li, W. J. An, L. Liu and W. Q. Cui. *Nanomaterials* 2019, **9**, 1321.

107. M. Trapani, A. Romeo, T. Parisi, M. T. Sciortino, S. Patane, V. Villari and A. Mazzaglia. *Rsc. Adv.* 2013, **3**, 5607–5614.

108. D. Conklin, S. Nanayakkara, T. H. Park, M. F. Lagadec, J. T. Stecher, M. J. Therien and D. A. Bonnell. *Nano Lett.* 2012, **12**, 2414–2419.

109. L. Zhang, H. J. Chen, J. F. Wang, Y. A. F. Li, J. A. Wang, Y. Sang, S. J. Xiao, L. Zhan and C. Z. Huang. *Small* 2010, **6**, 2001–2009.

110. M. Yamada, A. Kuzume, M. Kurihara, K. Kubo and H. Nishihara. *Chem. Commun.* 2001, 2476–2477.

111. C. M. A. Gangemi, R. Randazzo, M. E. Fragala, G. A. Tomaselli, F. P. Ballistreri, A. Pappalardo, R. M. Toscano, G. T. Sfrazzetto, R. Purrello and A. D'Urso. *New J. Chem.* 2015, **39**, 6722–6725.

112. H. X. Shi, Q. Q. Nie, M. Yang, C. J. Wang, E. Z. Liu, Z. Ji and J. Fan. *J. Photoch. Photobio. A* 2020, **389**, 112259.

113. H. H. Deng, G. W. Li, L. Hong, A. L. Liu, W. Chen, X. H. Lin and X. H. Xia. *Food Chem.* 2014, **147**, 257–261.

114. N. Tuccitto, G. T. Sfrazzetto, C. M. A. Gangemi, F. P. Ballistreri, R. M. Toscano, G. A. Tomaselli, A. Pappalardo and G. Marletta. *Chem. Commun.* 2016, **52**, 11681–11684.

115. Z. Zhou and D. Bong. *Langmuir* 2013, **29**, 144–150.

116. H. D. Hill and C. A. Mirkin. *Nat. Protoc.* 2006, **1**, 324–336.

117. M. J. Frisch, G. W. Trucks, H. B. Schlegel, G. E. Scuseria, M. A. Robb, J. R. Cheeseman, G. Scalmani, V. Barone, G. A. Petersson, H. Nakatsuji, X. Li, M. Caricato, A. V. Marenich, J. Bloino, B. G. Janesko, R. Gomperts, B. Mennucci, H. P. Hratchian, J. V. Ortiz, A. F. Izmaylov, J. L. Sonnenberg, Williams, F. Ding, F. Lipparini, F. Egidi, J. Goings, B. Peng, A. Petrone, T. Henderson, D. Ranasinghe, V. G. Zakrzewski, J. Gao, N. Rega, G. Zheng, W. Liang, M. Hada, M. Ehara, K. Toyota, R. Fukuda, J. Hasegawa, M. Ishida, T. Nakajima, Y. Honda, O. Kitao, H. Nakai, T. Vreven, K. Throssell, J. A. Montgomery Jr., J. E. Peralta, F. Ogliaro, M. J. Bearpark, J. J. Heyd, E. N.

Brothers, K. N. Kudin, V. N. Staroverov, T. A. Keith, R. Kobayashi, J. Normand, K. Raghavachari, A. P. Rendell, J. C. Burant, S. S. Iyengar, J. Tomasi, M. Cossi, J. M. Millam, M. Klene, C. Adamo, R. Cammi, J. W. Ochterski, R. L. Martin, K. Morokuma, O. Farkas, J. B. Foresman and D. J. Fox, *Gaussian 09, Revision B.01*; Gaussian, Inc.: Wallingford CT, USA, 2009.

118. D. Briggs and J. T. Grant. *Surface Analysis by Auger and X-Ray Photoelectron Spectroscopy*, IMP: Chichester, UK edn., **2003**.

119. G. Greczynski and L. Hultman. *Angew. Chem. Int. Edit.* 2020, **59**, 5002–5006.

120. A. Gulino. *Anal. Bioanal. Chem.* 2013, **405**, 1479–1495.

121. H. Al-Johani, E. Abou-Hamad, A. Jedidi, C. M. Widdifield, J. Viger-Gravel, S. S. Sangaru, D. Gajan, D. H. Anjum, S. Ould-Chikh, M. N. Hedhili, A. Gurinov, M. J. Kelly, M. El Eter, L. Cavallo, L. Emsley and J. M. Basset. *Nat. Chem.* 2017, **9**, 890–895.

122. M. Zhao, L. H. Meng, L. C. Ma, G. S. Wu, Y. W. Wang, F. Xie and Y. D. Huang. *Rsc Adv.* 2016, **6**, 29654–29662.

123. R. Xue, H. Guo, T. Wang, X. Wang, J. B. Ai, L. G. Yue, Y. L. Wei and W. Yang. *Mater. Lett.* 2017, **209**, 171–174.

124. D. Y. Osadchii, A. I. Olivos-Suarez, A. V. Bavykina and J. Gascon. *Langmuir* 2017, **33**, 14278–14285.

125. Y. F. Zhao, K. X. Yao, B. Y. Teng, T. Zhang and Y. Han. *Energ. Environ. Sci.* 2013, **6**, 3684–3692.

126. C. Yao, G. Y. Li, J. K. Wang, Y. H. Xu and L. M. Chang. *Sci. Rep.* 2018, **8**, 1867.

127. C. I. Olariu, H. H. P. Yiu, L. Bouffier, T. Nedjadi, E. Costello, S. R. Williams, C. M. Halloran and M. J. Rosseinsky. *J. Mater. Chem.* 2011, **21**, 12650–12659.

128. W. H. Ni, T. Ambjornsson, S. P. Apell, H. J. Chen and J. F. Wang. *Nano Lett.* 2010, **10**, 77–84.

129. W. H. Ni, Z. Yang, H. J. Chen, L. Li and J. F. Wang. *J. Am. Chem. Soc.* 2008, **130**, 6692–6693.

130. Y. W. Hao, H. Y. Wang, Y. Jiang, Q. D. Chen, K. Ueno, W. Q. Wang, H. Misawa and H. B. Sun. *Angew. Chem. Int. Edit.* 2011, **50**, 7824–7828.

131. E. Dulkeith, A. C. Morteani, T. Niedereichholz, T. A. Klar, J. Feldmann, S. A. Levi, F. C. J. M. van Veggel, D. N. Reinhoudt, M. Moller and D. I. Gittins. *Phys. Rev. Lett.* 2002, **89**, 203002-1 – 203002-4.

132. E. Dulkeith, M. Ringler, T. A. Klar, J. Feldmann, A. M. Javier and W. J. Parak. *Nano Lett.* 2005, **5**, 585–589.

133. G. Schneider, G. Decher, N. Nerambourg, R. Praho, M. H. V. Werts and M. Blanchard-Desce. *Nano Lett.* 2006, **6**, 530–536.

134. T. L. Jennings, M. P. Singh and G. F. Strouse. *J. Am. Chem. Soc.* 2006, **128**, 5462–5467.

135. H. Q. Li, J. M. Kang, J. H. Yang and B. Wu. *J. Phys. Chem. C* 2016, **120**, 16907–16912.

136. P. Anger, P. Bharadwaj and L. Novotny. *Phys. Rev. Lett.* 2006, **96**, 113002-1 – 113002-4.

137. S. Ida, C. Ogata, D. Shiga, K. Izawa, K. Ikeue and Y. Matsumoto. *Angew. Chem. Int. Edit.* 2008, **47**, 2480–2483.

138. G. Arrachart, I. Karatchevtseva, D. J. Cassidy, G. Triani, J. R. Bartlett and M. W. C. Man. *J. Mater. Chem.* 2008, **18**, 3643–3649.

139. K. L. Ai, B. H. Zhang and L. H. Lu. *Angew. Chem. Int. Edit.* 2009, **48**, 304–308.

140. J. Yuasa, T. Nakagawa, Y. Kita, A. Kaito and T. Kawai. *Chem. Commun.* 2017, **53**, 6748–6751.

141. H. Tsukube and S. Shinoda. *Chem. Rev.* 2002, **102**, 2389–2403.

142. G. Zucchi, T. Jeon, D. Tondelier, D. Aldakov, P. Thuery, M. Ephritikhine and B. Geffroy. *J. Mater. Chem.* 2010, **20**, 2114–2120.

143. K. Binnemans. *Coordin. Chem. Rev.* 2015, **295**, 1–45.

144. J. C. G. Bunzli. *Accounts Chem. Res.* 2006, **39**, 53–61.

145. K. Hanaoka, K. Kikuchi, S. Kobayashi and T. Nagano. *J. Am. Chem. Soc.* 2007, **129**, 13502–13509.

146. E. Deiters, B. Song, A. S. Chauvin, C. D. B. Vandevyver and J. C. G. Bunzli. *New J. Chem.* 2008, **32**, 1140–1152.

147. Z. J. Hu, X. H. Tian, X. H. Zhao, P. Wang, Q. Zhang, P. P. Sun, J. Y. Wu, J. X. Yang and Y. P. Tian. *Chem. Commun.* 2011, **47**, 12467–12469.

148. L. M. Fu, X. F. Wen, X. C. Ai, Y. Sun, Y. S. Wu, J. P. Zhang and Y. Wang. *Angew. Chem. Int. Edit.* 2005, **44**, 747–750.

149. T. Ishida, T. Murayama, A. Taketoshi and M. Haruta. *Chem. Rev.* 2020, **120**, 464–525.

150. H. Kang, J. T. Buchman, R. S. Rodriguez, H. L. Ring, J. Y. He, K. C. Bantz and C. L. Haynes. *Chem. Rev.* 2019, **119**, 664–699.

151. J. F. Li, C. Y. Li and R. F. Aroca. *Chem. Soc. Rev.* 2017, **46**, 3962–3979.

152. H. L. Perry, R. M. Botnar and J. D. E. T. Wilton-Ely. *Chem. Commun.* 2020, **56**, 4037–4046.

153. A. Dutta and A. Chattopadhyay. *J. Phys. Chem. C* 2017, **121**, 18854–18861.

154. C. D. S. Brites, M. C. Fuertes, P. C. Angelome, E. D. Martinez, P. P. Lima, G. J. A. A. Soler-Illia and L. D. Carlos. *Nano Lett.* 2017, **17**, 4746–4752.

155. E. M. Surender, S. Comby, B. L. Cavanagh, O. Brennan, T. C. Lee and T. Gunnlaugsson. *Chem.* 2016, **1**, 438–455.

156. D. J. Lewis and Z. Pikramenou. *Coordin Chem Rev* 2014, **273**, 213–225.

157. R. M. Pallares, K. P. Carter, S. E. Zeltmann, T. Tratnjek, A. M. Minor and R. J. Abergel. *Inorg. Chem.* 2020, **59**, 2030–2036.

158. P. Nath, N. Priyadarshni and N. Chanda. *Acs Appl. Nano Mater.* 2018, **1**, 73–81.

159. M. Milne, P. Gobbo, N. McVicar, R. Bartha, M. S. Workentin and R. H. E. Hudson. *J. Mater. Chem. B* 2013, **1**, 5628–5635.

160. L. K. Truman, S. J. Bradberry, S. Comby, O. Kotova and T. Gunnlaugsson. *Chemphyschem* 2017, **18**, 1746–1751.

161. R. Ranjan, E. N. Esimbekova, M. A. Kirillova and V. A. Kratasyuk. *Anal. Chim. Acta* 2017, **971**, 1–13.

162. Y. F. Zhao, A. L. Wang, J. Kang, H. B. Chu, H. X. Zhang and Y. L. Zhao. *J. Photoch. Photobio. A* 2020, **400**, 112678.

163. Q. R. Wang, J. H. Liu, K. W. Huang, Q. C. Chen, H. C. Dong, D. Zhang, Q. Shi, S. H. Li and W. J. Wang. *Spectrochim. Acta A* 2020, **235**, 118260.

164. J. J. Romero, J. H. Hodak, H. B. Rodriguez and M. C. Gonzalez. *J. Phys. Chem. C* 2018, **122**, 26865–26875.

165. E. Hwang, I. I. Smolyaninov and C. C. Davis. *Nano Lett.* 2010, **10**, 813–820.

166. W. Wang, Y. Zhang, W. Zhang, Y. B. Liu, P. Y. Ma, X. H. Wang, Y. Sun and D. Q. Song. *Anal. Chim. Acta* 2021, **1183**, 338989.

167. Y. Chen, K. K. Wang, F. Chen, S. Q. Chang and H. Q. Zhang. *Anal. Sci.* 2021, **37**, 309–314.

168. R. Ren, S. W. Li, J. Li, J. X. Ma, H. Z. Liu and J. T. Ma. *Catal. Sci. Technol.* 2015, **5**, 2149–2156.

169. A. Contino, G. Maccarrone, L. Spitaleri, L. Torrisi, G. Nicotra and A. Gulino. *Eur. J. Inorg. Chem.* 2018, 4678–4683.

170. A. Gulino, F. Lupo, G. G. Condorelli, A. Motta and I. L. Fragala. *J. Mater. Chem.* 2009, **19**, 3507–3511.

171. G. G. Condorelli, C. Tudisco, A. Motta, A. Di Mauro, F. Lupo, A. Gulino and I. L. Fragala. *Eur. J. Inorg. Chem.* 2010, 4121–4129.

172. Y. Q. Yu, M. Zhou and H. Cui. *J. Mater. Chem.* 2011, **21**, 12622–12625.

173. E. de la Llave, S. E. Herrera, L. P. M. De Leo and F. J. Williams. *J. Phys. Chem. C* 2014, **118**, 21420–21427.

174. S. Tanuma, T. Shiratori, T. Kimura, K. Goto, S. Ichimura and C. J. Powell. *Surf. Interface Anal.* 2005, **37**, 833–845.

175. Z. L. Wang, H. Yang, P. He, Y. H. He, J. S. Zhao and H. J. Tang. *Dalton Trans.* 2016, **45**, 2839–2844.

176. C. Yang, L. M. Fu, Y. Wang, J. P. Zhang, W. T. Wong, X. C. Ai, Y. F. Qiao, B. S. Zou and L. L. Gui. *Angew. Chem. Int. Edit.* 2004, **43**, 5010–5013.

177. S. Cotton. *Lanthanides and actinides*, Macmillan Education LTD, **1991**.

178. J. C. G. Bunzli and C. Piguet. *Chem. Soc. Rev.* 2005, **34**, 1048–1077.

179. B. G. Wybourne and L. Smentek. *Optical Spectroscopy of Lanthanides – Magnetic and Hyperfine Interactions*, Taylor & Francis Group, **2007**.

180. A. Gulino, S. Di Bella, I. Fragala, M. Casarin, A. M. Seyam and T. J. Marks. *Inorg. Chem.* 1993, **32**, 3873–3879.

181. A. Gulino, M. Casarin, V. P. Conticello, J. G. Gaudiello, H. Mauermann, I. Fragala and T. J. Marks. *Organometallics* 1988, **7**, 2360–2364.

182. I. L. Fragalà and A. Gulino. In *Fundamental and Technological Aspects of Organo-f-Element Chemistry*, eds. T. J. Marks and I. L. Fragalà, Springer, Dordrecht, 1 edn., **1985**, pp. 327–360.

183. S. Fujihara and K. Tokumo. *Chem. Mater.* 2005, **17**, 5587–5593.

184. X. Zhang, C. A. Marocico, M. Lunz, V. A. Gerard, Y. K. Gun'ko, V. Lesnyak, N. Gaponik, A. S. Susha, A. L. Rogach and A. L. Bradley. *Acs Nano* 2014, **8**, 1273–1283.

185. J. J. Stewart. *MOPAC2012*, Stewart Computational Chemistry, Colorado Springs, CO, http://OpenMOPAC.net, **2012**.

186. S. Mayilo, M. A. Kloster, M. Wunderlich, A. Lutich, T. A. Klar, A. Nichtl, K. Kurzinger, F. D. Stefani and J. Feldmann. *Nano Lett.* 2009, **9**, 4558–4563.

187. Z. Zhang, M. Choi, M. Baek, Z. X. Deng and K. Yong. *Acs Appl. Mater. Inter.* 2017, **9**, 3967–3976.

188. S. Xu and Z. L. Wang. *Nano Res.* 2011, **4**, 1013–1098.

189. C. Klingshirn, J. Fallert, H. Zhou, J. Sartor, C. Thiele, F. Maier-Flaig, D. Schneider and H. Kalt. *Phys. Status Solidi B* 2010, **247**, 1424–1447.

190. J. N. Anker, W. P. Hall, O. Lyandres, N. C. Shah, J. Zhao and R. P. Van Duyne. *Nat. Mater.* 2008, **7**, 442–453.

191. X. Q. Liu, J. Iocozzia, Y. Wang, X. Cui, Y. H. Chen, S. Q. Zhao, Z. Li and Z. Q. Lin. *Energ. Environ. Sci.* 2017, **10**, 402–434.

192. J. A. Rodriguez, S. D. Senanayake, D. Stacchiola, P. Liu and J. Hrbek. *Accounts Chem. Res.* 2014, **47**, 773–782.

193. J. Cure, H. Assi, K. Cocq, L. Marin, K. Fajerwerg, P. Fau, E. Beche, Y. J. Chabal, A. Esteve and C. Rossi. *Langmuir* 2018, **34**, 1932–1940.

194. P. She, K. L. Xu, S. Y. Yin, Y. X. Shang, Q. R. He, S. Zeng, H. Sun and Z. N. Liu. *J. Colloid. Interf. Sci.* 2018, **514**, 40–48.

195. Y. Zhang, J. B. Zhou, Z. Li and Q. Q. Feng. *J. Mater. Sci.* 2018, **53**, 3149–3162.

196. M. K. Choudhary, J. Kataria and S. Sharma. *Acs Appl. Nano. Mater.* 2018, **1**, 1870–1878.

197. X. M. Jiang, W. W. He, X. W. Zhang, Y. Wu, Q. Zhang, G. J. Cao, H. Zhang, J. W. Zheng, T. R. Croley and J. J. Yin. *J. Phys. Chem. C* 2018, **122**, 29414–29425.

198. Z. H. Bao, Y. Yuan, C. B. Leng, L. Li, K. Zhao and Z. H. Sun. *Acs Appl. Mater. Inter.* 2017, **9**, 16417–16425.

199. W. H. Lin, Y. H. Chiu, P. W. Shao and Y. J. Hsu. *Acs Appl. Mater. Inter.* 2016, **8**, 32754–32763.

200. W. W. He, H. K. Kim, W. G. Warner, D. Melka, J. H. Callahan and J. J. Yin. *J. Am. Chem. Soc.* 2014, **136**, 750–757.

201. T. H. Yang, L. D. Huang, Y. W. Harn, C. C. Lin, J. K. Chang, C. I. Wu and J. M. Wu. *Small* 2013, **9**, 3169–3182.

202. E. J. Guidelli, O. Baffa and D. R. Clarke. *Sci. Rep.* 2015, **5**, 14004.

203. K. K. Haldar and T. Sen. *J. Colloid. Interf. Sci.* 2016, **484**, 263–269.

204. H. V. Thang and G. Pacchioni. *J. Phys. Chem. C* 2018, **122**, 20880–20887.

205. D. S. Rahman and S. K. Ghosh. *J. Phys. Chem. C* 2016, **120**, 14906–14917.

206. G. Schön. *J. Electron. Spectrosc. Relat. Phenom.* 1973, **2**, 75–86.

207. A. Gulino, F. Lupo and M. E. Fragala. *J. Phys. Chem. C* 2008, **112**, 13869–13872.

208. A. Gulino, P. Dapporto, P. Rossi and I. Fragala. *Chem. Mater.* 2002, **14**, 4955–4962.

209. A. Gulino and I. Fragala. *Chem. Mater.* 2002, **14**, 116–121.

210. S. Arunkumar, T. F. Hou, Y. B. Kim, B. Choi, S. H. Park, S. Jung and D. W. Lee. *Sensor Actuat. B-Chem.* 2017, **243**, 990–1001.

211. A. M. Kalsin, M. Fialkowski, M. Paszewski, S. K. Smoukov, K. J. M. Bishop and B. A. Grzybowski. *Science* 2006, **312**, 420–424.

212. L. Manna, D. J. Milliron, A. Meisel, E. C. Scher and A. P. Alivisatos. *Nat. Mater.* 2003, **2**, 382–385.

213. M. Zimbone, G. Cacciato, M. Boutinguiza, A. Gulino, M. Cantarella, V. Privitera and M. G. Grimaldi. *Catal. Today.* 2019, **321**, 146–157.

214. M. Zimbone, G. Cacciato, L. Spitaleri, R. G. Egdell, M. G. Grimaldi and A. Gulino. *Acs Omega* 2018, **3**, 11270–11277.

215. A. Gulino, A. E. Taverner, S. Warren, P. Harris and R. G. Egdell. *Surf. Sci.* 1994, **315**, 351–361.

216. J. M. Wu and Y. R. Chen. *J. Phys. Chem. C* 2011, **115**, 2235–2243.

217. D. S. Bohle and C. J. Spina. *J. Am. Chem. Soc.* 2007, **129**, 12380–12381.

218. G. Corro, S. Cebada, U. Pal and J. L. G. Fierro. *J. Catal.* 2017, **347**, 148–156.

General Conclusions

The aim of this PhD thesis was the fabrication of hybrid plasmonic and/or luminescent nanostructures showing optical, electrical, or catalytic properties in the perspective of their applications in different fields of nanotechnology.

All the investigated systems were obtained by a bottom-up approach that involves the self-assembly of appropriate emissive molecules on plasmonic gold nanoparticles.

In all synthesized hybrid sytems, the core is represented by plasmonic gold nanoparticles on the surface of which functional emissive molecules have been anchored, thus allowing the fabrication of covalent nanostructures that show the combination of the starting properties of the interacting building blocks. This method allowed obtaining the manufacture of highly organized networks of Au nanoparticles self-assembled through a new bi-functional porphyrin molecule. The bi-functional porphyrin molecules covalently bonded to the surface of the gold NPs resulted in a new optical material showing a strong surface plasmon, due to the Au nanoparticles, and a strong luminescence signal coming from porphyrin molecules.

Furthermore, we obtained the synthesis of Au nanoparticles decorated with two slightly different Eu(III) complexes. Both functional architectures exhibit a surface plasmon, due to the Au nanoparticles but only $EuNH_2$@Au maintains, in addition, some luminescence signal, thus giving a new optical material having unique characteristics. In fact, we demonstrated the covalent dye-Au NP

interaction hinders some Eu(III) emission quenching mechanism. In contrast, the Eu complex which can only interact through space with Au NPs shows a total quenching mechanism of its emission.

A real advantage of the covalent assembly is represented by the robustness of the obtained nanostructures and, sometimes, the unicity of their properties. As an example, the photocatalytic properties of the Au_ZnO core–shell nanostructures prepared by a one-pot synthesis led to an about one order of magnitude enhance of UV–vis photodetection of ZnO. An increased absorption was observed in Au_ZnO because of the additional presence of the surface plasmon resonance of the Au nanoparticles.

Therefore, using this Au_ZnO photocatalyst, sun light efficiently decomposes a standard methylene blue solution, according to ISO 10678:2010, with better photocatalytic activity than that observed using ZnO.

To sum up, a major goal of this thesis was the combination of inorganic/organic systems on gold nanoparticles properties. Thus, the covalent assembly of suitable molecules on gold nanoparticles surfaces allows the synthesis of hybrid architectures showing peculiar and unique properties appealing for future applications in plasmon-enhanced fluorescence, heat generation, photocatalysis, nonlinear optics, solar cells, nanofluidics, photoacoustic, photothermal imaging, cancer therapy, drug delivery, nanotherapeutics, etc., under atmospheric conditions, since our systems are not reactive to air nor to water and do not need to be stored in a vacuum or inert gas. Noteworthy, these hybrid molecular-nanoparticle materials both show a strong surface plasmon and a strong luminescence signal.

Appendix

Materials and Characterization

techniques used in this work

All reagents and solvents used in this thesis were purchased from Sigma-Aldrich and used without further purification due to their high degree of purity. The synthesized nanostructures were investigated using the techniques and instrumentation described in the following paragraphs.

Trasmission Electron Microscopy

Transmission electron microscopy (TEM) is an ideal technique for the morphological characterization of nanomaterials to provide structure, grain size, morphology, chemical compositional and crystallography information.

A TEM has several components, which include a vacuum system in which the electrons travel, an electron emission source for the generation of the electron stream, a series of electromagnetic lenses as well as electrostatic plates that allow to guide and manipulate the beam. Also, is required a device to allow the insertion into, motion within, and removal of specimens from the beam path. Imaging devices are subsequently used to create an image from the electrons that have interacted with the system.

A heated tungsten filament in the electron gun produces a high-energy electron beam (from 60 to 300 KeV) that through multiple electromagnetic is collimated and focused on the surface of a thin sample (<100 nm). On reaching the sample, the interactions with the electrons and the atoms generate a high-resolution image.

During transmission, the speed of electrons directly correlates to electron wavelength; the faster electrons move, the shorter wavelength and the greater the quality and detail of the image. The denser the sample, the more the electrons are scattered forming a darker image because fewer electron reaches the screen for visualization while thinner, more transparent specimens appear brighter because a greater number of electrons were able to pass through the sample. These differences provide information on the structure, texture, shape, and size of the sample.

The image can be manipulated by adjusting the voltage of the gun to accelerate or decrease the speed of electrons as well as changing the electromagnetic wavelength via the solenoids.

In function on how the electron source/beam is generated, how the electron beam is manipulated, and/or what kind of signal is collected following the interaction of the electron beam with the sample, it is possible to obtain different information (Figure 1). In this context, it is possible to distinguish different techniques: (i) high-resolution transmission electron microscopy (HRTEM) if the phase contrast and lattice structural image are emphasized; (ii) scanning transmission electron microscopy (STEM) if a focused beam is scanned over the sample; (iii) energy-dispersive X-ray spectroscopy (EDXS) if the electron beam is scanned across the sample surface, it generates the emission of X-ray

fluorescence from the atoms in its path and electron energy-loss spectroscopy and, finally, (iv) electron energy-loss spectroscopy (EELS) if the signals related to the inelastic electron scattering process are collected.
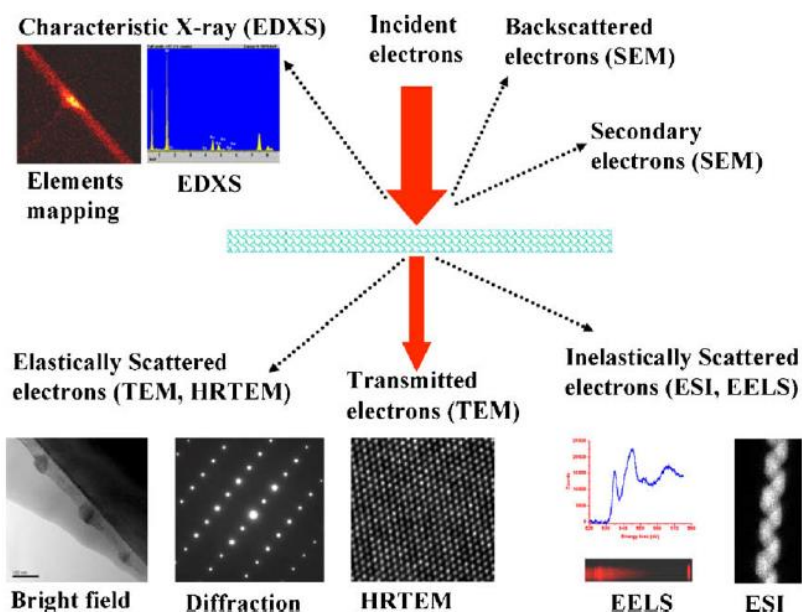
Figure 1. Schematic drawing showing the interaction of electrons beam with a thin section of sample and the signals that are used either for the formation of image or spectroscopy.

EDXS can be used to identify the elemental composition of materials because the energy of each X-ray photon emitted from a specimen is characteristic of the difference in energy between the two shells and of the atomic structure of the emitting element. In fact, the incident beam may excite an electron in an inner shell, ejecting it from the shell while creating an electron hole where the electron was. An electron from an outer, higher-energy shell then fills the hole, and the difference in energy between the higher-energy shell and the lower energy shell may be released in the form of an X-ray.

For TEM analysis, samples need to be thin enough for electrons to pass through, a property known as "electron transparency". Types of preparation include dehydration, gold or graphene sputter coating in case of non-conductive materials, cryofixation, etc.

The morphology of all the nanostructures synthesized in this thesis was investigated by TEM measurements using an Atomic Resolution Analytical Microscope (JEOL ARM200F Cs-corrected). The samples were placed on Cu/C TEM Grid. Electron Energy Loss Spectroscopy (EELS) and Energy Dispersive X-ray (EDX) chemical analyses were performed using a 60 KeV electron beam.

Dynamic Light Scattering

Dynamic light scattering (DLS) is a non-invasive technique used to measure the size distribution profiles and to detect the presence of aggregation of colloidal samples such as particles, micelles, polysaccharides, and supramolecular aggregates like supramolecular polymers.

DLS measures the temporal fluctuations of the light scattering intensity due to the Brownian motions of the particles that move continuously and randomly in solution depending on their size, when a solution containing the particles is placed in the path of a laser beam.[1] Consequently, it allows obtaining the hydrodynamic parameters of particles or macromolecules in solution, such as hydrodynamic radius (R_H). Therefore, at the same temperature and viscosity, the small particles move rapidly and give rapid variations in the scattering intensity, while the large particles move more slowly and generate slow intensity variations. Hence, the DLS instrument will generate a correlation function that

is mathematically linked with particle size and its time-dependent light scattering capacity using the Stokes-Einstein equation:

$$D = \frac{k_B\,T}{6\,\pi\,\eta\,R_H}$$

in which, D is diffusion coefficient, k_B is Boltzmann's constant, T is temperature, η is solvent viscosity, and R_H is the hydrodynamic radius of the particles in solution.

The size characterization of the present hybrid nanoparticles was performed using both DLS and TEM. In fact, the hydrodynamic radius gives information of the inorganic core along with any coating material and solvent layer attached to the particle.[2] The present DLS analysis was performed using a miniDAWN Treos (Wyatt Technology) multi-angle light scattering detector, equipped with a Wyatt QELS DLS Module, at 25°C.

X-ray Diffraction

X-ray diffraction (XRD) is a rapid and powerful non-destructive analysis technique, which can be conducted at room temperature and pressure, for determining the crystal structure of materials. It provides information on structures, phases, preferred crystal orientations (texture), and other structural parameters, such as average grain size, crystallinity, strain, and crystal defects.

XRD analysis is based on constructive interference of a monochromatic beam of X-rays scattered at specific angles from each set of lattice planes in a crystalline sample.

The X-rays are generated by a cathode ray tube, filtered to produce monochromatic radiation, collimated to concentrate, and directed toward the

sample. The interaction of the incident rays with the sample produces constructive interference (and a diffracted ray) when conditions satisfy Bragg's Law ($n\lambda = 2d \sin \theta$). This law relates the wavelength of electromagnetic radiation to the diffraction angle and the lattice spacing in a crystalline sample.

The XRD peak angles and intensities are determined by the atomic positions within the lattice planes. Consequently, the XRD pattern is the fingerprint of periodic atomic arrangements in each material. An online search of a standard database for X-ray powder diffraction patterns enables quick phase identification for a large variety of crystalline samples.

The crystal structure of both ZnO and core–shell Au_ZnO powders was investigated by XRD measurements using a D8 Discover Bruker AXS diffractometer (Cu kα source) equipped with soller silts and operating in 2theta-omega geometry. The patterns were acquired with a 0.01° step size and a step time of 10 s/step. The powder compounds were pelletized between tungsten carbide dies at 500 kg/cm and then loaded on the sample holder.

UV-Vis Spectroscopy

Ultraviolet-visible (UV-Vis) spectroscopy is a type of absorption spectroscopy in which UV-visible light is absorbed by the molecule. Absorption of the UV-visible radiations results in the excitation of the electrons from lower to higher energy levels. The technique is based on the measurement of the intensity of the incident monochromatic radiation produced by a suitable source (I_0) and that of the radiation that reaches the detector after interacting with the sample under examination (I) (Figure 2).
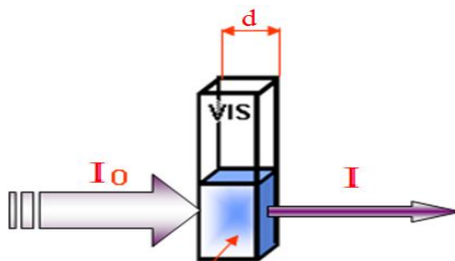
Figure 2. Absorption phenomenon by the solution with consequent attenuation of the intensity of the monochromatic ray from I_0 to I.

By comparing the incident radiation (I_0) and the transmitted radiation (I), the amount of light absorbed by the sample at that specific wavelength can be easily calculated. Using the Beer–Lambert law, this absorption can be used to determine concentrations of solutions:

$$A = \log \frac{I_0}{I} = \varepsilon \cdot L \cdot C$$

where A is the measured absorbance, I_0 is the intensity of the incident light at a given wavelength, I is the transmitted intensity, L is the path length through the sample (cm), c is the concentration of the absorbing species (mol L^{-1}), and ε is the molar absorptivity or extinction coefficient (L mol^{-1} cm^{-1}). According to this relationship, the concentration of the analyte can be calculated when ε is known, L is fixed, and I_0 and I are measured.

UV-vis spectroscopy can also be used for the characterization of solid materials on the nanometre scale, e.g. noble metal nanoparticles, when they are homogeneously dispersed in solvents, by measuring the Surface Plasmon Resonance (SPR) to get information on their size, stability, and aggregation.[3]

The optical properties of the nanostructures synthesized in this PhD thesis, were investigated using a UV-Vis V-650 Jasco spectrometer and the spectra

were recorded with a 0.2 nm resolution at room temperature in quartz cells with a path length of 1 cm (3.5 mL capacity).

Photoluminescence Spectroscopy

Photoluminescence (PL) is a process in which a substance emits light (usually at somewhat lower energies with a smaller number of photons) after the absorption of photons (electromagnetic radiation).

The physical principle of photoluminescence is depicted by the Jablonski diagram (Figure 3).[4] Absorption of photons promotes an electron from the electronic ground state (S_0) to certain vibrational levels ($v = 0, 1, 2, …$), of the first (S_1) or higher electronic excited state ($S_{2,3} …$). The excited electron relaxes to the lowest S_1 state through internal conversion (IC), which occurs when a vibrational state of an electronically excited state can couple to a vibrational state of a lower electronic state. The resulting electron can further deactivate either radiatively by emitting a photon (FL) or non-radiatively through one of three processes: (1) IC quenching to the ground state; (2) collisional quenching (CQ) to the ground state; or (3) intersystem crossing (ISC) to a triplet excited states (T_1) that usually lies at lower energy relative to S_1. Then, the electron can either emit a photon by phosphorescence or deactivate through IC to S_0.
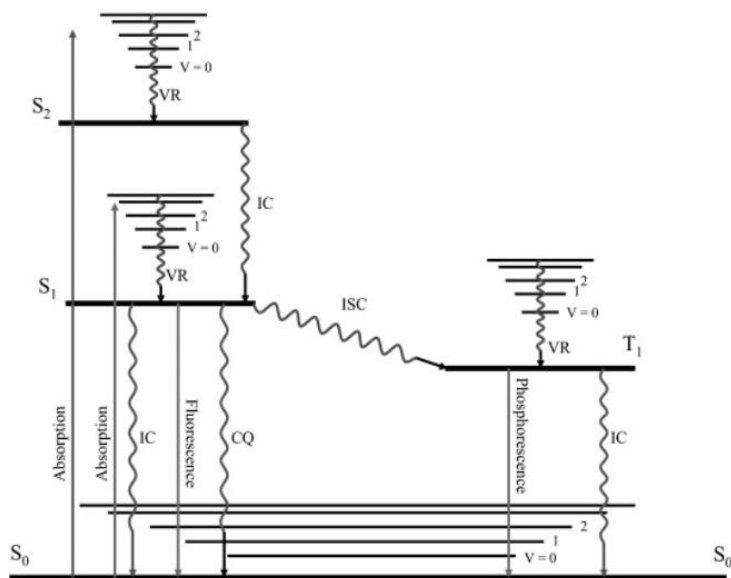
Figure 3. Jablonski diagram showing principles of photoluminescence spectroscopy.

For molecular materials, the intensity and profile of the photoluminescence spectra are direct measures of various important material properties such as the relative energies of the ground and excited states, electronic transitions and concentrations of the emitting species. Furthermore, the temporal dependence of the photoluminescence reflects the relaxation characteristics of the excited state, molecular bonding environment, and identification and quantification of photoluminescence quenchers.

Present luminescence measurements were carried out using a Varian Cary Eclipse fluorescence spectrophotometer with 1 nm resolution and at room temperature in quartz cells with a path length of 1 cm (3.5 mL capacity). The emission was recorded at 90° with respect to the exciting line beam using 5:5 slit widths.

X-Ray Photoelectron Spectroscopy

X-ray photoelectron spectroscopy (XPS) is a widely used technique to investigate the electronic structure and chemical composition of surfaces. It provides information on the oxidation states and on the chemical environment of the studied species and allows estimation of the surface elemental composition, once the relevant atomic sensitivity factors have been taken into account.

It was developed in the mid-1960's by Kai Siegbahn and his research group at the University of Uppsala, Sweden. The XPS technique is used to measure:

- elemental composition of surfaces (top 0–10 nm usually);
- chemical or electronic state of each element in the surface;
- uniformity of elemental composition across the surface (or line profiling or mapping);
- uniformity of elemental composition as a function of ion beam etching (or depth profiling).

The phenomenon is based on the photoelectric effect, outlined by Einstein in 1905, where the concept of the photon was used to describe the ejection of electrons from a surface when photons impinge upon it (Figure 4).

$$A + h\nu \rightarrow A^+ + \ e^-$$
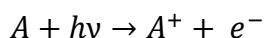
Irradiation causes the emission of photoelectrons whose kinetic energy is proportional to the incident radiation frequency, while their number is proportional to the radiation intensity.
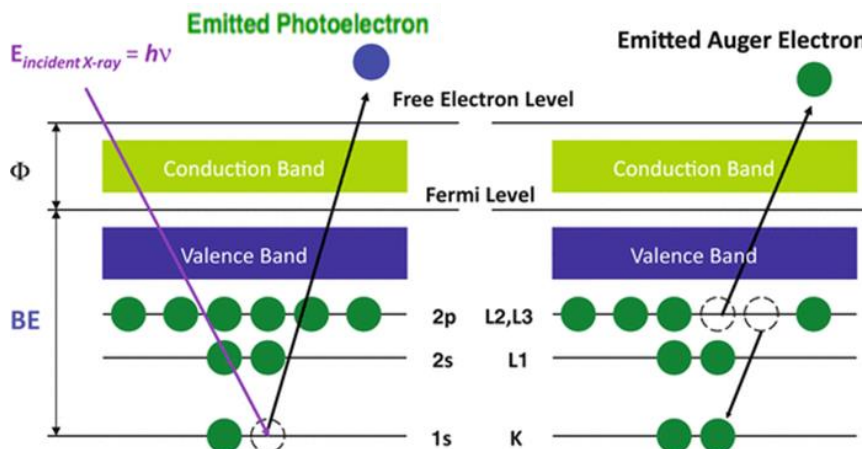
Figure 4. Scheme of the photoemission and Auger processes.

In addition to photoelectrons, after 10^{-14} seconds of this photoelectric process, Auger electrons may be emitted because of the relaxation of the excited ions remaining after photoemission (Figure 4).

In the Auger process, an electron from a higher-level shell fills a core-level vacancy, and at the same time a second electron is emitted, carrying off the excess energy. The Auger electron possesses kinetic energy equal to the difference between the energy of the initial ion and the doubly charged fmal ion and is independent of the energy of the photon creating the core-level vacancy.

Thus, photoionization causes the emission of two electrons (a photoelectron and an Auger electron) and the sum of the kinetic energies of these electrons emitted cannot exceed the energy of the ionizing photons.

A typical XPS instrument has an analysis chamber kept at ultra-high vacuum, ca. 10^{-8} Pa and the X-ray sources typically used are Al (1486.6 eV) or Mg (1253.6 eV) Kα radiations that induce the emission of electrons from the inner energetic levels (core electrons) of each element present on the surface of the analysed material.

The vacuum is essential to maximize the path of the electrons out of the material, without collision with other gaseous substances present in the chamber, allowing thus them to reach the detector. Moreover, it reduces the probability of finding contaminants absorbed on the surface of the sample, such as water and oxygen. X-ray photoelectron spectra are thus collected by measuring the kinetic energy and number of electrons that escape from a few tens of angstroms of the surface.

In detail, when X-rays illuminate an area of a sample cause ejection of electrons with a range of energies and directions. The electron optics, which may be a set of electrostatic and/or magnetic lens units, collect a proportion of these emitted electrons defined by those rays that can be transferred through the apertures and focused onto the analyser entrance slit. Electrostatic fields within the hemispherical analyser (HSA) are established to only allow electrons of a given energy (the so-called Pass Energy, PE) to arrive at the detector slits and onto the detectors themselves. Electrons of a specific initial kinetic energy are measured by setting voltages for the lens system that both focus onto the entrance slit the electrons of the required initial energy and retards their velocity so that their kinetic energy after passing through the transfer lenses matches the pass energy of the hemispherical analyser. To record a spectrum over a range of initial excitation energies it is necessary to scan the voltages applied to these transfer lenses. Thus, known the energy of the incident beam and the kinetic energy of the families of ejected photoelectrons, it is possible to measure the Binding Energy value (B.E.) using the following equation:

$$E_K = h\nu - B.E. - W$$

where hv is the energy of the incident photon, E_k is the kinetic energy of the ejected electron, B.E. is the binding energy of the ejected electron, and W is the work function depending on both the spectrometer and the material.

According to Koopman's theorem, the measured B.E. corresponds to the energy difference between the initial state of an atom with "n" electrons and the final state with "n-1" electrons:

$$B.E. = E_{final} (n-1) - E_{initial} (n)$$

This is true only if the "frozen orbit" hypothesis (frozen or sudden approximation), is valid (no relaxation phenomenon after photoemission). In fact, according to this theorem it is believed that the atomic orbitals remain unchanged upon the ionization. It is known that as a result of ionization, the n-1 number of electrons of the ion affects the correlation energy and there is an electronic rearrangement, but the XPS energy resolution (~ 0.5 eV) allows to neglect these effects.

The different atomic species can be identified by their B.E. which depend on the oxidation state and chemical environment of the analyzed atom (chemical shift). Furthermore, electrons from p, d or f orbitals give two signals (due to the coupling between the spin angular momentum (s) and the orbital angular momentum (l)) with separation energy characteristic of the atom (spin-orbit coupling), while the intensity ratio between the respective areas of the peaks is only as a function of the type of orbital from which the peaks arise. For the identification of the elements, it can thus be exploited also their spin-orbit separation.

In addition, it should be outlined that the XPS is a surface technique since the thickness from which the signals arise typically ranges from 0 to 100 Å, although the X-radiation penetrates into the solid for about 10^4 Å. In fact, the electrons ejected from core orbitals in the ionization process can be subjected to impact (inelastic scattering) within the solid, which determines an energy loss not allowing these to reach the surface and be expelled. Therefore, the sampling depth of the emitted electrons originate is defined as:

$$d = 3\lambda \cdot \text{sen}\theta$$

where λ is the electron mean free path within the solid (about 30 Å) and θ is the take-off angle between the sample surface and the analyzer direction.

It results evident that the higher the take-off angle the higher the sampling depth.

Finally, with XPS technique it is possible to perform quantitative analyses. XPS peak intensity $I(\varepsilon i)$ is correlated to the number of emitted photoelectrons and depends on several factors:

$$I(\varepsilon_i) = I_0 \cdot \eta_i \cdot \sigma(\varepsilon_i) \cdot \lambda(\varepsilon_i) \cdot D(\varepsilon_i)$$

- I_0: X-ray flux intensity;
- η_i: atomic density of the i element;
- $\sigma(\varepsilon_i)$: cross section for the photoelectron extraction;
- $\lambda(\varepsilon_i)$: mean free path of photoelectrons in the sample;
- $D(\varepsilon_i)$: detector and analyser efficiency.

From the intensities of the peaks, it is possible to obtain the atomic concentrations in the sample studied through the formula:

$$C_x = \frac{\eta_x}{\sum \eta_i} = \frac{I_x}{S_x} \times \frac{1}{\sum \dfrac{I_i}{S_i}}$$

where η is the atomic density of the element per volume unit (cm^3), S is the atomic sensitivity factor, and I is the peak intensity.

Before using the intensities of the peaks for the quantitative analysis it is necessary the removal of the background determined from all those photoelectrons that lose energy before reaching the detector. Methods to be used for this correction are (i) linear subtraction, (ii) Shirley, and (iii) Tougaard.

The main components of an XP spectrometer system include a source of X-rays, an ultra-high vacuum (UHV) stainless steel chamber with UHV pumps, an electron energy analyser, an electron detector system, a moderate vacuum sample introduction chamber, sample mounts, a sample stage, and a set of stage manipulators (Figure 5).
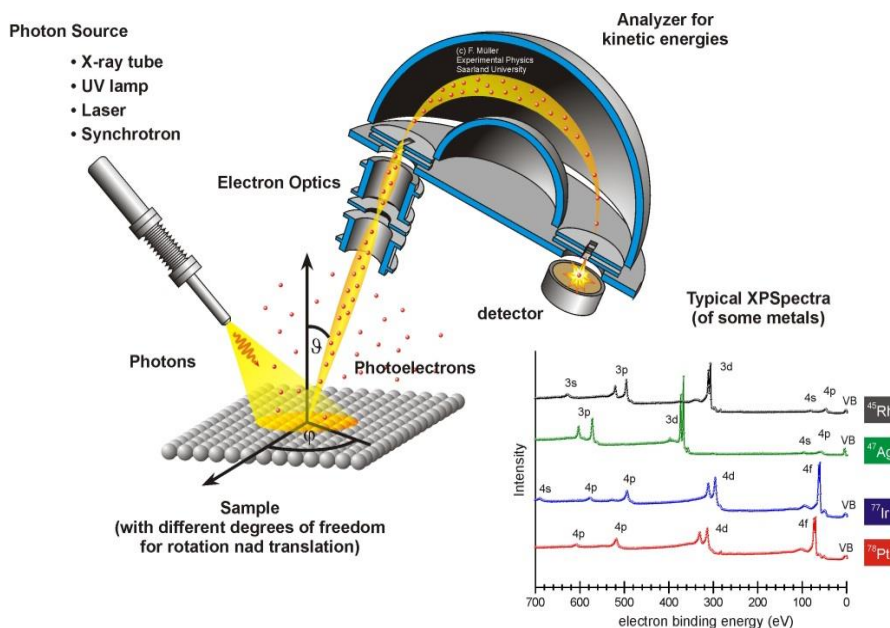

Figure 5. Main components of an XP spectrometer and XP spectra typical of some elements.

Source: X-ray tube consisting of a tungsten cathode and a copper anode coated by aluminium on a face and magnesium on the other face. These materials are chosen for two reasons:

- energy of the X-ray beam sufficiently high to allow the excitation of the core electrons;

- Full Width at Half Height (FWHM) of the peak usually between 0.7-0.8 eV since the resolution of the instrument is inversely proportional to the bandwidth of the incident beam. The electrons produced at the cathode by thermionic effect are accelerated by a potential of 15 keV and directed towards the anode, because of this collision X photons will be emitted.

Analyser: consisting of two concentric metal hemispheres (electrostatic plates) between which a ddp is applied. As a function of the potential applied to the grid of entrance (Pass Energy) electrons will be deflected differently according to their kinetic energy and only those having the desired E_k will arrive at the detector.

Vacuum System: allows obtaining UHV conditions through turbomolecular and ionic pumps. Moreover, the system can also be equipped with a titanium sublimation pump.

The instrument used to perform XPS measurements is PHI 5600 Multi Technique System which gives good control of the electron take-off angle (base pressure of the main chamber 3×10^{-8} Pa).[5,6] Samples, placed on a molybdenum specimen holder, were excited with Al-Kα X-ray radiation using a pass energy of 5.85 eV. The instrumental energy resolution was ≤ 0.5 eV. Spectra calibration was achieved by fixing the Ag $3d_{5/2}$ peak of a clean sample at 368.3 eV; this

method turned the C 1s main peak at 285.0 eV.[5,7] XPS peak intensities were obtained after Shirley background removal.[8] The atomic concentration analysis was performed by taking into account the relevant atomic sensitivity factors. The fitting of the XP spectra in the C 1s, N 1s and Au 4f−Zn 3p binding energy region was carried out by fitting the spectral profile with symmetrical Gaussian envelopes, after subtraction of the background. This process involves data refinement, based on the method of the least squares fitting, carried out until there was the highest possible correlation between the experimental spectrum and the theoretical profile. The residual or agreement factor R, defined by $R = [\Sigma(F_{obs} - F_{calc})^2 / \Sigma (F_{obs})^2]^{1/2}$, after minimization of the function $\Sigma(F_{obs} - F_{calc})^2$, converged to the value of 0.03. The fitting was performed using the XPSPEAK4.1 software.

References

1. J. Lim, S. P. Yeap, H. X. Che and S. C. Low. *Nanoscale Res. Lett.* 2013, **8**, 1–14.

2. C. I. Olariu, H. H. P. Yiu, L. Bouffier, T. Nedjadi, E. Costello, S. R. Williams, C. M. Halloran and M. J. Rosseinsky. *J. Mater. Chem.* 2011, **21**, 12650–12659.

3. X. Liu, M. Atwater, J. Wang and Q. Huo. *Colloids and Surfaces B: Biointerfaces* 2007, **58**, 3–7.

4. A. Jablonski. *Z. Phys.* 1935, **94**, 38–46.

5. D. Briggs and J. T. Grant. *Surface analysis by Auger and X-ray photoelectron spectroscopy*. IMP, Chichester, 2003.

6. A. Gulino. *Anal. Bioanal. Chem.* 2013, **405**, 1479–1495.

7. G. Greczynski and L. Hultman. *Angew. Chem. Int. Ed.* 2020, **59**, 5002–5006.

8. M. Repoux. *Surf. Interface Anal.* 1992, **18**, 567.

List of Abbreviations

^{1}H-NMR	Proton nuclear magnetic resonance
Abs	Absorbance
Au NCs	Gold nanoclusters
Au NPs	Gold nanoparticles
B.E.	Binding Energy
BL	Boat-like conformation
CL	Chair-like conformation
DFT	Density functional theory
DLS	Dynamic light scattering
DTAzDPH2P or Di-Triazine-Porphyrin	5,15-Di(phenyl) 10,20- Di-benzamide, N-ethyl, N-1,3,5 Tri-aminotriazine, 21H,23H-porphine
EDX	Energy dispersive X-ray
EELS	Electron energy loss spectroscopy
ESI-MS	Electrospray ionization mass spectrometry
Eu	Tris(dibenzoylmethane) mono(1,10-phenanthroline)europium (III)
EuNH$_2$	Tris(dibenzoylmethane) mono(5-amino-1,10-phenanthroline)europium (III)
HAADF-STEM	High-angle annular dark-field scanning transmission electron microscopy
HAuCl$_4$	Tetrachloroauric acid
ISO	International Organization for Standardization

MB	Methylene blue
NaBH$_4$	Sodium borohydride
NIR	Near-infrared
NM NPs	Noble metals nanoparticles
NP	Nanoparticle
PES	Potential energy surface
PL	Photoluminescence
R$_H$	Hydrodynamic radius
SERS	Surface Enhanced Raman Scattering
SPR	Surface plasmon resonance
TEM	Transmission electron microscopy
TOAB	Tetraoctylammonium bromide
UV-Vis	Ultraviolet-visible spectroscopy
XPS	X-ray photoelectron spectroscopy
XRD	X-ray Diffraction
ZnCit$^-$	[Zinc Citrate]$^-$ complex
ZnO	Zinc oxide

List of Publications

1) **L. Spitaleri**, G. Nicotra, M. Zimbone, A. Contino, G. Maccarrone, A. Alberti and A. Gulino.
Fast and Efficient Sun Light Photocatalytic Activity of Au_ZnO Core−Shell Nanoparticles Prepared by a One-Pot Synthesis.
ACS Omega **2019**, *4*, 15061–15066.

2) **L. Spitaleri**, C.M.A. Gangemi, R. Purrello, G. Nicotra, G. Trusso Sfrazzetto, G. Casella, M. Casarin and A. Gulino.
Covalently Conjugated Gold–Porphyrin Nanostructures.
Nanomaterials **2020**, *10*, 1644.

3) **L. Spitaleri**, F. Perricelli, G. Nicotra, G. Sfuncia and A. Gulino
Optical Properties of Emitting Dyes Bound to Au Nanostructures: Through Bond vs. Through Space Interactions.
To be Submitted.

List of Oral Communications

1) A. Gulino, **L. Spitaleri**, G. T. Sfrazzetto and I. Fragalà.

Molecular Nanostructures Covalently Assembled on Functionalized surfaces.

AIV, XXIV meeting AIV.

Giardini-Naxos, 07-10 May **2019**.

2) **L. Spitaleri**, G. Nicotra, M. Zimbone, A. Contino, G. Maccarrone, A. Alberti, A. Gulino.

Enhanced Visible Photocatalytic Activity of Au@ZnO core-shell Nanoparticles for Water Purification.

Convegno Regionale SCI della Sezione Sicilia.

Online, Italia, 2 December **2021**.

3) **L. Spitaleri**, C. M. A. Gangemi, R. Purrello, G. Nicotra, G. Trusso Sfrazzetto, G. Casella, M. Casarin, A. Gulino

Covalently Conjugated Gold–Porphyrin Nanostructures.

XXVII Congresso Nazionale SCI.

Online, Italia, 14-23 September **2021**.

Acknowledgements

I would like to thank all the people who contributed in some way to the work described in this thesis.

First and foremost, I want to thank my supervisor, Prof. Antonino Gulino, for his invaluable advice, support, and useful guide during my PhD study.

Additionally, I would like to express gratitude to Profs. Giuseppe Maccarrone and Annalinda Contino of the University of Catania for their invaluable support which has been influential in shaping my experiment methods for the synthesis of gold nanoparticles.

I would like to thank Profs. Giuseppe Trusso Sfrazzetto and Roberto Purrello of the University of Catania for their assistance in the synthesis of the novel bifunctional porphyrin.

I would like to thank Dr. Giuseppe Nicotra of CNR-IMM of Catania for their contribution to TEM analysis.

Last, but not least, I would like to express my gratitude to my wife and my family for their support, understanding, and encouragement during this very exciting "study way". Furthermore, I would like to thank my friends, lab mates and colleagues for a cherished time spent together in the laboratory and in social settings.